MODELING OF TUBULAR STRUCTURES AND FIBERS IN *IN VIVO* DATA: REVEALING ASYMMETRY IN HUMAN VASCULATURE AND WHITE MATTER FIBER TRACTS

by

Süheyla Çetin Karayumak

Submitted to the Graduate School of Engineering and Natural Sciences
in partial fulfillment of the requirements for the degree of
Doctor of Philosophy
in Computer Science and Engineering

Sabancı University

Spring 2015-2016

MODELING OF TUBULAR STRUCTURES AND FIBERS IN IN VIVO DATA: REVEALING ASYMMETRY IN HUMAN VASCULATURE AND WHITE MATTER FIBER TRACTS

APPROVED BY:

Assoc. Prof. Dr. Gözde ÜNAL
(Thesis Supervisor) .....

Prof. Dr. Berrin YANIKOĞLU .....

Asst. Prof. Dr. Deniz SEZER .....

Assoc. Prof. Dr. Selim BALCISOY .....

Asst. Prof. Dr. Ömer Sinan SARAÇ .....

DATE OF APPROVAL: 01/08/2016

©Süheyla Çetin Karayumak 2016
All Rights Reserved

to my family

Acknowledgments

First and foremost I would like to express my sincere gratitude to my advisor Assoc. Prof. Dr. Gozde Unal. She was a wise mentor when I needed guidance, a patient motivator when I needed an extra push, but above all a friend when I needed one. She always did the best for me and supported me with her heart and soul in the way of attaining my objectives. This thesis would not have come out without her supervision and invaluable guidance.

I would like to thank Assist. Prof. Dr. Evren Özarslan, Dr. Berkin Bilgin and Dr. Audrey Fan for their kind contributions and support to this thesis.

I also would like to thank TÜBİTAK BİDEB for providing the necessary financial support for my graduate education.

I am grateful to my committee members Prof. Dr. Berrin Yanıkoğlu, Assist. Prof. Dr. Deniz Sezer, Assoc. Prof. Dr. Selim Balcısoy, and Assist. Prof. Dr. Ömer Sinan Saraç for taking the time to read and comment on my thesis.

I owe special thanks to my friends and colleagues, particularly to, Rıza Alp Güler and Andaç Hamamcı for their friendship and assistance.

My husband, my best friend Fatih. You made my life better and more meaningful after coming into it. I am very lucky for having you as a companion on the path of life. Sena and Sümeyra, you are my sisters, my besties and the joys of my life. Thank you

for being with me all the time. My dad Mesut and my mom Hülya, there are no right words to express my gratitude for you. You dedicated yourselves for raising me as a better person. You always made me feel like the luckiest child in the world. Thank you for your unconditional support, love and belief in me. I would not have done any of these without your encouragement.

MODELING OF TUBULAR STRUCTURES AND FIBERS IN *IN VIVO* DATA: REVEALING ASYMMETRY IN HUMAN VASCULATURE AND WHITE MATTER FIBER TRACTS

Süheyla Çetin Karayumak

CS, PhD. Thesis, 2016

Thesis Supervisor: Gözde ÜNAL

Keywords: vessel tree segmentation, higher order tensor (HOT), vessel tractography, 4D tensor estimation over 3-sphere, branch modeling, coronary arteries, cerebral vasculature, bifurcations and n-furcations, DTI, HARDI, diffusion MRI, asymmetric fiber orientations, fiber asymmetry measure, asymmetric ODF, QSM, Susceptibility MRI, QSM reconstruction, vessel orientation constraint

Abstract

In medical image analysis, asymmetric modeling of vasculatures, such as cerebro- or cardio-vessels, is a challenging task because of the n-furcated branching geometries. Detection of asymmetry in anatomical structures such as vessels is a significant step in the accurate modeling of vasculatures. Therefore, it is essential to present new computational methodologies to model the underlying asymmetries in anatomical structures. For the asymmetric modeling of vasculatures, which is the first part of this thesis, we present a vasculature segmentation method that is based on a cylindrical flux-based higher order tensor (HOT). On a vessel structure, the HOT naturally models branching points as well as the tubular sections of the vessels. We demonstrate quantitative validation of the proposed algorithm on synthetic complex tubular structures, cerebral vasculature in Magnetic Resonance Angiography (MRA) datasets and coronary arteries from Computed Tomography Angiography (CTA) volumes.

Capturing asymmetry in white matter (WM) fibers is another open problem. Detection of asymmetry in fibers is important in both the localization and the quantitative assessment of specific neuronal pathways. More than 60% of WM fiber populations make crossings in a voxel, therefore, it is natural to expect a substantial part of those to involve asymmetric crossings/junctions. However, most well-known white matter fiber reconstruction methods assume symmetric signal acquisition that yield symmetric orientation distribution functions (ODFs) even when the underlying geometry is asymmetric. In the second part of this thesis, we employ inter-voxel filtering approaches through a cone model to reveal more information regarding the cytoarchitectural organization within the voxel. The cone model facilitates a sharpening of the ODFs in some directions while suppressing peaks in other directions, thus yielding an asymmetric ODF (AODF) field. The feasibility of the technique is demonstrated on *in vivo* data obtained from the MGH-USC Human Connectome Project (HCP) and Parkinson's Progression Markers Initiative (PPMI) Project database.

Quantitative Susceptibility Mapping (QSM) reconstruction is a recent technique for venous imaging. The reconstruction of QSM image volume is a challenging problem due to its long acquisition time, which causes several artifacts that need to be handled separately using a regularization term in the reconstruction. Prior knowledge such as smoothness and sparsity assumptions has been widely used as regularization. We hypothesize that incorporation of local orientation of vessels into regularization leads to an enhanced imaging of vasculatures. In the last part of this thesis, we present vessel orientation as a new regularization term to improve the accuracy of l_1- and l_2-norm regularized QSM reconstruction in cerebral veins. Using a multi-orientation QSM acquisition as gold standard, we show that the QSM reconstruction obtained with the vessel anatomy prior provides up to 40% Root-Mean-Square-Error (RMSE) reduction relative to the baseline l_1 regularizer approach.

IN VIVO VERİLERİNDE TÜBÜLER YAPILARIN VE LİFLERİN MODELLENMESİ: İNSAN DAMAR SİSTEMİ VE AK MADDE YOLAKLARINDA ASİMETRİNİN ORTAYA ÇIKARILMASI

Süheyla Çetin Karayumak

CS, Doktora Tezi, 2016

Tez Danışmanı: Gözde ÜNAL

Anahtar Kelimeler: damar ağacı bölütleme, yüksek mertebeli tensör, damar traktografi, 3-kürede 4-Boyutlu tensör kestirme, dal modelleme, koroner arterler, beyin damar sistemi, ikiye çatallanma, n'e çatallanma, Difüzyon Tensör Görüntüleme, Difüzyon MR, asimetrik lif yönleri, lif asimetri ölçümü, asimetrik yön dağılım fonksiyonu, QSM, Suseptibilite MR, QSM verisini oluşturma, damar yön kısıtı

Özet

Tıbbi görüntü analizinde damar sistemlerinin, beyin ve kalp damarları gibi, asimetrik modellemesi n'e çatallanma nedeniyle zorlu bir işlemdir. Damarlarda asimetrinin tespiti, damar sisteminin doğru modellenmesinde önemli bir adımdır. Bu nedenle, anatomik yapılarda altta yatan asimetrinin modellenmesinin yeni hesaplamalı yöntemlerle sunulması esastır. Damar sistemlerinin asimetrik modellenmesi icin akı tabanlı yüksek mertebeli tensör (YBT) ile damar sistemi bölütleme yöntemi bu tezin ilk bölümü olarak sunulmuştur. Damar yapısı üzerinde YBT tübüler kesitlerin yanında damar dallanma noktalarını da modeller. Önerdiğimiz yöntemin sayısal doğrulamasını karmaşık yapılı sentetik damar ağacında, Magnetik Rezonans Anjiyografi'de (MRA) beyin damar sisteminde ve Bilgisayarlı Tomografi Anjiyografi'de (BTA) koroner damarlarda ispat ediyoruz.

Ak madde liflerinde asimetrinin yakalanması çözülememiş diğer bir problemdir. Lif

yapılarında asimetrinin tespiti özgül nöronal yolakların konumlandırılmasında ve sayısal değerlendirilmesinde de önemli bir adımdır. Ak madde liflerinin %60'ından fazlası kesişir ve bunların önemli bir kısmının asimetrik kesişmesinin ya da çatallanmasının beklenmesi doğaldır. Buna rağmen en bilinen ak madde lif yapılandırma yöntemleri altında yatan geometri asimetrik olsa dahi simetrik sinyal edinimi (simetrik yön dağılım fonksiyonu (YDF)) varsayar. Bu tezin ikinci kısmında hücresel yapınının mimarisini ortaya çıkaran vokseller arasında koni modeliyle filtreleme yaklaşımları sunuyoruz. Koni modeli YDFlerin bazı yönlerinde keskinleştirilmesini sağlarken diğer yönleri bastırır, bu sayede asimetrik yön dağılım fonksiyonu (AYDF) oluşur. Tekniğin uygulanabilirliği MGH-USC HCP ve PPMI veritabanlarından sağlanan *in vivo* verilerinde test edilmiştir.

Sayısal Suseptibilite verisi oluşturma (QSM) venöz görüntüleme için yeni bir yöntemdir. QSM görüntü hacminin oluşturulması uzun edinim zamanı dolayısıyla zorlu bir problemdir. Uzun edinim zamanı pek çok artifakta neden olur, bunlar da regularizasyon teriminin kullanılmasıyla ayrı ayrı ele alınmasına sebep olur. Regularizasyonda yumuşatma ve seyreklik varsayımları önsel bilgi olarak çokça kullanılmaktadır. Biz de damar yönelimlerini regularizasyon terimine katarak damar sisteminin daha gelişmiş bir şekilde görüntülenebileceği yönünde hipotez kurduk. Tezin son bölümünde, beyin damarlarında l_1- ve l_2-norm tabanlı QSM yapılandılmasının doğruluğunu arttırmak için damar yönelimini yeni bir regularizasyon terimi olarak öneriyoruz. Çok yönlü QSM edinimini altın standart olarak kullanarak damar yönelimli l_1 regularizasyon yöntemini standart l_1 regularizasyon yöntemiyle karşılaştırdık ve %40'a kadar Kök-Ortalama-Kare-Hatasında (KOKH) iyileştirme gözlemledik.

Table of Contents

Acknowledgments **vi**

Abstract **viii**

Özet **x**

1 Introduction **1**
1.1 Motivation of the thesis . . . 1
1.2 Background on Anatomy . . . 2
1.2.1 Arteries . . . 2
1.2.2 Cerebral Veins . . . 5
1.2.3 White Matter Tracts . . . 5
1.3 Anatomical Orientations and Planes . . . 6
1.4 Imaging Modalities . . . 7
1.4.1 Computed Tomography Angiography (CTA, cardiac CT, cardiac CAT) 8
1.4.2 Magnetic Resonance Angiography . . . 9
1.4.3 Diffusion MRI and Diffusion Tensor Imaging . . . 10
1.4.4 Quantitative Susceptibility Mapping (QSM) . . . 12
1.5 Thesis Contributions and Overview . . . 13
1.6 List of Abbreviations . . . 17

2 A Higher-Order Tensor Vessel Tractography for Segmentation of Vascular Structures **18**
2.1 Literature Review . . . 19
2.2 Mathematical Background . . . 21
2.3 Method . . . 22
2.3.1 Higher Order Tensor (HOT) Model in 4D . . . 23
2.3.2 A Flux-based Measurement Model . . . 26
2.3.3 Higher Order Tensor Fitting and Decomposition . . . 28
2.3.4 Vessel Lumen Thickness Estimation . . . 34
2.3.5 Implementation Details . . . 35
2.4 Experiments and Results . . . 36
2.4.1 Method Validation . . . 37
2.4.2 Sensitivity to Initial Seed Position . . . 47
2.4.3 Computational Aspects . . . 48

2.5 Discussions . . . 49
2.6 Conclusion . . . 51

3 Asymmetric orientation distribution functions (AODFs) revealing intravoxel geometry in diffusion MRI 52
3.1 Literature Review . . . 52
3.2 Mathematical Background . . . 56
3.3 Method . . . 57
3.3.1 Asymmetric ODFs revealed by a cone model . . . 58
3.3.2 Measuring Asymmetry . . . 61
3.4 Experiments and Results . . . 62
3.4.1 Synthetic Fibers . . . 63
3.4.2 Real MRI Data Fibers . . . 70
3.4.3 Asymmetry Index Map Results . . . 75
3.5 Discussions and Conclusion . . . 81

4 Vessel Orientation Constrained Quantitative Susceptibility Mapping (QSM) Reconstruction 83
4.1 Literature Review . . . 84
4.2 Mathematical Background . . . 84
4.2.1 l_1- or l_2- regularized QSM reconstruction . . . 84
4.2.2 Oxygen Extraction Fraction (OEF) . . . 86
4.3 Method . . . 86
4.3.1 Segmentation . . . 86
4.3.2 l_1- or l_2- regularized QSM reconstruction with vessel orientation (VO) constraint . . . 87
4.4 Experimental Results . . . 89
4.4.1 Validation data . . . 90
4.4.2 *in vivo MRI data* . . . 92
4.4.3 QSM + MFAST data . . . 94
4.5 Discussions and Conclusion . . . 96

5 Summary of Contributions and Conclusion 99

Bibliography 102

List of Figures

1.1 *Illustration of the heart and coronary arteries [1]* 3

1.2 *Illustration of coronary artery disease [2]* 3

1.3 *Illustration of the Circle of Willis (CoW) and cerebral arteries [3]* 4

1.4 *Anatomy of the cerebral veins [4].* 5

1.5 *Gray matter and white matter [4].* 6

1.6 *Illustration of several white matter tracts [4].* 7

1.7 *Axial/transverse, coronal and sagittal planes that divides body into three orthogonal parts. source: Anatomy tutorial, University of Minnesota.* . . . 8

1.8 *Cardiac CTA images from three different views. Arrows indicate LCA.* . . 9

1.9 *MIP view of a sample MRA volume that visualizes cerebral arteries.* 10

1.10 *Diffusion weighted Spin Echo Pulse Sequence [5].* 11

1.11 *(a) B_0 (Non-diffusion weighted image); (b) FA image; (c) Color-FA image.* 12

1.12 *MIP view of a sample QSM volume.* 13

2.1 $60 \times 60 \times 60$ *synthetic Y-junction volume: Comparison between $S(\boldsymbol{g})$ measurements (a), and their rank-2 (b), rank-3 (c), and rank-4 (d) tensor fit model in 3D. Neither of these Cartesian tensor models in 3D are capable of modeling the whole vessel structure.* 23

2.2 *Flowchart of the proposed HOT Vessel Tractography method.* 24

2.3 *Each row illustrates a different type of n-furcation (first row for the crossing vessels, second row for modeling trifurcation, and the last row depicts asymmetric trifurcation.). Each column represents 3D/4D third or fourth order tensors: Left: fitting measurements to the 3D third order tensor model (purple); Second from Left: 3D fourth order tensor model (blue); Second from Right: 4D third order tensor model (orange); Right: 4D fourth order tensor model (green). 4D tensors are projected to 3D after decomposition (Section 2.3.3) for visualization.* 25

2.4 *Illustrations of: (a) directional measurement model: each* Cyl_i *is characterized by the direction vector* $\boldsymbol{g}$ *, the height h, and the circle centered at point* $\boldsymbol{x}_l$ *with radius r,* $\boldsymbol{x}_s$ *is the center point on the base circle of the cylinder; (b) cross sectional view of the cylindrical model.* 27

2.5 *Higher-order tensor representation of the ODF by a rank-1 approximation: (a) Two crossing fibers example; (b) DTI representation of crossing fibers; (c) the ODF model; (d) Two rank-1 terms and an isotropic part. (Fig. adapted from [6].)* 32

2.6 *Estimated modes (green) of the higher order tensors (red) are shown on synthetic Y-junction and T-junction volumes. Modes of the tensors along the centerline are depicted by blue.* 34

2.7 *Estimated modes (blue) of the higher order tensors (red) are shown on synthetic asymmetric-junction, crossing junction, and trifurcation volumes.* . . 34

2.8 *Illustration of the vessel lumen thickness estimation: multiple cylinders are fitted and "best fit radius" is calculated using Eq. (2.11).* 35

2.9 *(a,c) MIP views of VascuSynth dataset 1 and 3, respectively; (b) Extracted vessel tree for synthetic dataset 1; (d) Extracted vessel tree for synthetic dataset 3; Centerline of the vessel (green), extracted surface surrounds centerline (red) are depicted.* 37

2.10 *Segmentation results from Rotterdam dataset 6 (from training database). Orange: results for the new method; Green: results for the earlier method [7]; Violet: reference; (a) Extracted centerline, previous method's result and reference centerline; (b) Zoomed view of a segment where the two methods, particularly the earlier one deviate from the reference; (c) Extracted radii, previous method's radii and reference radii are rendered around the centerline.* 38

2.11 *(Top row) Segmented arteries from the earlier method [7] and the new method are shown for Rotterdam datasets 16, 22 and 30 with anatomical views; (Bottom row) MIP views of the datasets, red indicates the vessels that are evaluated in the Rotterdam Framework. Orange: results for the new method; Green: results for the earlier method. Four reference points per vessel are provided in Rotterdam database (Purple spheres): Point S is the start point of the branch, Point E is the end point, Point A and Point B are two reference points in between Point S and Point E.* 39

2.12 *(a,d) Volume rendering of aorta and vessels from datasets 23 and 30; (b,e) all vessels that are detected by the proposed method; (c,f) extracted vessels are shown with aorta as volume rendering.* 40

2.13 *Estimated higher order models are depicted (red) on the slices of CTA dataset of 14, 17, 24, and 29 from Rotterdam database. (a) Sagittal slice cuts the stenotic region (green) on dataset 14; (b) Axial slice cuts the stenotic region (green) on dataset 24; (c) Tensor fitting on dataset 17 at low contrast and noisy intensity regions; (d) Tensor fitting example at branching; (e, f, g, h) Zoomed views of the regions for CTA dataset of 14, 24, 17 and 29 respectively.* 41

2.14 *(a) MIP view of a sample MRA data; (b) Output of the proposed algorithm (red); (c) Output of the algorithm displayed similarly to the manual segmentation (green).* 42

2.15 *Comparison of our new method (purple) and previous method (green) on a sample MRA dataset.* 43

2.16 *Top row: (a, b, c, d) MIP views of MRA datasets 01, 32, 49, 58; Second row (e, f, g, h): Corresponding manual segmentation results [8]; Third row (i, j, k, l): Our results from the corresponding datasets; Bottom row (m, n, o, p): Results from the corresponding datasets using previous method [7].* . 44

2.17 *Seed selection from different branch points on the* 58^{th} *dataset of MIDAS MRA database, where seeds are shown by red spheres.* 48

3.1 *ODF field that is reconstructed by QBall imaging [9] on a sample HARDI data.* 54

3.2 *Flowchart of the proposed AODF reconstruction method.* 56

3.3 *Spherical harmonics basis. First 15 coefficients of the modified symmetric spherical harmonics bases are illustrated, which are used to represent DMRI spherical functions on the sphere. The bottom row shows that any spherical function can be represented as a sum of SH coefficients [10].* 58

3.4 *(a) The cone* $\mathbf{C}_{\boldsymbol{x},\hat{\boldsymbol{u}}}$ *is constructed with a certain height and a radius; (b) An asymmetric ODF is reconstructed by rotating the cone model along all sampled directions on the unit sphere at each voxel point, and executing a directional regularization on the ODF field in* $\mathbf{C}_{\boldsymbol{x},\hat{\boldsymbol{u}}}$. 59

3.5 *(a) Asymmetry index map; (b) FA map calculated for circularly bending fibers:(bright-to-dark:high-to-low values).* 62

3.6 *Circularly bending fibers: (a) AODF field created by the analytical results in [11]; (b) ODF field created by the DOT method [12]; (c) AODF field created by the proposed technique.* 64

3.7 *Simulations for strong curvature fibers. (a): ODFs obtained via the method in Ref. [13]; (b) AODF maps obtained by Gaussian filtering (Figure c and d are in the following page).* 65

3.7 *Simulations for strong curvature fibers. (c) AODF maps obtained by bilateral filtering; (d) AODF maps obtained by steerable filtering.* 66

3.8 *Simulations for kissing fibers. (a): ODFs obtained via the method in Ref. [13]; (b) AODF maps obtained by Gaussian filtering (Figure c and d are in the following page).* 67
3.8 *Simulations for kissing fibers. (c) AODF maps obtained by bilateral filtering; (d) AODF maps obtained by steerable filtering.* 68
3.9 *Simulations for branching fibers. (a): ODFs obtained via the method in Ref. [13]; (b) AODF maps obtained by Gaussian filtering (Figure c and d are in the following page).* 71
3.9 *Simulations for branching fibers. (c) AODF maps obtained by bilateral filtering; (d) AODF maps obtained by steerable filtering.* 72
3.10 *The results of (a) Gaussian filtering; (c) bilateral filtering; (e) steerable filtering on HCP HARDI data; (b, d, f) zoomed views of each filtering techniques.* 73
3.11 *The result of steerable filtering on PPMI HARDI data.* 74
3.12 *FA (a) and asymmetry (b, c, d) maps (bright-to-dark:high-to-low values) calculated for strong curvature fibers; (b): Filtering with a Gaussian function; (c): Bilateral filter based on a Gaussian distribution; (d): Steerable Gaussian filter.* 76
3.13 *FA (a) and asymmetry (b, c, d) maps (bright-to-dark:high-to-low values) calculated for kissing fibers; (b): Filtering with a Gaussian function; (c): Bilateral filter based on a Gaussian distribution; (d): Steerable Gaussian filter.* 77
3.14 *FA (a) and asymmetry (b, c, d) maps (bright-to-dark:high-to-low values) calculated for branching fibers; (b): Filtering with a Gaussian function; (c): Bilateral filter based on a Gaussian distribution; (d): Steerable Gaussian filter.* 78
3.15 *An axial slice depicting the asymmetry and FA maps on a sample PPMI data in (a) and (b), respectively.* 79
3.16 *An axial slice depicting the computed asymmetry and FA maps on a HCP data sample in (a) and (b), respectively.* 80

4.1 *Flowchart of the proposed QSM reconstruction method.* 85
4.2 *Illustration of vessel prior on a region of a vessel branch.* 88
4.3 *A ground truth* in vivo *phantom data from QSM image with 12-orientations; (a) the less detailed vessel tree from the phantom data; (b) the result of* l_2 *regularized reconstruction with VO constraint for the less detailed vessel tree segmentation (4 seed points are used for vessel segmentation, and the reconstruction has* 13.38% *RMSE); (c) the more detailed vessel tree from the phantom data; (d) the result of* l_1 *regularized reconstruction with VO constraint for the more detailed vessel tree segmentation (7 seed points are used for vessel segmentation, and the reconstruction has* 5.13% *RMSE).* . . 91
4.4 *A ground truth* in vivo *phantom data from QSM image with 12-orientations; (a) the less detailed vessel tree from the phantom data; (b) the result of* l_2 *regularized reconstruction with VO constraint for the less detailed vessel tree segmentation (4 seed points are used for vessel segmentation, and the reconstruction has* 6.27% *RMSE); (c) the more detailed vessel tree from the phantom data; (d) the result of* l_1 *regularized reconstruction with VO constraint for the more detailed vessel tree segmentation (7 seed points are used for vessel segmentation, and the reconstruction has* 11.23% *RMSE).* . 92
4.5 *Simulations result from ground truth susceptibility phantom. RMSE values were computed using a known ground truth susceptibility map. (a) Original* χ *field; (b) noisy normalized field map (input to QSM reconstruction); (c)* l_1 *regularized reconstructed* χ *field (*8.37% *RMSE); (d)* l_1 *regularized reconstructed with VO constraint* χ *field (*5.13% *RMSE). Arrows point out the reconstruction comparisons on the sample veins.* 93
4.6 *(Left Column) Original QSM map; (Middle Column) extracted centerlines of the vessels; (Right Column) surface renderings for the vessels are shown for two healthy subjects.* 94

4.7 *OEF visualization on two sample subjects from ten data volume (shown in hot colors); (a) QSM reconstruction without vessel orientation is shown on the first subject; (b) the result of l_1 regularized reconstruction with VO constraint is shown on the first subject; (c) QSM reconstruction without vessel orientation is shown on the second subject; (d) the result of l_1 regularized reconstruction with VO constraint is shown on the second subject.* 95

4.8 *Top row: Left Column-vessel tree extraction from QSM data, Right Column-vessel tree extraction from MFAST data ; Bottom row: (First column) QSM reconstruction without vessel orientation, (Second column) l_1-reg QSM data reconstructed with vessel orientation constraint (Vessel tree is extracted from the QSM data), (Third column) l_1-reg QSM data reconstructed with vessel orientation constraint (vessel tree is extracted from the MFAST data).* . . . 97

List of Tables

2.1 *Summary of Rotterdam Results* 42
2.2 *Rotterdam Results of our previous method [7]* 42
2.3 *Segmentation results of our method on MIDAS MRA volumes* 46

Chapter 1

Introduction

1.1 Motivation of the thesis

Asymmetric branching geometry such as bifurcations, trifurcations or even n-furcations are abundant in human vasculature. In the domain of human neural circuitry, as the percentage of white matter voxels that contain crossing fibers is thought to be greater than 60%, it is natural to expect a substantial part of those to involve asymmetric crossings/junctions. Hence, capturing asymmetry in anatomical structures such as vessels and white matter fibers is a significant step in the accurate modeling of vasculatures, and in both localization and quantitative assessment of specific neuronal pathways. Therefore, it is important to device new computational models to reveal the underlying asymmetries in anatomical structures. In the literature, there are no adapted methods to represent: (i) asymmetric junctions in vascular trees; (ii) asymmetric crossings in white matter fibers. These are two of the challenging problems whose solutions we undertake in this thesis.

Magnetic Resonance Imaging reconstruction is a challenging problem due to its long acquisition time. It requires patients to remain motionless within a tight, closed environment typically for half an hour or longer, which is especially hard in pediatric and patient populations. For the reconstruction of MRI, prior knowledge such as smoothness and sparsity assumptions have been widely used as regularization. However, local orientation of vessels was not utilized before. We propose to employ vessel orientation as part of the regularization for a more accurate imaging of vasculatures.

In this thesis, we present contributions to the solution of the above mentioned three problems. Before we dwell on the details of the newly proposed methods, we present a background on anatomy in the following section, as the application domain of this thesis involves imaging of human anatomy and medical image computing.

1.2 Background on Anatomy

This section describes the background information on anatomical structures targeted in this thesis.

1.2.1 Arteries

Arteries are the blood vessels that deliver oxygenated blood from the heart to the tissues of the body. Physically, arteries are muscular tubes that usually branch into two (e.g as in coronary arteries). Sometimes they may n-furcate into several branches at a point (e.g Circle Of Willis (CoW) of Brain).

1.2.1.1 Coronary arteries

The coronary arteries, which originate from the coronary ostium (root of aorta), may be divided into two sets: the right (RCA) and left coronary arteries (LCA) [4]. The left coronary artery (LM - left main) system bifurcates into the circumflex artery (LCX) and the left anterior descending artery (LAD). Left coronary artery supplies blood for left ventricle and right coronary artery feeds right ventricle. Figure 1.1 depicts four chambers (Left and Right Atria; Left and Right Ventricles) and coronary arteries (RCA, LAD (LM), LCX, LAD) of the heart. Arteries (blood vessels) surrounding the heart are shown by red.

According to the statistics of World Health Organization (WHO), coronary heart disease (CHD) is the leading cause of death worldwide. The most common cause for CHD, coronary artery disease (CAD) is caused because of the damage in the inner walls of the coronary arteries due to multiple risk factors such as high blood pressure, high cholesterol, smoking and diabetes. Plaque (See Figure 1.2), which contains calcium, cholesterol and other substances in the blood, accumulates excessively on the damaged inner walls of the

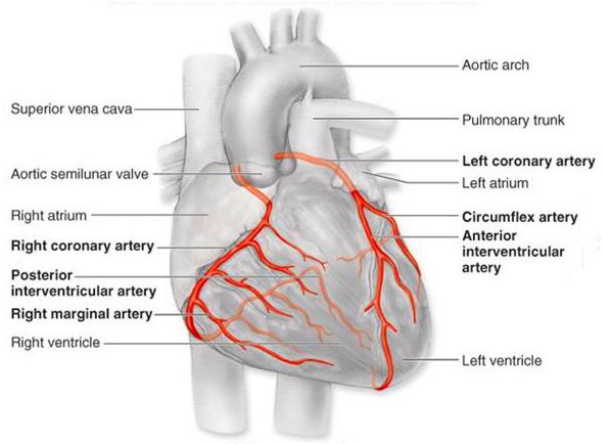


Figure 1.1: *Illustration of the heart and coronary arteries [1]*

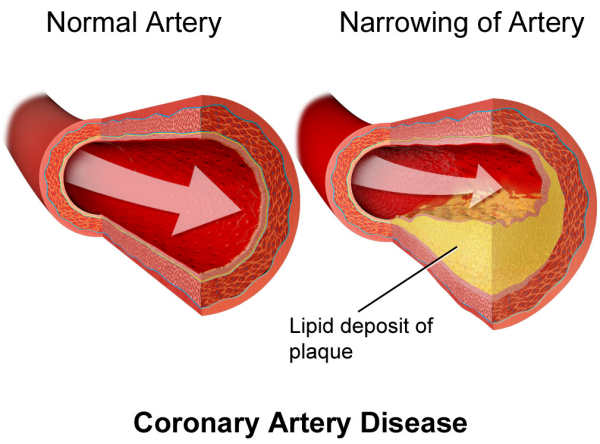


Figure 1.2: *Illustration of coronary artery disease [2]*

coronary arteries, which causes atherosclerosis, or hardening of the arteries [14]. Over a period of time, plaque begins to completely block the oxygen and nutrient-rich blood flow to the heart, which causes heart muscle cells to die and leads to myocardial infarction (heart attack) at the end.

1.2.1.2 Arteries of the brain

Cerebral circulation is the oxygen and nutrients enriched blood movement for supplying brain via blood vessels [4]. Two major sets of vessels supply the cerebral arteries and the cerebrum: the common carotid arteries and the vertebral arteries. The common carotid

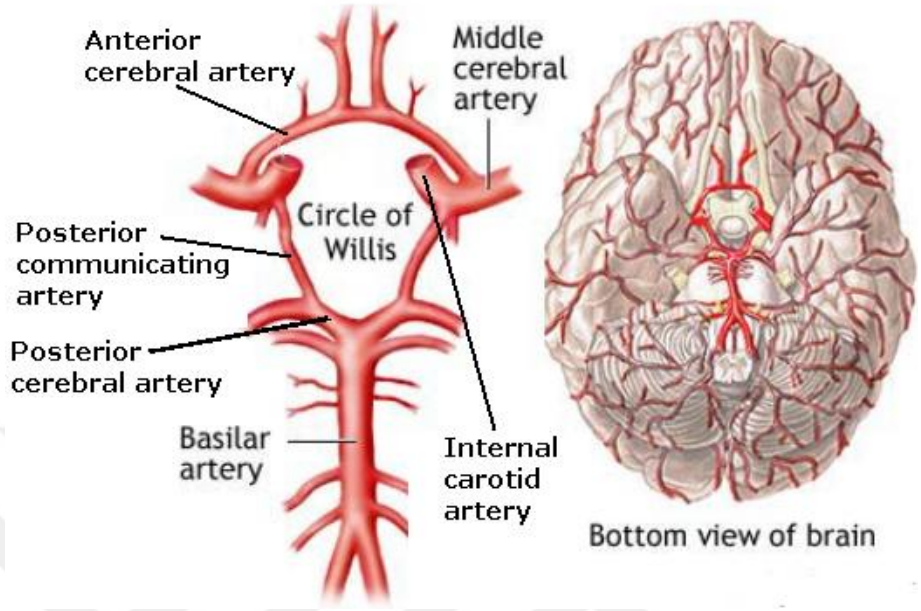


Figure 1.3: *Illustration of the Circle of Willis (CoW) and cerebral arteries [3]*

arteries have two divisions. The external carotid arteries supply the facial tissues. The internal carotid artery branches into the anterior cerebral artery (ACA) and then carves out the middle cerebral artery (MCA). The vertebral arteries supply the shoulders, arms and lateral chest.

The CoW is a part of cerebral circulation, which is a joining region of following arteries at the inferior side of the brain: Anterior cerebral artery, Internal carotid artery, Anterior communicating artery, Posterior communicating artery, Posterior cerebral artery, and Basilar artery. Figure 1.3 depicts CoW region and cerebral arteries (red). CoW may consist of several n-furcations, i.e multiple branchings in the same local neighborhood of the vessel segment.

Cerebrovascular diseases (e.g stroke) is the second leading cause of death, which occurs when there is an interruption or reduction in the blood flow through the brain. Recently, advanced imaging techniques have begun to improve the early detection, diagnosis and treatment of vascular diseases. Often, experts having high quality visualization systems are less probable to make wrong diagnosis. Additionally, visual models of the vessels are used in presurgical and interventional medical navigation systems for diagnosis of disease

and for better treatment options.

1.2.2 Cerebral Veins

The central nervous system consists of the cerebrum, cerebellum, brainstem and spinal cord, and it has a complex drainage system. The cerebrum, cerebellum and brainstem are drained by a number of veins, which empty into the dural veins: superior sagittal sinus, transverse, straight and sigmoid sinuses. Cortical veins are divided into Vein of Labbe (drains into the temporal lobe), and Vein of Trolard, which is the largest cortical vein that drains into the superior sagittal sinus (See Figure 1.4).

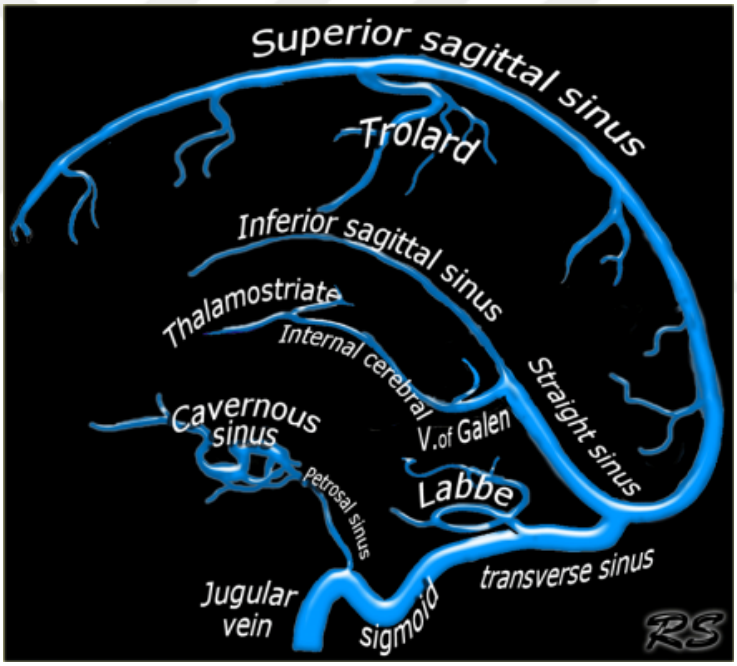


Figure 1.4: *Anatomy of the cerebral veins [4].*

1.2.3 White Matter Tracts

Brain tissue is composed mainly of *gray matter* and *white matter* (See Figure 1.5). Both gray matter and white matter have highly organized topographies. Gray matter is made up of dendrites, neuronal cell-bodies, synaptic connection sites, and glial cells. White matter is made up myelinated axonal projections. The color of gray matter is

gray brown due to the capillary blood vessels and the neuronal cell-bodies. Due to the abundance of neuronal cells, gray matter is the processing center of the brain. They reside mostly in the surface of the cerebral hemispheres (cerebral cortex), cerebellar cortex.

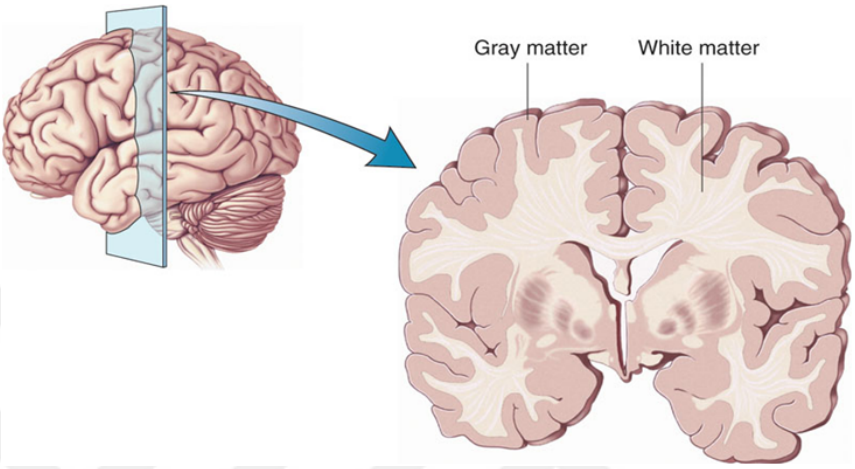


Figure 1.5: *Gray matter and white matter [4].*

White matter gets its color from the myelinated axons. Various gray matter structures or pathways are interconnected and traversed via the myelinated axons. White matter pathways connect the cortex to the other cortical gray matter regions, as well as the cerebellum, and the spinal cord. These pathways represent the fibrous information from the microscopic to the macroscopic scale. Physical basis of diffusion magnetic resonance imaging (DMRI) is based on the isotropic diffusion of water molecules in white matter due to thermally driven Brownian motion. DMRI probes the signal charges due to water molecules, which make it possible to indirectly detect the fine microstructure of the white matter and construct a digital representation of white matter pathways (fiber tracts) (Figure 1.6).

1.3 Anatomical Orientations and Planes

This section briefly summarizes the anatomical orientations and planes that are used in the medical imaging terminology. Here are the definitions for orientational and directional terms:

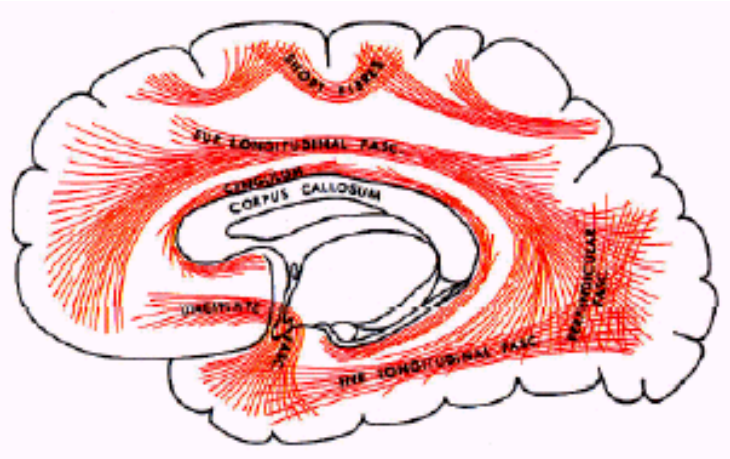


Figure 1.6: *Illustration of several white matter tracts [4].*

Superior: above of the body

Inferior: below of the body

Anterior: in front of the body

Posterior: behind of the body

For anatomical purposes, the human body is often sectioned into planes. Those frequently used body planes are as following:

Axial (Transverse): Horizontal plane, divides the body into inferior and superior parts

Sagittal: Vertical plane, divides the body into left and right parts

Coronal: Vertical plane, divides the body into posterior and anterior parts

See Figure 1.7 for the illustration of anatomical planes and orientations.

1.4 Imaging Modalities

Medical imaging provides non-invasive creation of geometric and visual representations of the internal organs, tissues and micro-structures of the body. Many different medical imaging modalities (Computed Tomography (CT), Magnetic Resonance Imaging (MRI),

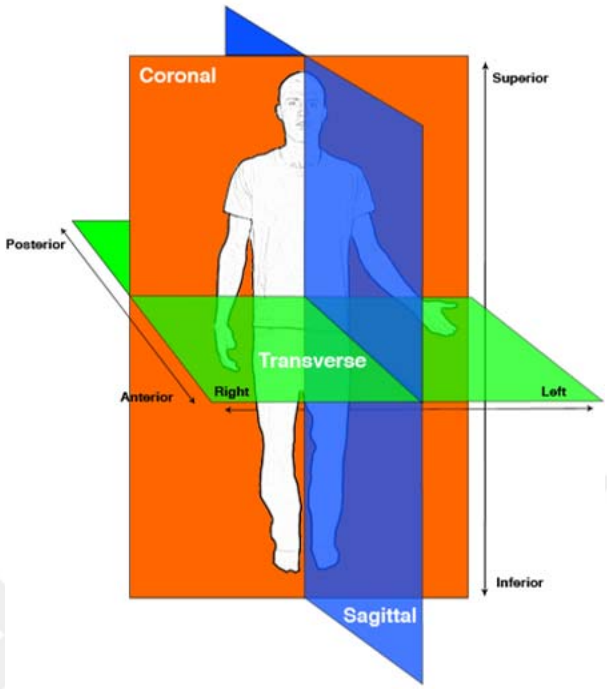


Figure 1.7: *Axial/transverse, coronal and sagittal planes that divides body into three orthogonal parts. source: Anatomy tutorial, University of Minnesota.*

Positron Emission Tomography (PET), PET-CT, Ultrasound, X-Ray) have been devised. Those that are used in this thesis are briefly explained in the following subsections:

1.4.1 Computed Tomography Angiography (CTA, cardiac CT, cardiac CAT)

CTA is mainly a cardiac (heart) imaging technique that uses advanced CT technology with an injected contrast agent and produces high resolution images of moving heart, arterial anatomy and plaque or calcium deposits in the artery walls. In addition, CTA has a fast image acquisition, which typically takes less than a minute, compared to other imaging techniques. During CTA acquisition, beams of X-rays are generated from a rotational X-ray source, which turns around a volume of interest of the patient's body. Attenuated X-ray beams are collected by the detectors from several different angles in the scanner. Then, the projection images are obtained from 3D attenuation volumes and a CTA image

volume is reconstructed. CTA is not the safest way of cardiac imaging, but it creates the finest images for visualizing arterial and venous vessels. Short acquisition time is another advantage of CTA (Figure 1.8).

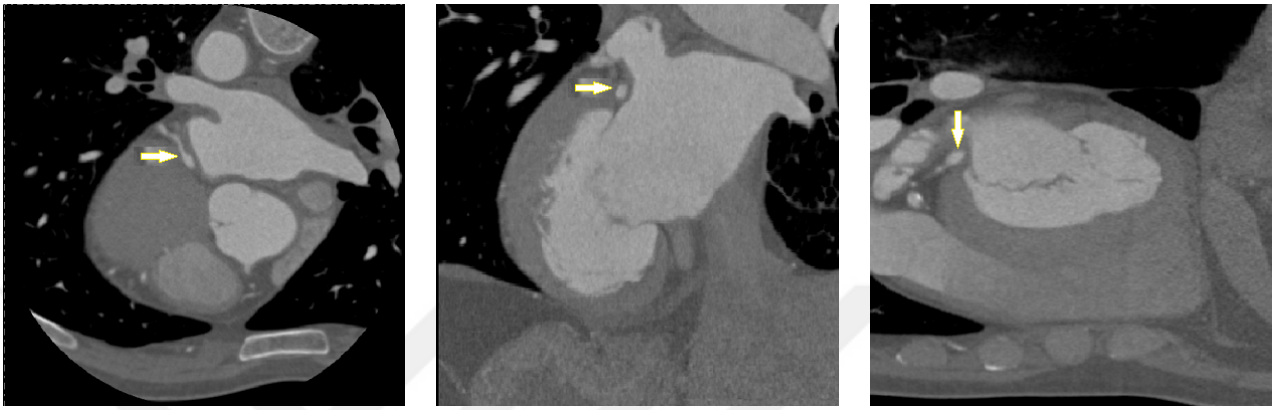


Figure 1.8: *Cardiac CTA images from three different views. Arrows indicate LCA.*

1.4.2 Magnetic Resonance Angiography

Magnetic Resonance Angiography (MRA) [15] is a Magnetic Resonance Imaging (MRI) technique, which is used for visualization of blood vessels such as the stationary arteries of the neck, brain, and the legs. It is utilized to detect stenosis (abnormal narrowing), aneurysms (vessel wall dilatation) on the vessels. MRA has drawbacks for visualizing coronary arteries due to several reasons: i) cardiac motion of heart; ii) higher cost than CTA; iii) lower resolution; and iv) longer scan times. However, MRA has advantages over CTA due to: i) lack of contrast agent injection, it is less invasive; ii) it is safer, since patient is not exposed to any ionizing radiation. MRA is mostly used for visualizing the cerebral vasculatures. Figure 1.9 depicts Maximum Intensity Projection (MIP) of a sample MRA volume that visualizes cerebral arteries. MIP is a rendering method that projects the 3D volume to the 2D plane by projecting the voxels with maximum attenuation/intensity value that fall in the way of parallel rays traced from the viewpoint to the plane.

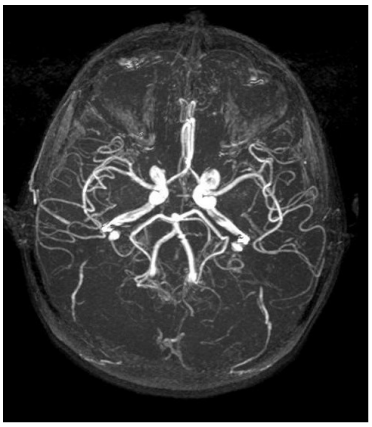


Figure 1.9: *MIP view of a sample MRA volume that visualizes cerebral arteries.*

1.4.3 Diffusion MRI and Diffusion Tensor Imaging

Diffusion MRI (DMRI) is an imaging technique based on Brownian (thermal) motion of water molecules to generate contrast in MR images. Signal occurs due to moving spins experiencing phase shift [16]. Signal drops in gradient directions corresponding to restricted diffusion i.e. along WM fibers [5].

The amount of attenuation depends on the amplitude and direction of the applied diffusion gradient. In order to generate diffusion weighted images, diffusion gradients are applied in certain directions. Strength of diffusion weighting is described by b factor. For the Stejskal-Tanner spin echo sequence (See Figure 1.10), the equation of the sequence is expressed as follows:

$$b = \gamma^2 G^2 \delta^2 \left(\Delta - \frac{\delta}{3} \right) \tag{1.1}$$

where b value is determined by duration of the pulse δ, G is the strength of gradient pulses, Δ is defined as the time interval between two gradients and γ is the gyromagnetic ratio [16].

The MR signal loss due to strong diffusion gradients could be expressed as in Eq. 1.2, where S is the measured diffusion weighted signal, S_0 is the signal without any diffusion gradient applied, b is diffusion weighting factor, and D is a diffusion constant which is also known as apparent diffusion coefficient (ADC).

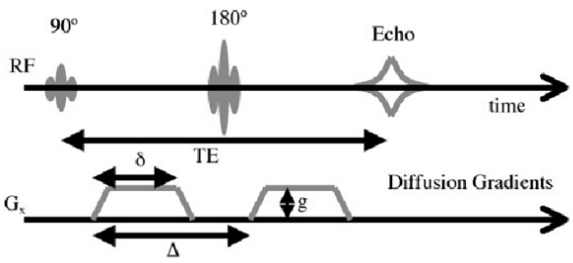


Figure 1.10: *Diffusion weighted Spin Echo Pulse Sequence [5].*

$$S = S_0 e^{-bD} \tag{1.2}$$

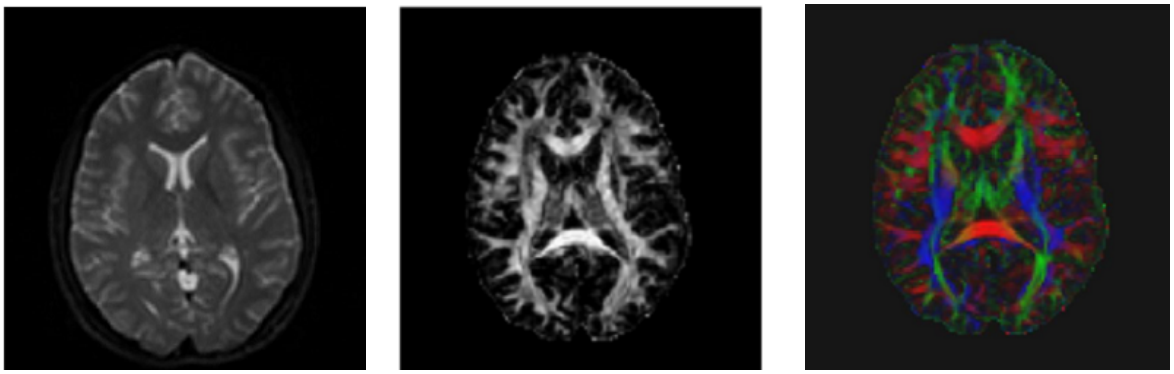
ADC represents the isotropic (uniform in all directions) diffusion when the diffusion is same in all directions. However, for a tissue which is oriented in a certain direction such as a white matter tract, diffusion signal becomes anisotropic (directionally dependent). Diffusion is typically represented mathematically with a 2^{nd} order tensor, which is here a 3×3 symmetric positive definite matrix (Eq. 1.3) that corresponds to an ellipsoid in three-dimensional (3D) space:

$$\boldsymbol{D} = \begin{bmatrix} D_{xx} & D_{xy} & D_{xz} \\ D_{xy} & D_{yy} & D_{yz} \\ D_{xz} & D_{yz} & D_{zz} \end{bmatrix}. \tag{1.3}$$

In the case of 3×3 diffusion tensor representation, Eq. 1.2 is reexpressed as in Eq. 1.4, where $b_0 = \gamma^2 G^2 \delta^2 \left(\Delta - \frac{\delta}{3}\right)$ and $\boldsymbol{g}$ is the gradient direction in 3D space:

$$S = S_0 e^{-b_0 \boldsymbol{g}^T \boldsymbol{D} \boldsymbol{g}}. \tag{1.4}$$

Diffusion Tensor Imaging (DTI) provides information about the orientation of the greatest diffusion at each voxel: the largest principal axis of the diffusion tensor aligns with the dominant fiber (white matter tract) orientation in an MRI voxel. In order to find the principal direction of the diffusion tensor, the tensor is diagonalized. The eigenvector corresponding to the largest eigenvalue represents the principal direction of the diffusion tensor.



(a) (b) (c)

Figure 1.11: *(a) B_0 (Non-diffusion weighted image); (b) FA image; (c) Color-FA image.*

Degree of anisotropy (DAI) of diffusion is measured in different ways. The most widely used DAI is fractional anisotropy (FA) [17], which varies from 0 (isotropic) to 1 (fully anisotropic) and is expressed as:

$$FA = \sqrt{\frac{3}{2}}\sqrt{\frac{(\lambda_1 - \bar{\lambda})^2 + (\lambda_2 - \bar{\lambda})^2 + (\lambda_3 - \bar{\lambda})^2}{\lambda_1^2 + \lambda_2^2 + \lambda_3^2}}, \tag{1.5}$$

where λ_1, λ_2 and λ_3 are the eigenvalues of the diffusion tensor $\boldsymbol{D}$, and $\bar{\lambda} = \frac{1}{3}\sum_{i=1}^{3}\lambda_i$. Hence, FA measures the variation among the eigenvalues of the diffusion tensor. When one of the eigenvalues is larger than the other two, presence of highly anisotropic WM fiber tissue is very likely.

The fiber orientations can be represented in a better way by weighting the rgb color channels with FA along each x, y, z component of principal direction of the tensor. Red color indicates the left-to right direction, green shows the anterior-posterior direction and blue represents the superior-inferior direction [17]. Figure 1.11 depicts B_0 image (no diffusion gradient applied), and corresponding FA and color-FA maps, respectively.

1.4.4 Quantitative Susceptibility Mapping (QSM)

QSM is a recently developed venographic imaging technique, which aims to estimate the tissue magnetic susceptibility that gives rise to subtle changes in the magnetic field [18] (Figure 1.12). Susceptibility is the magnetic property of the tissues, which gives rise to the

observed signal phase in MRI, and it is linearly proportional to the voxel intensity in QSM. Mapping susceptibility allows quantification of tissue iron concentration [19, 20] and vessel oxygen saturation [21, 22]. QSM has found use in the recent studies of neurodegenerative diseases, such as multiple sclerosis [23] and brain lesions characterization [24].

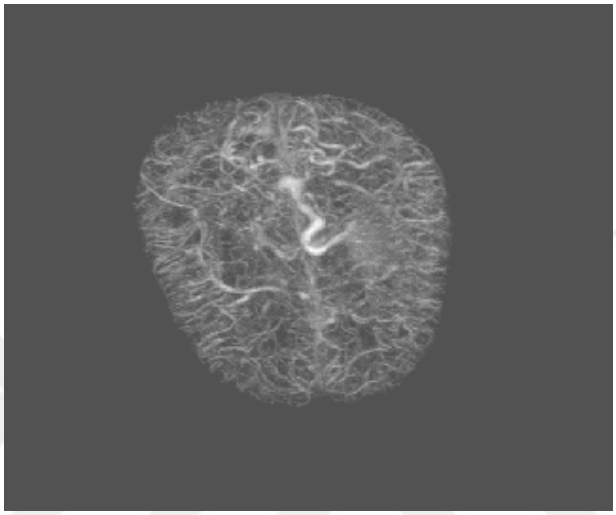


Figure 1.12: *MIP view of a sample QSM volume.*

1.5 Thesis Contributions and Overview

1. The complex tubular structures of vessels due to bifurcations and various pathologies make their segmentation a difficult problem in medical image analysis. The structures of the vessels become even more complex with multiple branchings (n-furcations), stents, calcifications and pathologies such as stenosis. Besides anatomical artifacts, several imaging complications occur during acquisition such as noise, partial volume effects and resolution constraints, which make the problem more challenging. In the first part of this thesis (Chapter 2), we aim to model several vasculatures from varying imaging modalities and create geometric model of vessels, which may be used in a medical navigation system both in surgical planning and detection of possible vascular anomalies. Our novel tubular structure segmentation and n-furcation modeling method is based on a flux-based higher order tensor

(HOT) that fits to a vessel, which is inspired from Higher Angular Diffusion Imaging (HARDI) modeling in MRI. We demonstrate quantitative validation of the proposed method on both synthetic complex tubular structures as well as real cerebral vasculature in MRA datasets and coronary arteries from CTA volumes. The contents of this study are published in:

- Suheyla Cetin, Gozde Unal, "A Higher-Order Tensor Vessel Tractography for Segmentation of Vascular Structures", IEEE Transactions on Medical Imaging, Volume 34, Issue 10, pages 2172-2185, Oct. 2015.

Other works related to this study are published in:

- Efe Ilicak, Suheyla Cetin, Elif Bulut, Kader Karli Oguz, Emine Ulku Saritas, Gozde Unal and Tolga Cukur, "Targeted vessel reconstruction in non-contrast-enhanced steady-state free precession angiography", NMR in Biomedicine Volume 29, Issue 5, pages 532-544, May 2016.
- H.A. Kirisli et al. (Suheyla Cetin, Gozde Unal co-authors of a large consortium of authors), "Standardized evaluation framework for evaluating coronary artery stenosis detection, stenosis quantification and lumen segmentation algorithms in Computed Tomography Angiography", Medical Image Analysis, Volume 17, Issue 8, Pages 859–876.
- Suheyla Cetin, Emine U. Saritas, Gozde Unal, "Vessel tractography for magnetic particle imaging angiography", Magnetic Particle Imaging (IWMPI), 2015 5th International Workshop on , 26-28 March 2015.
- Suheyla Cetin, Audrey P. Fan, Berkin Bilgic, Kevin Setsompop, Gozde Unal, "Semi-automated visualization and segmentation of cerebral veins from QSM", International Society for Magnetic Resonance in Medicine 23rd Scientific Meeting, Toronto, Canada, 2015 (ISMRM Merit Award Magna Cum Laude).
- Suheyla Cetin, Gozde Unal, "A cerebral blood vessels segmentation method using a flux based second order tensor model", Singal Processing and Communications Applications Conference (SIU), Trabzon, 2014.

- Suheyla Cetin, Gozde Unal, "Automatic detection of coronary artery stenosis in CTA based on vessel intensity and geometric features", MICCAI'12, 3D Cardiovascular Imaging Segmentation Challenge, Nice, 2012.

2. The diffusional attenuation of MR signal has been exploited to characterize tissue anisotropy through an indirect computation of the diffusion behavior of water molecules in human nervous system. Particularly, taking various diffusion-weighted images in several directions enables determination of the orientation of specific neuronal fiber tracts. By an assumption of a single fiber tract per voxel, the DTI has been proven to infer the dominant fiber direction sufficiently [25]. Unfortunately, in cases of heterogeneous fiber structures such as crossing, kissing, fanning or bending fiber configurations, the unimodal orientation distribution function (ODF) assumed by DTI is no longer capable of resolving the orientation of distinct fiber populations within a voxel. Alternatively, HARDI acquisitions, which evenly sample a single shell or multiple spherical shells, have been proposed [26], but assumption of a real DTI signal forces ODFs to become symmetric even if the underlying intravoxel geometry is asymmetric. In the second part of this thesis (Chapter 3), we propose a cone-based inter-voxel filtering method for representing the inherent asymmetry of the underlying intravoxel geometry. The cone model facilitates a sharpening of the ODFs in some directions while suppressing peaks in other directions, thus yielding an asymmetric ODF (AODF) field. The contents of this chapter are reported in:

   - Suheyla Cetin, Evren Ozarslan, Gozde Unal, "Elucidating Intravoxel Geometry in Diffusion-MRI: Asymmetric Orientation Distribution Functions (AODFs) Revealed by a Cone Model", Volume 9349 of the series Lecture Notes in Computer Science, Medical Image Computing and Computer-Assisted Intervention – MICCAI, (2015) pp 231-238.

3. QSM is used to estimate the underlying tissue magnetic susceptibility and oxygen saturation in veins [27]. In the last chapter of the thesis, we present vessel orientation as a new regularization term to improve the accuracy of l_1 and l_2 regularized QSM reconstruction in cerebral veins [28]. For that purpose, the vessel tree is first

extracted from an initial QSM reconstruction using Higher Order Vessel Tractography [29] (Chapter 2). In a second step, the vascular geometric prior is incorporated through an orthogonality constraint into the QSM reconstruction. The parts of this work are reported in:

- "Vessel Orientation Constrained Quantitative Susceptibility Mapping (QSM) Reconstruction", Lecture Notes in Computer Science, Medical Image Computing and Computer-Assisted Intervention – MICCAI, (2016).

This thesis is organized as five chapters including the Introduction chapter (Chapter 1). In Chapter 2, our study on"Higher-Order Tensor Vessel Tractography for Segmentation of Vascular Structures" is described. In Chapter 3, "Elucidating intravoxel geometry in diffusion-MRI: Asymmetric orientation distribution functions (AODFs) revealed by a cone model" study is presented. In Chapter 4, our "Vessel Orientation Constrained QSM Reconstruction" work is explained. In the last chapter, the conclusions of the thesis and future research directions are presented.

1.6 List of Abbreviations

Here is the list of mostly used abbreviations in this thesis:

MRI Magnetic Resonance Imaging

CT Computed Tomography

CTA Computed Tomography Angiography

WM White Matter

DTI Diffusion Tensor Imaging

DWI Diffusion Weighted Imaging

DMRI Diffusion Magnetic Resonance Imaging

HARDI Higher Angular Resolution Diffusion Imaging

QSM Quantitative Susceptibility Imaging

ODF Orientation Distribution Function

AODF Asymmetric Orientation Distribution Function

HOT Higher Order Tensor

CoW Circle of Willis

MIP Maximum Intensity Projection

4D 4-Dimensional

3D 3-Dimensional

2D 2-Dimensional

VO Vessel Orientation

Chapter 2

A Higher-Order Tensor Vessel Tractography for Segmentation of Vascular Structures:[1]

Extraction of vascular structures, such as coronary and cerebral arteries, is an important step in the detection and analysis of vessel anomalies and pathologies such as aneurysms, stenoses, and plaques. It is also significant to create accurate models for the blood flow analysis, functional assessment, surgical planning, and simulation. These models can also be used for quantitative assessment and geometrical analysis of the tubular structures in other domains. Manual segmentation is an exhausting task for experts. For computer-based segmentation, although tubularity can be represented by a fairly simple geometric model, the presence of branchings in vessels, the variation in tubular radii, and the non-rigid geometry bring additional challenges to the problem of automated creation of patient-specific vessel models from imaging data. Robust and fast vasculature segmentation remains one of the demanding problems in medical imaging.

[1]This chapter appeared as a journal article in *IEEE Transactions on Medical Imaging, Volume 34, Issue 10, pages 2172-2185, Oct. 2015.*

2.1 Literature Review

The existing vessel segmentation methods can be classified into two categories: model-free and model-based methods. Image filtering and enhancement methods have been proposed as model-free segmentation methods. Most well-known filtering techniques are based on the Hessian [30, 31, 32, 33, 34], non-linear diffusion [35, 36, 37], or flux-based filtering [38, 39]. A broad review of these methods can be found in [40, 41, 42, 43, 44, 45].

In the model-based approaches, explicit vessel models are applied to extract the vasculature. Two main model-based approaches are: (i) deformable models, particularly level-set representations [46, 47, 48], and (ii) tubular/cylindrical models [49, 50]. Lately, multi-hypotheses tracking [39, 50] and data driven [51] approaches have been proposed for the vascular segmentation problem. Friman et al. [50] proposed a tubular tracking algorithm based on 3D template matching, called Multiple Hypothesis Tracking, which was used to traverse difficult vessel passages, such as those caused by pathologies and areas of low contrast.

Minimal path techniques are another category of model-based vessel extraction [52, 53, 54, 55]. In [55], a flux-based anisotropic metric was utilized for the minimization of a path energy to extract vessel orientation and scale. The local metric used was based on the optimally oriented flux in [38]. In [54], the vessel was modeled as a curve whose coordinates correspond to the 3D centerline point plus the radius of the vessel. This approach considered isotropic measurements through a sphere fitted to a vessel. In contrast, we modeled the vessel orientation by adding cylinders in our earlier work [7], where an intensity-based rank-2 tensor was fit to a vessel, which mimicked DTI. The anisotropic tensor inside the vessel drove the segmentation analogously to a tractography approach in DTI. Our vessel tractography method [7] provided advantages in terms of incorporating vessel orientation information for modeling the whole vessel tree, while it had to employ a separate branch detection scheme in order to capture bifurcation points in a vessel tree. The latter is due to choice of a rank-2 tensor, which becomes isotropic in bifurcations of vessels.

Modeling of bifurcations in tree-like structure segmentation, in a seamless fashion, is

an open problem in vascular segmentation. One of the recent reviews [45] indicates that in automatic blood vessel segmentation bifurcation detection is one of the most challenging problems with only few papers specifically address bifurcation detection [56, 57, 58], and almost no work refer to n-furcation modeling. Baboiu and Hamarneh [56] proposed a bifurcation detection filter which is based on a scale-space conversion of the original image. They showed that the smallest eigenvalue of the Hessian matrix can detect bifurcations in both 2D and 3D. Generally, for the problem of patient-specific vascular tree modeling, an initial segmentation step that produces a 3D segmented volume has to be followed by a separate branch detection scheme. Later, it is used in creation of a vascular tree model, and sometimes followed by an external mesh construction scheme to model n-furcated vessels for mesh editing and further modeling [59, 60, 8]. Bogunovic et al. [8] presented anatomical labeling of Circle of Willis, mainly based on bifurcations of the cerebral arteries. An open-source toolkit TubeTK [61] was utilized for this purpose, which produced a set of disconnected centerlines, where the tracing failed close to bifurcations, which had to be separately handled.

Modeling WM tracts using DMRI faces challenges similar to modeling the vascular tree. The unimodal orientation distribution function (ODF) assumed by DTI (rank-2 tensor model) is no longer capable of resolving the orientation of distinct fiber populations within a voxel [62, 63]. To overcome this difficulty, Tuch et al. [62] proposed HARDI, which exploited imaging with diffusion-weighting gradients applied along many directions. Those directions are distributed isotropically on the unit 2-sphere, which can better represent the underlying fiber crossings. In addition to the usage of generalized HOTs in HARDI methods [63, 64], more flexible approaches via ODFs as an alternative for modeling crossings, were presented [65, 66, 67]. In [68], reconstruction of the ODF is reformulated in terms of spherical harmonic basis functions. In all the above HARDI models, an ODF or an iso-surface of the displacement probability profile is utilized to characterize the intra-voxel fiber structure without considering any inter-voxel information. The profiles obtained from these techniques are always anti-podally symmetric, thus only single fiber tracts or symmetric crossings can be modeled. However, neural fiber tracts may form asymmetric local structures such as in sprouting fibers [69]. In order to model

the sprouting or anti-symmetric crossing structures, Barmpoutis et al. [66] suggested an ODF field construction method by considering inter-voxel information, which requires a relatively higher number of diffusion directions. Schultz [70] demonstrated that HOTs indicating likely fiber directions can be estimated from a small number of diffusion-weighted measurements by taking into account information from local neighborhoods. Suggesting a HOT voting method, they demonstrated that the resulting even-order tensor fields facilitate fiber reconstruction at crossings both in synthetic and in real DW-MRI data, and that the odd-order fields differentiate crossings from junctions.

The beneficial mathematical modeling provided by HOTs was also used for feature extraction. Schultz et al. [71] presented a generalization of the traditional second-order model to a higher-order structure tensor (HOST), which was shown to model crossing edges in 2D images.

In analogy to fiber-crossing locations of white-matter, vascular structures include n-furcations, which are locations where n branches exit from the same vessel point, and hence have to be modeled properly. Inspired by the idea of generalized linear tensors in HARDI, we model the n-furcations of the vascular structures using a HOT, however embedding them in 4D, which is described in Section 2.3. Our technique brings a unified approach to the problem of whole vascular tree extraction, which includes simultaneous modeling of both tubular sections and n-furcations of the vascular structures. Experimental results are presented to demonstrate the performance of the proposed algorithm in Section 2.4, followed by discussions and conclusion in Section 2.5 and Section 2.6, respectively.

2.2 Mathematical Background

In HARDI methods, the diffusivity function $S(\boldsymbol{g})$ can be approximated by an m^{th} order Generalized Cartesian Tensor (GCT) in 3D as follows [63]:

$$S(\boldsymbol{g}) = \sum_{i=1}^{3}\sum_{j=1}^{3}\cdots\sum_{k=1}^{3}\sum_{l=1}^{3} g_i g_j \ldots g_k g_l D_{i,j,\ldots,k,l} \tag{2.1}$$

where g_i is the i^{th} component of the 3D unit vector $\boldsymbol{g} \in \mathbb{S}^2$, and $D_{i,j,\ldots k,l}$ are the tensor coefficients. The number of indices represents the order m of the tensor $\boldsymbol{D}$. As can be

observed, when m is odd: $S(-\boldsymbol{g})=-S(\boldsymbol{g})$, the GCT model forces negated measurements at the antipodal ends of the sphere. On the other hand, when m is even: $S(-\boldsymbol{g})=S(\boldsymbol{g})$ cannot model an antipodal asymmetric situation. For the HARDI application, this is not crucial, as the diffusion measurements are positive and symmetric on the sphere; therefore, even order tensors ($m=2,4,6$) are mostly utilized.

In our problem, a GCT in 3D cannot model the geometry of the vessel, which is symmetric along the vessel and asymmetric at the bifurcations. We illustrate this in Figure 2.1 on a Y-shaped vessel [72] with $m=2,3,4$th order tensors estimated by a linear least squares fit to $S(\boldsymbol{g})$. In Figure 2.1(a), the measurements $S(\boldsymbol{g})$ taken from multiple orientations (described in Section 2.3.2) for a Y-shaped vessel are depicted; in (b) are the corresponding rank-2 tensors fit to $S(\boldsymbol{g})$. As can be observed, although tubular parts of the vessel are correctly represented, rank-2 tensors are not able to model the geometry of bifurcations. Similarly, a rank-4 tensor will not represent the correct geometry of a bifurcation (Figure 2.1(d)). Furthermore, odd-order GCT in 3D enforces negative measurements at the opposing directions and, therefore, is not suitable in this case either (Figure 2.1(c)).

2.3 Method

The proposed method for vascular structure segmentation, which we call HOT vessel tractography, is summarized in a flowchart in Figure 2.2. As an initialization, we start with a user defined single seed point and estimate the radius at the seed using the maximum tensor norm criterion in [7]. Then we create vessel measurements as explained in Section 2.3.2 and fit 4D tensors to those in Section 2.3.1. We extract the vessel directions using the techniques described in Section 2.3.3 and advance to the next centerline point based on the detected vessel directions. In the last step, we estimate the radius along the vessel orientation as described in Section 2.3.4.

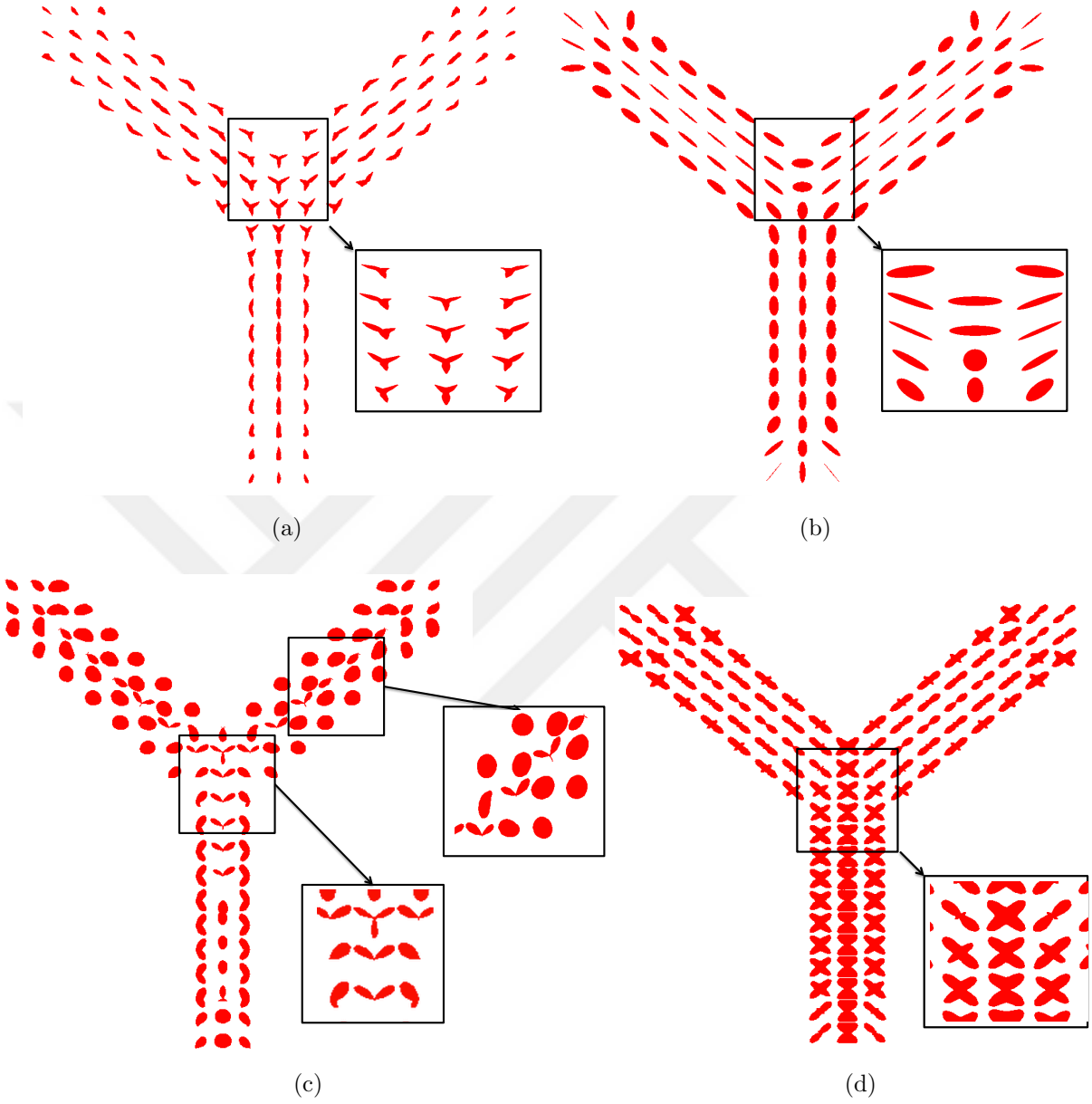


Figure 2.1: $60 \times 60 \times 60$ *synthetic Y-junction volume: Comparison between* $S(\boldsymbol{g})$ *measurements (a), and their rank-2 (b), rank-3 (c), and rank-4 (d) tensor fit model in 3D. Neither of these Cartesian tensor models in 3D are capable of modeling the whole vessel structure.*

2.3.1 Higher Order Tensor (HOT) Model in 4D

We propose a 4D higher order tensor which is able to model both antipodal asymmetry and the symmetry of a vessel n-furcation, where the fourth dimension along g_4 will be used to suppress the components in unwanted directions such as in the opposing directions of

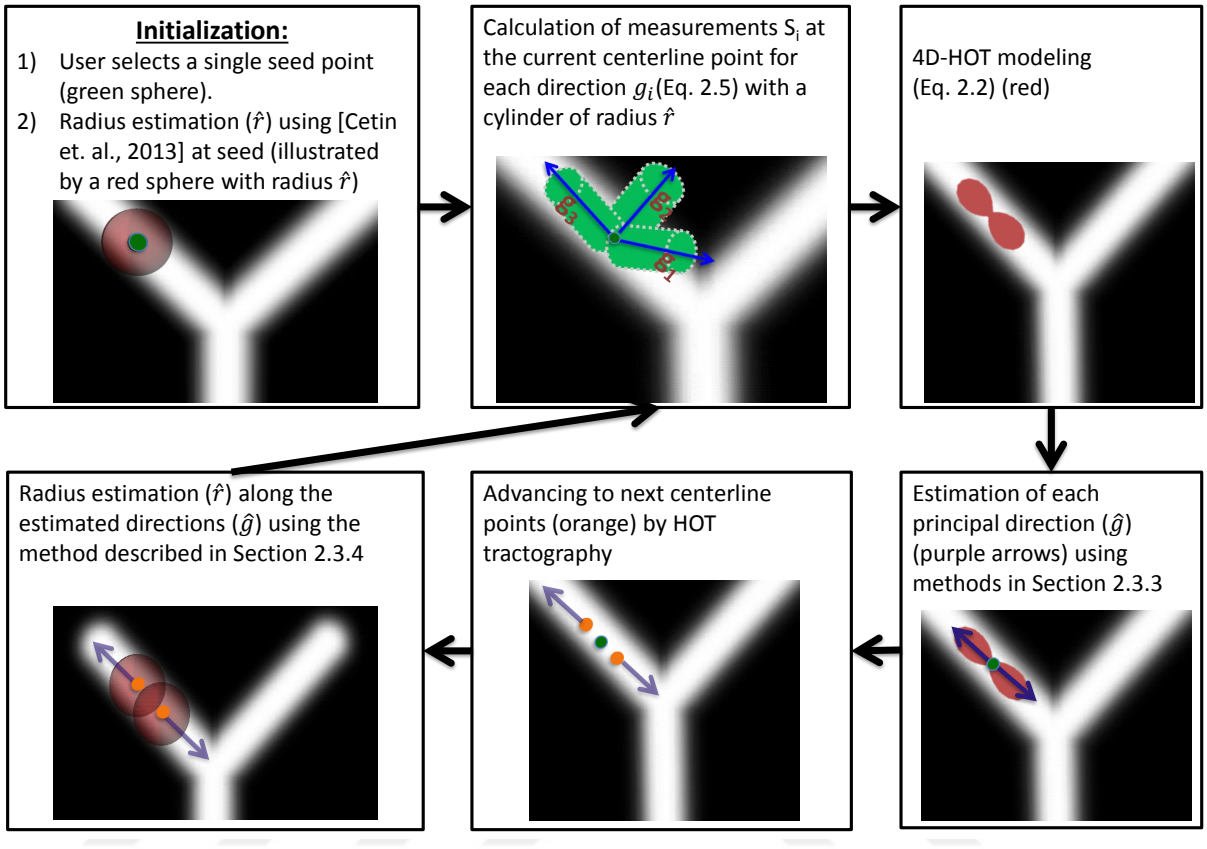


Figure 2.2: *Flowchart of the proposed HOT Vessel Tractography method.*

Y-junction branches. Mathematically, our m^{th} order tensor model in 4D is described as:

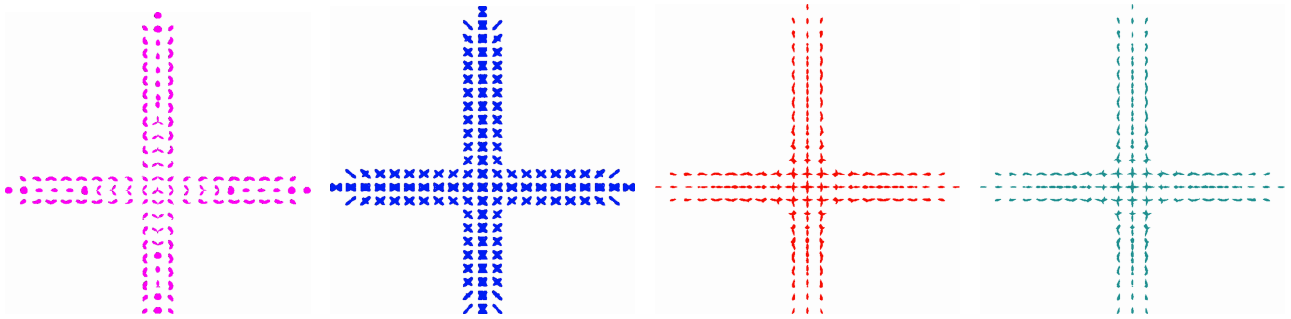
$$S(\boldsymbol{g}) = \sum_{i=1}^{4}\sum_{j=1}^{4}\cdots\sum_{k=1}^{4}\sum_{l=1}^{4} g_i g_j \ldots g_k g_l D_{i,j,\ldots,k,l} \tag{2.2}$$

where $S(\boldsymbol{g})$ is a measurement[2], $\boldsymbol{g} = [g_1, g_2, g_3]$ is an orientation vector on the unit sphere $\mathbb{S}^2$, and g_4 is defined with a sigmoid function as follows:

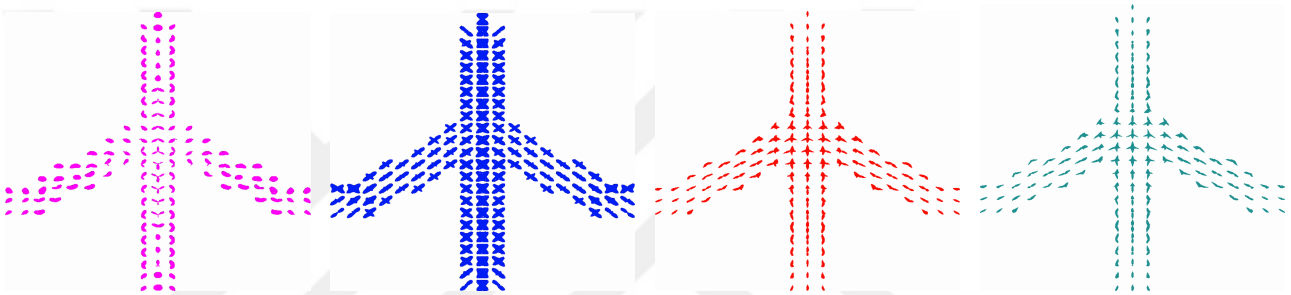
$$g_4(\boldsymbol{g}) = \frac{1}{1 + e^{-a(S(\boldsymbol{g})-c)}} \tag{2.3}$$

where $a > 0$, and $c > 0$. Note that this model in 4D lifts the limitation with symmetry of measurements, and one can have arbitrary measurements at $\boldsymbol{g}$ and $-\boldsymbol{g}$ directions for an odd order tensor in 4D. The sigmoid function in Eq.(2.3) is designed as a high-pass filter that sharpens the measurements along the directions of the vessel and the branches. Even though an even-order tensor still has an antipodal symmetry, the 4th component in 4D,

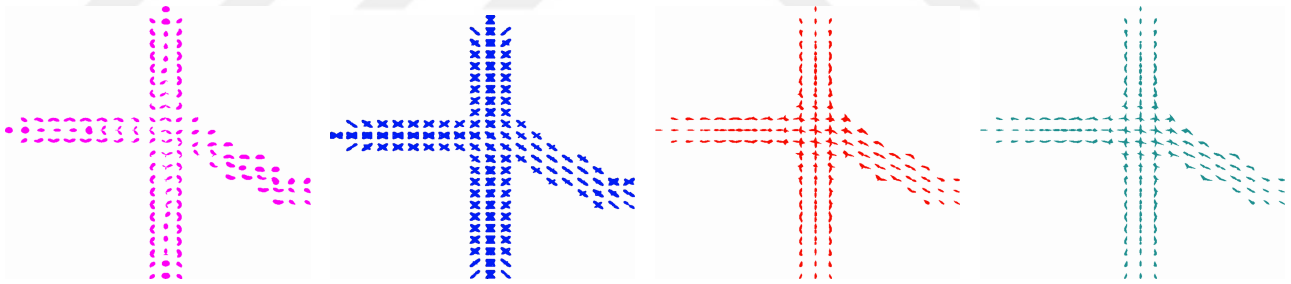
[2]Measurement model that represents the vessel structure will be described in Section 2.3.2.



(a) 3^{rd} Order Tensor Fitting in 3D (b) 4^{th} Order Tensor Fitting in 3D (c) 3^{rd} Order Tensor Fitting in 4D (d) 4^{th} Order Tensor Fitting in 4D



(e) (f) (g) (h)



(i) (j) (k) (l)

Figure 2.3: *Each row illustrates a different type of n-furcation (first row for the crossing vessels, second row for modeling trifurcation, and the last row depicts asymmetric trifurcation.). Each column represents 3D/4D third or fourth order tensors: Left: fitting measurements to the 3D third order tensor model (purple); Second from Left: 3D fourth order tensor model (blue); Second from Right: 4D third order tensor model (orange); Right: 4D fourth order tensor model (green). 4D tensors are projected to 3D after decomposition (Section 2.3.3) for visualization.*

which acts like a measurement filter, helps in the estimation of the main branch directions in an n-furcation. Now, we define a 4D vector $\boldsymbol{p} = [g_1, g_2, g_3, g_4]$, and we normalize, $\hat{\boldsymbol{p}} = \frac{\boldsymbol{p}}{\|\boldsymbol{p}\|}$, to obtain a mapping $\mathbb{R}^4 \rightarrow \mathbb{S}^3$. Note that the orientation vectors $\hat{\boldsymbol{p}}$ lie on the unit sphere $\mathbb{S}^3$, which carry the tensor modeling to 4D space. The 4D space constructed on $\mathbb{S}^3$ is crucial to our method, which is achieved by the g_4 coordinate. Other forms of g_4 would work as well, as long as they provide suppression of measurements when the image is not symmetric along $\boldsymbol{g}$.

In Figure 2.3, each row depicts a different type of junction. The first and second columns represent the results of third-order and fourth-order tensor fitting to the junction measurements in 3D, respectively. The last two columns illustrate the results of third and fourth order tensor fitting in 4D, respectively. As can be observed, although third or fourth order tensor fitting in 3D are not suitable for modeling the vessel n-furcations, the latter can be modeled using higher order tensors in 4D.

2.3.2 A Flux-based Measurement Model

Our geometric measurement model to calculate $S(\boldsymbol{g})$ (left hand side of Eq.(2.2)) is depicted in Figure 2.4.

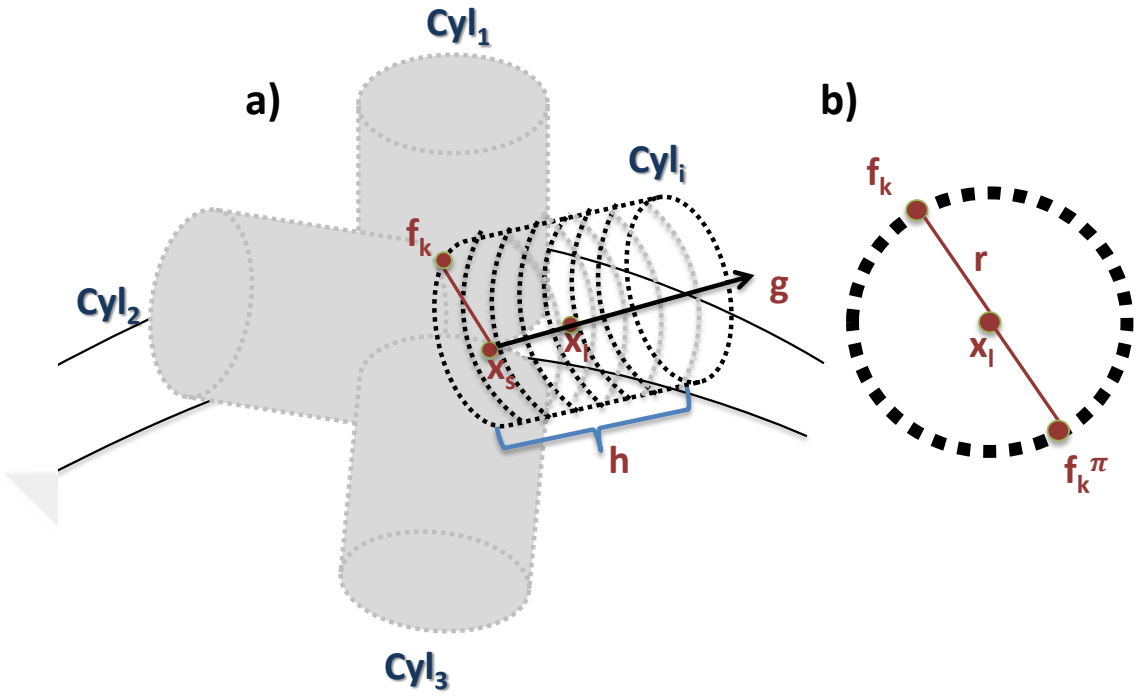


Figure 2.4: *Illustrations of: (a) directional measurement model: each Cyl_i is characterized by the direction vector $\boldsymbol{g}$, the height h, and the circle centered at point $\boldsymbol{x}_l$ with radius r, $\boldsymbol{x}_s$ is the center point on the base circle of the cylinder; (b) cross sectional view of the cylindrical model.*

It consists of a hollow cylinder along each sampled orientation $\boldsymbol{g}$, and is represented by a stack of circles denoted as follows:

$$cyl(\boldsymbol{g}) = \bigcup_{l=0,\cdots,h} circle(\boldsymbol{x}_l, r, \boldsymbol{g}), \qquad \boldsymbol{x}_l = \boldsymbol{x}_s + \boldsymbol{g}\, l, \tag{2.4}$$

where $\boldsymbol{x}_s \in \mathbb{R}^3$ is the current vessel centerline point. $\boldsymbol{x}_l \in \mathbb{R}^3$ is defined as a point along the centerline of the cylinder, $\boldsymbol{g}$ also indicates the normal vector to the circle: $circle(\boldsymbol{x}_l, r, \boldsymbol{g})$ with radius r, and h is defined as the height of the cylinder. Circles that define the cylinder are equi-angularly discretized into M points in polar coordinates.

Each measurement $S(\boldsymbol{g})$ at the given direction $\boldsymbol{g}$ is modeled as a flux-based feature, which is created by an accumulation of image gradient magnitudes. Mathematically, the

measurements along the cylinder $cyl(\boldsymbol{g})$ are calculated as follows:

$$S(\boldsymbol{g}) = \sum_{l=0}^{h} \left(\sum_{k=1}^{M/2} max(|< \nabla I(\boldsymbol{f}_k), \boldsymbol{u}_k >|, |< \nabla I(\boldsymbol{f}_k^{\pi}), \boldsymbol{u}_k^{\pi} >|) \right), \tag{2.5}$$

where $\nabla I(\boldsymbol{f}_k)$ is the image gradient vector at the sampled point $\boldsymbol{f}_k$ and $\boldsymbol{u}_k = \frac{\boldsymbol{x_l} - \boldsymbol{f}_k}{|\boldsymbol{x_l} - \boldsymbol{f}_k|}$ (Figure 2.4-b). To minimize the effects of the bright structures situated near the vessels, we pair diametrically opposed points as suggested in [39], $\boldsymbol{f}_{\frac{M}{2}+k} = \boldsymbol{f}_k^{\pi}$. Although the idea is similar to the original flux function [39], which calculates the flux around a cross section, our measurements are less sensitive to noise due to the introduced cylindrical model. The flux-based measurements $S(\boldsymbol{g})$ for each $\boldsymbol{g}$ are computed, and used in the tensor estimation as described next.

2.3.3 Higher Order Tensor Fitting and Decomposition

We exemplify our method with $m = 4^{th}$ order tensor estimation in 4D and define $S_i = S(\boldsymbol{g})$ for matrix representation of $S(\boldsymbol{g})$, where $i \in [1, N]$ and N is the number orientation vectors sampled over the unit sphere $\mathbb{S}^2$. To estimate a 4D fourth order tensor from the flux measurements S_i using a least squares technique, first, we stack the components of the tensor, and due to permutational symmetry (e.g. $D_{1112} = D_{1121} = D_{1211} = D_{2111}$), there exist 35 components in total:

$$\begin{aligned} \boldsymbol{d} = [&D_{1111} \quad D_{2222} \quad D_{3333} \quad D_{4444} \quad D_{1112} \\ &D_{1113} \quad D_{1114} \quad D_{2221} \quad D_{2223} \cdots D_{1234}]^T \end{aligned} \tag{2.6}$$

We re-arrange Eq. (2.2) to get

$$S_i = \boldsymbol{G}_i \boldsymbol{d}\,, \tag{2.7}$$

where $\boldsymbol{G}_i$ is the i^{th} row of the matrix, which is constructed as follows:

$$\begin{aligned} \boldsymbol{G_i} = [&g_{i1}^4 \quad g_{i2}^4 \quad g_{i3}^4 \quad g_{i4}^4 \quad 4g_{i1}^3 g_{i2} \quad 4g_{i1}^3 g_{i3} \quad \cdots \\ &4g_{i1}^3 g_{i4} \quad 4g_{i2}^3 g_{i1} \quad 4g_{i2}^3 g_{i3} \quad 24 g_{i1} g_{i2} g_{i3} g_{i4}] \end{aligned} \tag{2.8}$$

The tensor components $\boldsymbol{d}$ are estimated via a least-squares estimator from Eq.(2.7).

In 3D, tensors with different orders are used for modeling physical quantities such as strain, diffusion and curvature. Depending on the physical quantity that is being

modeled, positivity constraint should be satisfied for the estimated tensors. The constraint can be satisfied only with even order tensors as shown in [73]. In HARDI applications, the simplest approach for estimation of the coefficients of an HOT entails a solution to the over-determined linear least squares inverse problem [63]. As stated in [74], although this method is fast and is not limited to 4^{th} order diffusion tensors, it does not guarantee positive diffusivity, $D(\boldsymbol{g}) > 0, \quad \forall \boldsymbol{g} \quad st \quad \|\boldsymbol{g}\| = 1$. Another method used in HARDI applications is the ternary quartic of [73], where Hilbert's theorem is applied on non-negative ternary quartics to express the diffusivity function as $D(\boldsymbol{g}) = (\boldsymbol{u}^T \boldsymbol{q}_1)^2 + (\boldsymbol{u}^T \boldsymbol{q}_2)^2 + (\boldsymbol{u}^T \boldsymbol{q}_3)^2 = \boldsymbol{u}^T \boldsymbol{Q}\boldsymbol{Q}^T \boldsymbol{u}$, Q is estimated from the HARDI acquisitions, and the coefficients of the 4^{th} order diffusion tensor are extracted from $\boldsymbol{Q}\boldsymbol{Q}^T$. Also, a spherical harmonics approach [75], which does not assure positive diffusivity, and a Riemannian approach [74] were suggested to estimate the positive definite tensor coefficients of even order tensors in 3D.

Previously proposed HARDI methods in literature cannot be used to enforce positive definiteness in our 4D general Cartesian tensor model since we do not impose a constraint on neither the order of the tensor nor its evenness [73, 75, 74]. Instead, we utilized a non-negative least squares fitting to estimate the tensor components. In order to monitor whether the estimated m^{th} order 4D tensors are positive definite, we use Z-eigenvalue and Z-eigenvector method presented in [76]:

$$\boldsymbol{D}\,\hat{\boldsymbol{p}}^{\,m-1} = \lambda \hat{\boldsymbol{p}} \quad s.t. \quad \hat{\boldsymbol{p}}^{\,T}\hat{\boldsymbol{p}} = 1, \tag{2.9}$$

where $\lambda \in \mathbb{R}$ is called a Z-eigenvalue and $\hat{\boldsymbol{p}}$ is called a Z-eigenvector of $\boldsymbol{D}$ if they are solutions to Eq. (2.9). It is well known that non-negative least squares fitting does not ensure positive definiteness, however, by computing the Z-eigenvalues of the constructed tensors, we observed that it provided positive definiteness for all cases in our application.

At this point, we have a $\boldsymbol{D}_{4\times4\times4\times4}$ tensor, which models the vessel in 4D. Next, the question is how to make use of the 4D tensor for vascular n-furcation modeling. We propose to decompose the tensor into its components to unveil the n-furcating paths or branches of the vessel. In order to do that, we adapted two approaches, which are explained next.

2.3.3.1 Higher Order Orthogonal Iteration

After going up higher in the dimension, in order to come back to the vessel physical space we decompose the tensor to find its principal directions. As a Higher Order Tensor Decomposition method [77], we utilize a higher-order extension of matrix singular value decomposition (Tucker decomposition) that computes the orthonormal spaces associated with the different axes (or modes) of a tensor [78]. The Tucker decomposition of an $M \times N \times P \times Q$ (for our case, $M = N = P = Q = 4$) tensor $\boldsymbol{D}$ of order 4 is given by:

$$\boldsymbol{D} = \sum_{I=1}^{M} \sum_{J=1}^{N} \sum_{K=1}^{P} \sum_{L=1}^{Q} \boldsymbol{\Lambda}_{IJKL} \boldsymbol{U}_{iI} \otimes \boldsymbol{V}_{jJ} \otimes \boldsymbol{W}_{kK} \otimes \boldsymbol{Z}_{lL} \tag{2.10}$$

where $\otimes$ denotes the tensor (or outer) product: $\boldsymbol{x} \otimes \boldsymbol{y} \triangleq \boldsymbol{x}\boldsymbol{y}^{\boldsymbol{T}}$. The matrices $\boldsymbol{U}$, $\boldsymbol{V}$, $\boldsymbol{W}$, and $\boldsymbol{Z}$ are orthogonal, and keep the modes of the tensor. $\boldsymbol{\Lambda}$ keeps the eigenvalues. Matrix slices of $\boldsymbol{\Lambda}$ along any mode are chosen to be mutually orthogonal with a decreasing Frobenius norm. In this case, the Tucker decomposition is called the Higher Order Singular Value Decomposition (HOSVD), which can be viewed as a generalization of the classical SVD for tensors (See Algorithm 2).

It is well known that the HOSVD is not optimal for giving the best fit which is computed by the norm of the difference. However, it is a good initialization point for an iterative Alternating Least Squares (ALS) algorithm [77]. [79] proposed an efficient ALS technique by computing only the dominant singular vectors of the higher order tensor which is called Higher Order Orthogonal Iteration (HOOI) method. Let $\boldsymbol{D}$ be an n^{th}-order tensor of size $S_1 \times S_2 \times \cdots \times S_n$. The n-rank of $\boldsymbol{D}$, which can be defined as $R_n = rank_n(\boldsymbol{D})$, $R_n \leq S_n$ (See Algorithm 1).

2.3.3.2 Finding Rank-1 Approximation

As a second method for higher order tensor decomposition, we utilized the best $rank_1$ approximation technique described in [6]. The goal of the algorithm is the decomposition of the HOT representation of the ODF into an several parts: isotropic part; several $rank_1$ modes that represent the individual fiber peaks; a small residual, which covers outliers such as noise and other factors outside the model (See Figure 2.5).

Algorithm 1 *Higher Order Singular Value Decompostion (HOSVD) for computing a rank−$(R_1, R_2, \cdots, R_n)$ tensor $\boldsymbol{D}$.*

function HOSVD($\mathbf{D}$, R_1, R_2, $\cdots$, R_n)

for $n = 1, \cdots, n$ **do**

$\mathbf{C^{(n)}} \leftarrow \mathbf{R_n}$ leading left singular vectors of $\mathbf{D_{(n)}}$

end for

$\mathbf{H} \leftarrow \mathbf{D} d_1 \mathbf{C}^{(1)T} d_2 \mathbf{C}^{(2)T} \cdots d_n \mathbf{C}^{(n)T}$ // $\mathbf{H}$ is called the core tensor

return $\mathbf{H}, \mathbf{C}^{(1)}, \mathbf{C}^{(2)}, \cdots, \mathbf{C}^{(n)}$

end function

Algorithm 2 *HOOI algorithm which computes a rank−$(R_1, R_2, \cdots, R_n)$ Tucker decomposition for an $n^{th}-$order tensor $\mathbf{D}$ of size $S_1 \times S_2 \times \cdots \times S_n$.*

function HOOI($\mathbf{D}$, R_1, R_2, $\cdots$, R_n)

initialize: $C^{(n)} \in \mathbb{R}^{S_n \times \Omega}$ for $n = 1, \cdots, n$ using HOSVD

repeat

for $n = 1, \cdots, N$ **do**

$\mathbf{W} \leftarrow \mathbf{D} d_1 \mathbf{C}^{(1)T} \cdots d_{n-1} C^{(n-1)T} d_{n+1} C^{(n+1)T}$

$\cdots d_n C^{(n)T}$

end for

until fit ceases to improve or maximum iterations

$\mathbf{H} \leftarrow \mathbf{D} d_1 \mathbf{C}^{(1)T} d_2 \mathbf{C}^{(2)T} \cdots d_n \mathbf{C}^{(n)T}$ // $\mathbf{H}$ is called the core tensor

return $\mathbf{H}, \mathbf{C}^{(1)}, \mathbf{C}^{(2)}, \cdots, \mathbf{C}^{(n)}$

end function

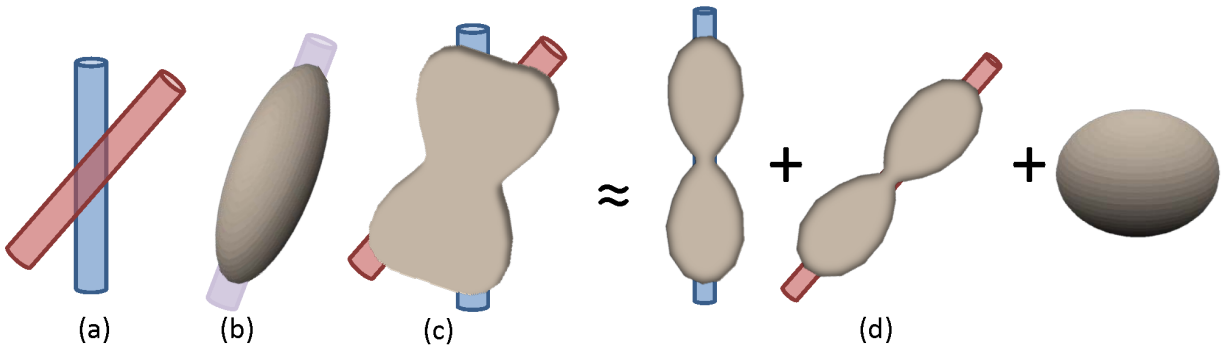


Figure 2.5: *Higher-order tensor representation of the ODF by a rank-1 approximation: (a) Two crossing fibers example; (b) DTI representation of crossing fibers; (c) the ODF model; (d) Two rank-1 terms and an isotropic part. (Fig. adapted from [6].)*

Algorithm 3 adapted from (Schultz et al. [6]) works iteratively: Initially, the full input ODF $\mathbf{S}$ is calculated by the estimated 4^{th} order using the Eq. 2.2 and is assigned to the residual $\Re$. In the first step, the isotropic part of $\Re$ is estimated via calculating the mean of $\mathbf{S}$, $\mu = mean(\Re)$. Then, it is multiplied by the isotropic ODF $\mathbf{I}$. A rank-f approximation of $\Re$ is found by following: f is the number of fiber tracts to be estimated, $\bar{\mathbf{F}}_i$ is its ODF representation. They estimate $\bar{\mathbf{F}}_i$ by an iterative local optimization. It repeatedly optimizes each rank-1 term, while keeping all others terms fixed. To add a new term, a rank-1 approximation $approx(\Re)$ of $\Re$ is applied: an existing rank-1 term $\bar{\mathbf{F}}_i$ is improved, then they seek an approximation of $\Re+\bar{\mathbf{F}}_i$. Later, they begin a gradient descent at the former optimum $\mathbf{u}$, defined as $refine(\mathbf{u}, \Re + \bar{\mathbf{F}}_i)$. Residual norm $\|\Re\|$ is reduced in each step of the algorithm. This procedure is repeated until the residual norm no longer changes significantly.

Figure 2.6 depicts the detected eigen-directions (green) of the higher order tensors (red) on synthetic Y and T junction volumes. Modes of the tensors along the centerline are depicted by blue. Although the tensors become perturbed along the edges, they correctly represent the expected geometry along the centerline of the vessel. Estimated modes of the Figure 2.7 show demonstrations on synthetic trifurcation volumes. As it can be observed, the directions for all branches of the junction structures are reliably extracted by the proposed technique.

Algorithm 3 *Pseudocode of Rank-1 approximation algorithm.*

function HOOI($\mathbf{S}$, f_{max})

Inputs and parameters: $\mathbf{S}$ is the ODF to be decomposed, f_{max} is the number of fibers to be extracted.

Output: $\bar{\mathbf{F}}_i$ is the final fiber ODF for each term i.

Important variables: $\mathbf{F}_i^{(n)}$ is the fiber i at iteration n. $\mathbf{u}_i^{(n)}$ is the vector of $\mathbf{F}_i^{(n)}$. f is the current number of fibers. $\Re$ is the current residual and $\Re^{(n)}$ is the residual before inner iteration n.

Constants: $\mathbf{I}$ is the identity matrix, ϵ is a small scalar value greater than zero.

Initialization: $\Re = \Re^{(1)} = \mathbf{S}$, $f = 1$, $n = 1$;

repeat//outer iteration

repeat//inner iteration

$\Re = \Re - \mu(\Re).\mathbf{I}$ // estimation of isotropic part

for $i = 1, \cdots, f$ **do** //for all number of f fiber terms

if $\mathbf{F}_i^{(n)}$ is defined **then**

$\mathbf{F}_i^{(n+1)} = refine(\mathbf{u}_i^{(n)}, \Re + \mathbf{F}_i^{(n)})$;

else

$\mathbf{F}_i^{(n+1)} = approx(\Re)$;

end if

end for

$n = n + 1$; $\Re^{(n)} = \Re$;

until $\left\|\Re^{(n)}\right\| > (1 - \epsilon) \cdot \left\|\Re^{(n-1)}\right\|$ // test convergence

if accept($\mathbf{F}_i^{(n)}$) **then**//accept f fiber terms

for $i = 1, \cdots, f$ **do**// store output candidates

$\bar{\mathbf{F}}_i = \mathbf{F}_i^{(n)}$;

end for

end if

until $f > f_{max}$ or not accept($\mathbf{F}_i^{(n)}$)

end function

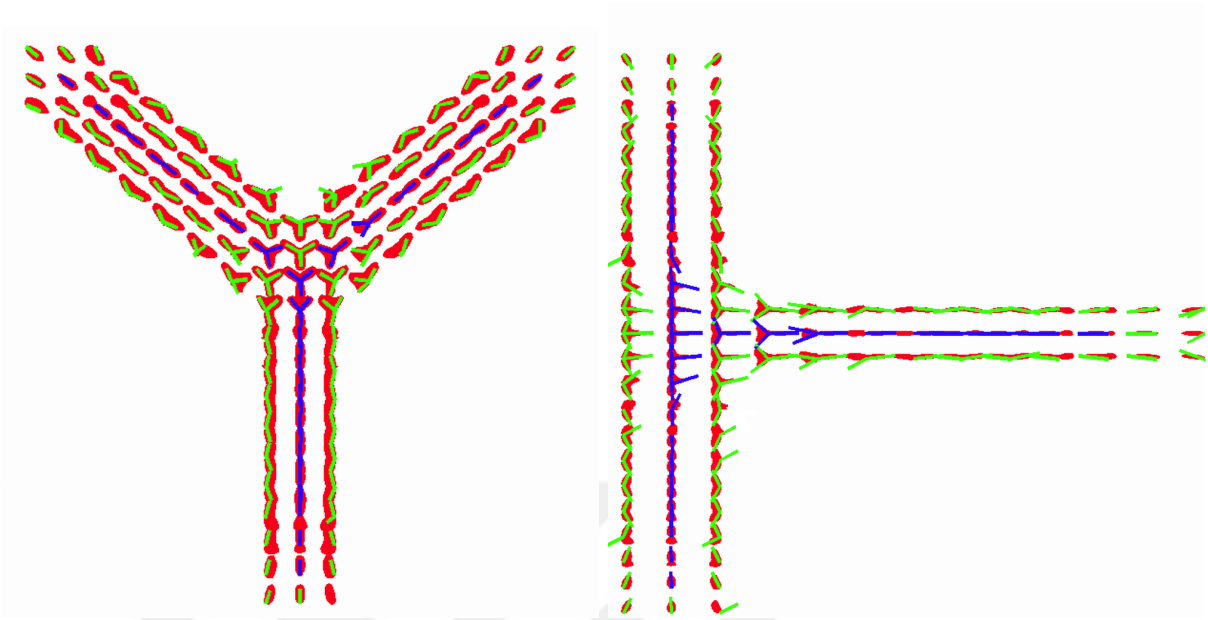


Figure 2.6: *Estimated modes (green) of the higher order tensors (red) are shown on synthetic Y-junction and T-junction volumes. Modes of the tensors along the centerline are depicted by blue.*

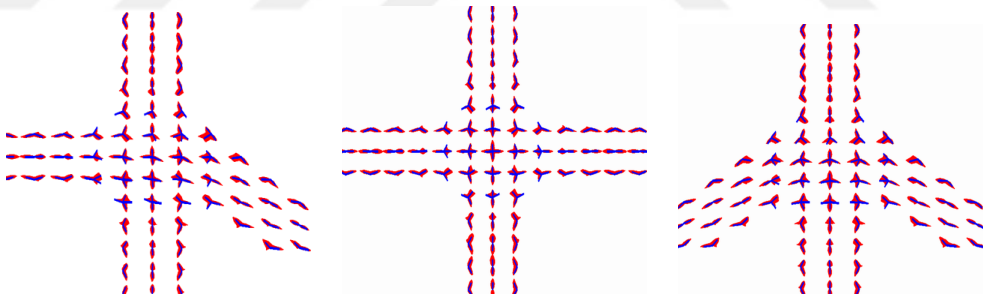


Figure 2.7: *Estimated modes (blue) of the higher order tensors (red) are shown on synthetic asymmetric-junction, crossing junction, and trifurcation volumes.*

2.3.4 Vessel Lumen Thickness Estimation

The thickness of the vessel lumen is directly related to the radius of the cylinder, as the lumen radius is to be obtained when there is a perfect fit of the model to the data. When the diameter of the cylinder is below or above the true vessel lumen thickness, the measurement S_i^r for a certain radius r decreases. Thus S_i^r is largest when the cylinder is tangent and along the direction of vessel $\hat{\boldsymbol{g}}$ (See Figure 2.8).

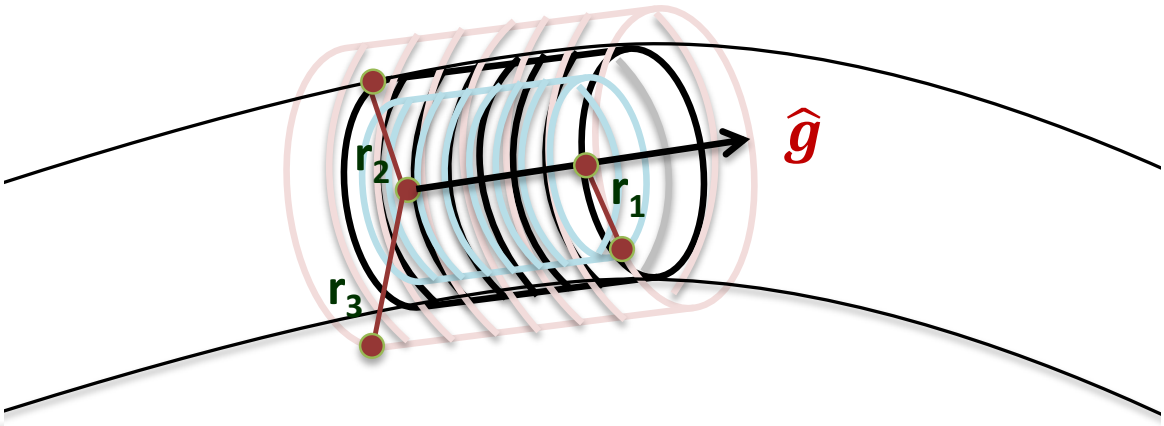


Figure 2.8: *Illustration of the vessel lumen thickness estimation: multiple cylinders are fitted and "best fit radius" is calculated using Eq. (2.11).*

The measurements are first estimated for multiple radii, $S^r_{\hat{\boldsymbol{g}}}$, as in Eq. (2.5), but by replacing the first sum to run between $l = -r, ..., r$. The "best radius" is then selected as follows:

$$\hat{r} = \underset{r \in [r_{min}, r_{max}]}{\arg\max} \left\| S^r_{\hat{\boldsymbol{g}}} \right\|, \tag{2.11}$$

$S^r_{\hat{\boldsymbol{g}}}$ denotes the measurement calculated from the cylindrical flux based model (Section 2.3.2) along the estimated vessel direction $\hat{\boldsymbol{g}}$ (Section 2.3.3) with a given r.

2.3.5 Implementation Details

As illustrated in the flowchart in Figure 2.2, the algorithm starts from a user selected seed point, preferably chosen from a high contrast region over a vessel (except for junction points). As an initialization step, we fit a second-order tensor to estimate the radius of the seed point [7]. In the following steps, we utilize a higher order tensor fitting method to find the directions of the vessel as explained in Sections 2.3.1, 2.3.2, and 2.3.3. Next, based on the estimated directions, which are projected to 3D, an advanced HOT tractography technique in [80] is utilized to trace the vessel centerline. In order to correct possible voxel perturbation errors on the centerline, we apply the procedure in [7], which centralizes the vessel centerline coordinate after each tractography advance step. We estimate the

thickness of the vessel lumen using the method explained in Section 2.3.4. These steps are repeated at each centerline point until all estimated directions are traced and the end of the vessel, according to simple stopping criteria in [7], is reached. Parameters a and c in Eq.(2.3) are heuristically fixed to 1 and 0.5, and $h = 4r$ is selected as the cylinder height in Eq.(2.5) for all the experiments, as they are observed to be robust parameters across applications in this study.

For a human coronary artery segmentation application, to cover the typical vessel radius range, values are selected from $r_{min} = 0.25mm$ to $r_{max} = 4.0mm$ with a fixed step of $0.25mm$ in radius estimation. Since the calcifications are not part of the vessel lumen, we remove calcifications using the technique described in [7] as a preprocessing step.

For a cerebral artery segmentation application, values are selected from $r_{min} = 0.25mm$ to $r_{max} = 5.0mm$ with the same fixed step of $0.25mm$. 64 and 128 (parameter N in Section 2.3.3) unit directions on $\mathbb{S}^2$ mapped to $\mathbb{S}^3$ are used in tensor fitting for the decomposition methods in Sections 2.3.3.1 and 2.3.3.2 respectively.

2.4 Experiments and Results

We evaluated the proposed method on three different datasets: (i) synthetically created vascular trees; (ii) coronary arteries in CTA data; (iii) cerebral arteries in MRA data. We used four different quantitative measures as True Positives: $TP = |E \cap R|/|R|$, False Negatives: $FN = (|R| - |E \cap R|)/|R|$, False Positives: $FP = (|E| - |E \cap R|)/|R|$ and Overlap Measure: $OM = 2|E \cap R|/(|E| + |R|)$ between the estimated vessel point set E and the reference vessel point set R, and $|\cdot|$ denotes the cardinality of the set E or R.

2.4.1 Method Validation

2.4.1.1 Synthetic data

We first evaluate the proposed HOT vessel tractography on 20 synthetic vascular im-

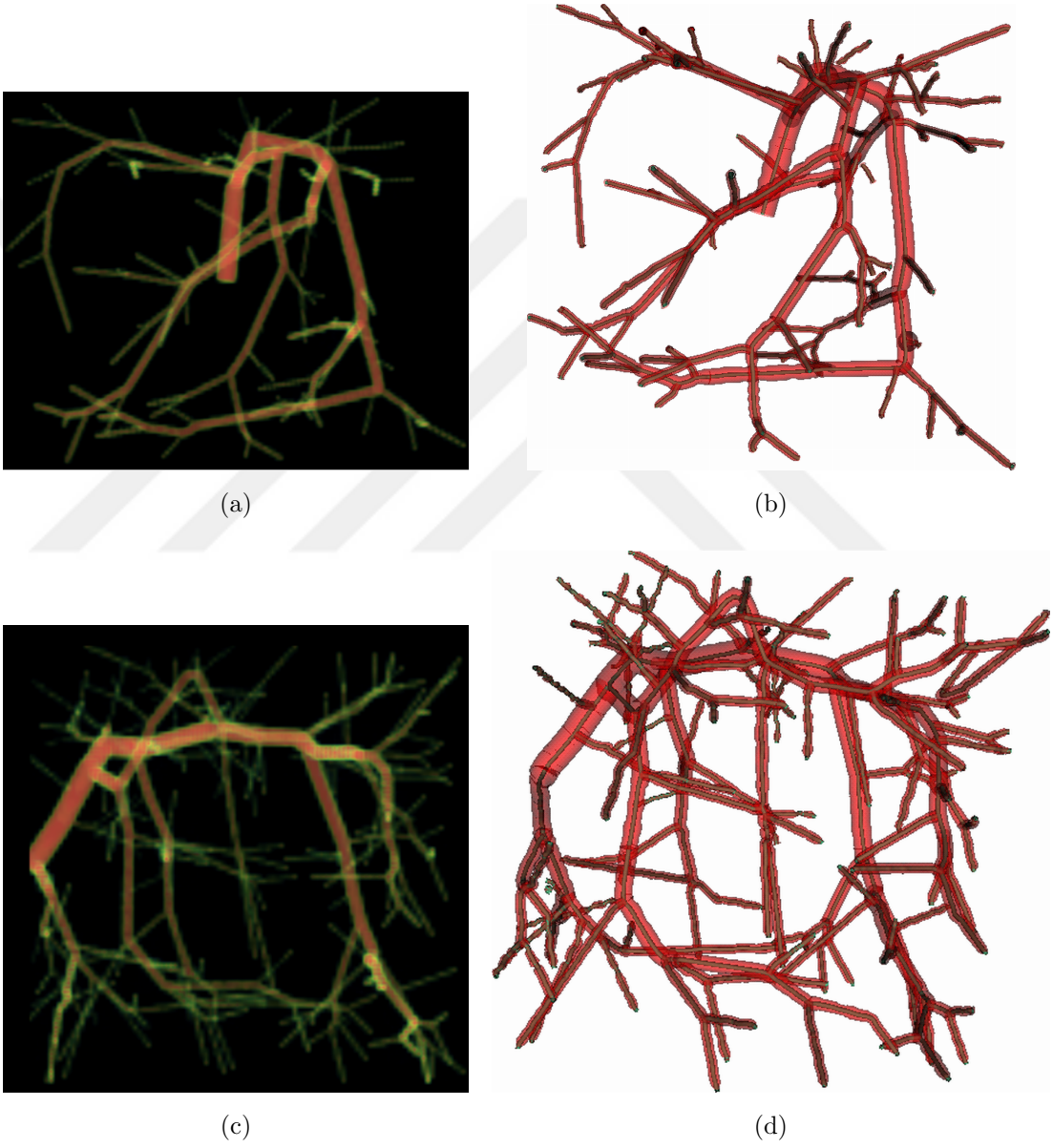
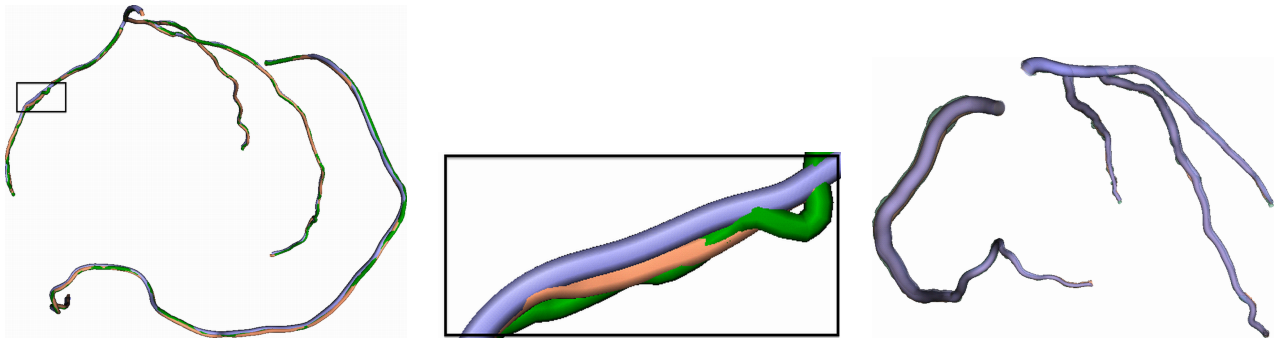


Figure 2.9: *(a,c) MIP views of VascuSynth dataset 1 and 3, respectively; (b) Extracted vessel tree for synthetic dataset 1; (d) Extracted vessel tree for synthetic dataset 3; Centerline of the vessel (green), extracted surface surrounds centerline (red) are depicted.*



(a) (b) (c)

Figure 2.10: *Segmentation results from Rotterdam dataset 6 (from training database). Orange: results for the new method; Green: results for the earlier method [7]; Violet: reference; (a) Extracted centerline, previous method's result and reference centerline; (b) Zoomed view of a segment where the two methods, particularly the earlier one deviate from the reference; (c) Extracted radii, previous method's radii and reference radii are rendered around the centerline.*

ages with known ground truth. The "VascuSynth" synthetic data simulate the volumetric images of vascular trees with varying contrast [81]. Each tree includes between 49 and 499 branches, 282 branches on average. Dice overlap (OM), and the percentage of detected branches in the vessel tree, (number of detected branches / total number of branches)$\times$100%, are computed to evaluate the performance.

Figure 2.9 (b, d) shows the extracted centerlines of the vessel trees with their vessel thickness values as surface renderings. After selecting a single seed on one of the branches, our algorithm extracts the entire tree automatically. Over this set of 20 synthetic data, on average, $95.63 \pm 2.44\%$ OM ratio is obtained, and $98.13 \pm 1.46\%$ number of branches are detected. On the other hand, our previous method [7] obtained a $93.62 \pm 2.77\%$ OM ratio, and $95.91 \pm 2.21\%$ number of branches. The differences are statistically significant for both metrics with a significance level of 0.05 (p=5.2372e-07 for OM and p= 0.00018507 for % number of branches).

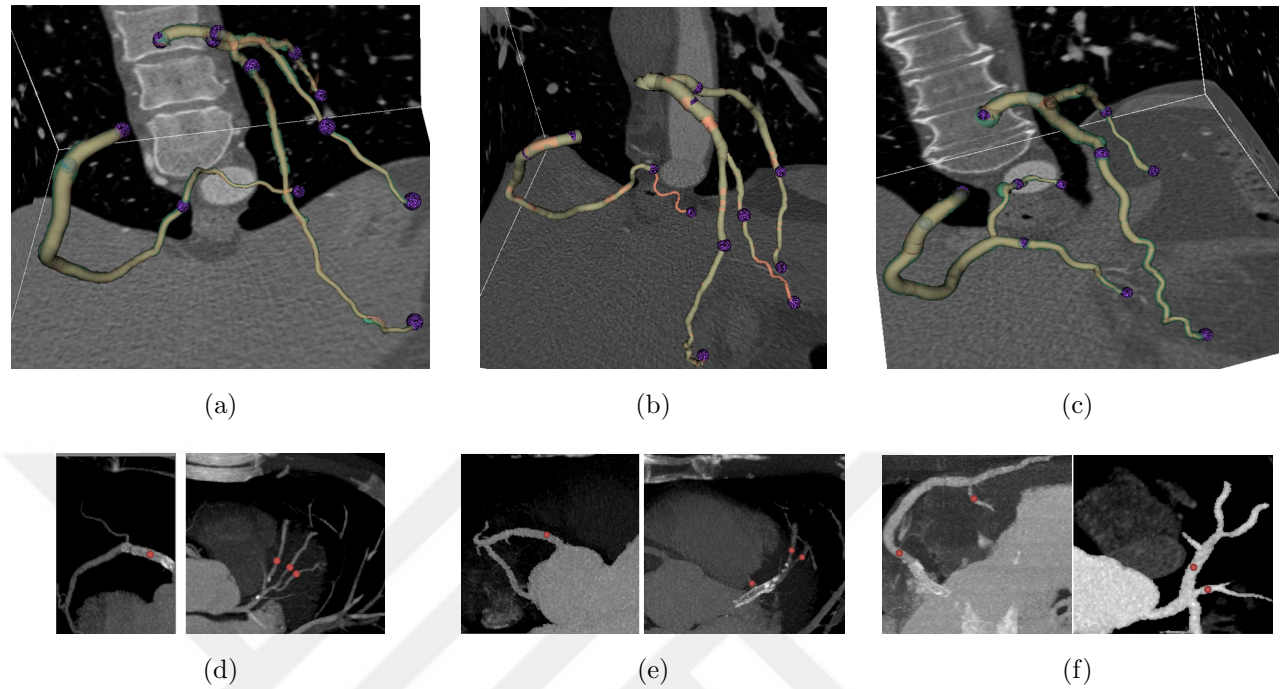


Figure 2.11: *(Top row) Segmented arteries from the earlier method [7] and the new method are shown for Rotterdam datasets 16, 22 and 30 with anatomical views; (Bottom row) MIP views of the datasets, red indicates the vessels that are evaluated in the Rotterdam Framework. Orange: results for the new method; Green: results for the earlier method. Four reference points per vessel are provided in Rotterdam database (Purple spheres): Point S is the start point of the branch, Point E is the end point, Point A and Point B are two reference points in between Point S and Point E.*

2.4.1.2 CTA data

We performed the quantitative validation on the database provided as part of the Rotterdam Coronary Artery Algorithm Evaluation Framework [82] using the HOOI technique. This facilitates standardized evaluations of the centerline extraction methods over common datasets with ground truth and with standard performance measures. So far, the results of 23 methods are evaluated in this framework. The proposed method was applied to all 32 datasets with the mean voxel size of $0.32 \times 0.32 \times 0.4$ mm^3 (including the 8 training and 24 testing data sets with four reference vessels in each dataset), and the results

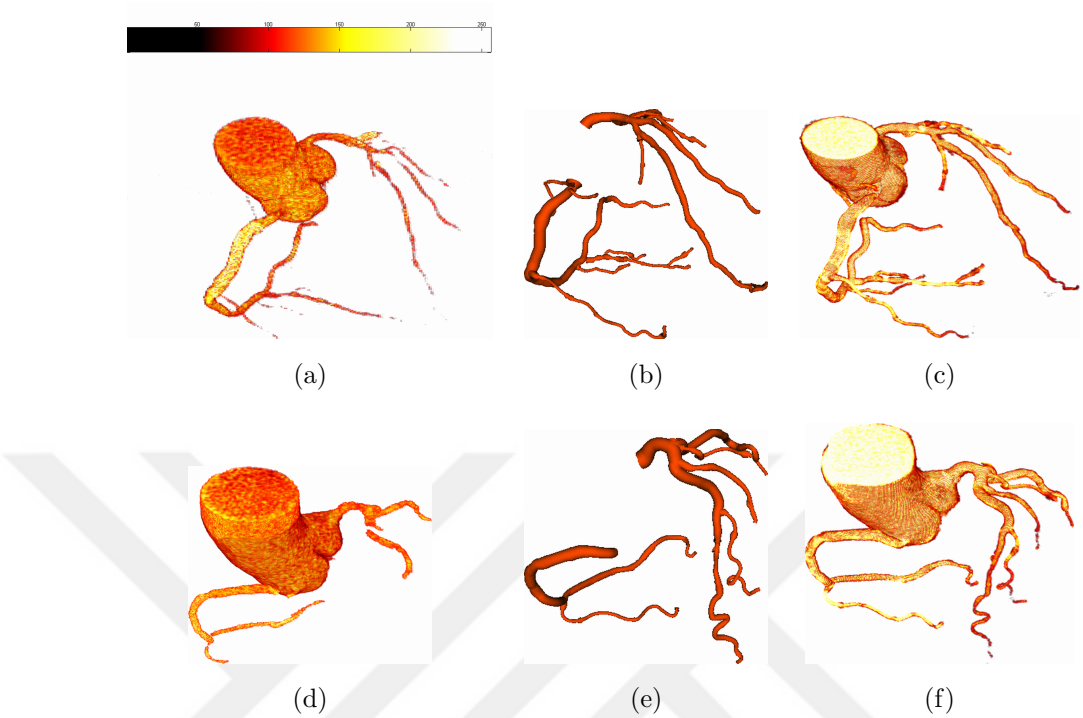


Figure 2.12: *(a,d) Volume rendering of aorta and vessels from datasets 23 and 30; (b,e) all vessels that are detected by the proposed method; (c,f) extracted vessels are shown with aorta as volume rendering.*

were evaluated by organizers. Only training datasets include reference centerline points and corresponding radii. For testing datasets, they only provide four reference points per vessel to segment the target vessel branch.

Table 2.1 summarizes our results[3]. We ranked the first in the semi-automatic algorithms Category #2, in general, our overall average ranking is $10.19th$. In fact our algorithm is nearly automatic: we selected only a single seed for each tree. The two automatic algorithms just above ours have the rankings 10.09 and 10.13, very close to the proposed method.

The results of our previous vessel tractography method, based on a second order tensor model [7], are shown in Table 2.2. The improvements in the scores of the proposed method

[3]Our results of the method HOT tractography among all participating methods can be viewed at: `http://coronary.bigr.nl/centerlines/results/results.php`, last visited: 9 July 2016

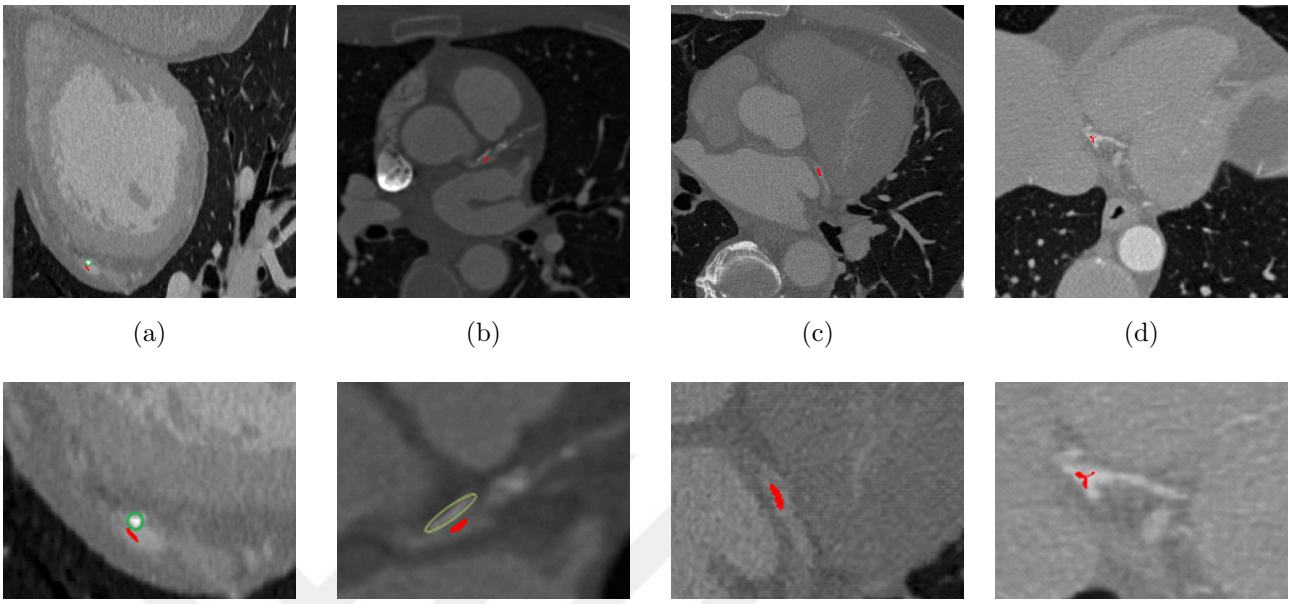


Figure 2.13: *Estimated higher order models are depicted (red) on the slices of CTA dataset of 14, 17, 24, and 29 from Rotterdam database. (a) Sagittal slice cuts the stenotic region (green) on dataset 14; (b) Axial slice cuts the stenotic region (green) on dataset 24; (c) Tensor fitting on dataset 17 at low contrast and noisy intensity regions; (d) Tensor fitting example at branching; (e, f, g, h) Zoomed views of the regions for CTA dataset of 14, 24, 17 and 29 respectively.*

over the previous one can be observed in all measures including overlap and accuracy. In addition, the execution time of the new method is around 10 times faster than the earlier vessel tractography method as can be observed in the overall Rotterdam results table (Footnote 3). Moreover, the new method requires a single seed point per vessel tree, whereas a single seed per vessel was used in the former method. Figure 2.10 depicts the results of the new method on dataset 6 from the Rotterdam training database. It also shows the comparison between our method (orange), previous method (green), and ground truth (purple) on four reference vessels. Figure 2.10 (b) depicts a zoomed view of segment in Figure 2.10 (a) where the two methods, particularly the earlier one deviates from the reference. Figure 2.11 illustrates the segmented arteries using the earlier (green) and the

Table 2.1: *Summary of Rotterdam Results*

Measure	% / mm			score			rank		
	min.	**max.**	**avg.**	**min.**	**max.**	**avg.**	**min.**	**max.**	**avg.**
OV	81.8%	100.0%	97.3%	41.4	100.0	72.9	1	20	5.68
OF	7.1%	100.0%	77.4%	4.9	100.0	63.2	1	22	7.06
OT	83.0%	100.0%	97.7%	44.8	100.0	75.4	1	18	5.30
AI	0.15 mm	0.55 mm	0.34 mm	18.3	59.3	32.0	4	23	14.40
Total							**1**	**23**	**10.20**

Table 2.2: *Rotterdam Results of our previous method [7]*

Measure	% / mm			score			rank		
	min.	**max.**	**avg.**	**min.**	**max.**	**avg.**	**min.**	**max.**	**avg.**
OV	75.5%	100.0%	96.4%	38.8	100.0	64.3	1	16	7.46
OF	6.2%	100.0%	69.9%	3.1	100.0	51.6	1	22	9.11
OT	75.5%	100.0%	97.0%	38.8	100.0	70.3	1	18	6.74
AI	0.23 mm	0.58 mm	0.36 mm	17.9	59.3	30.7	5	22	14.99
Total							**1**	**22**	**11.38**

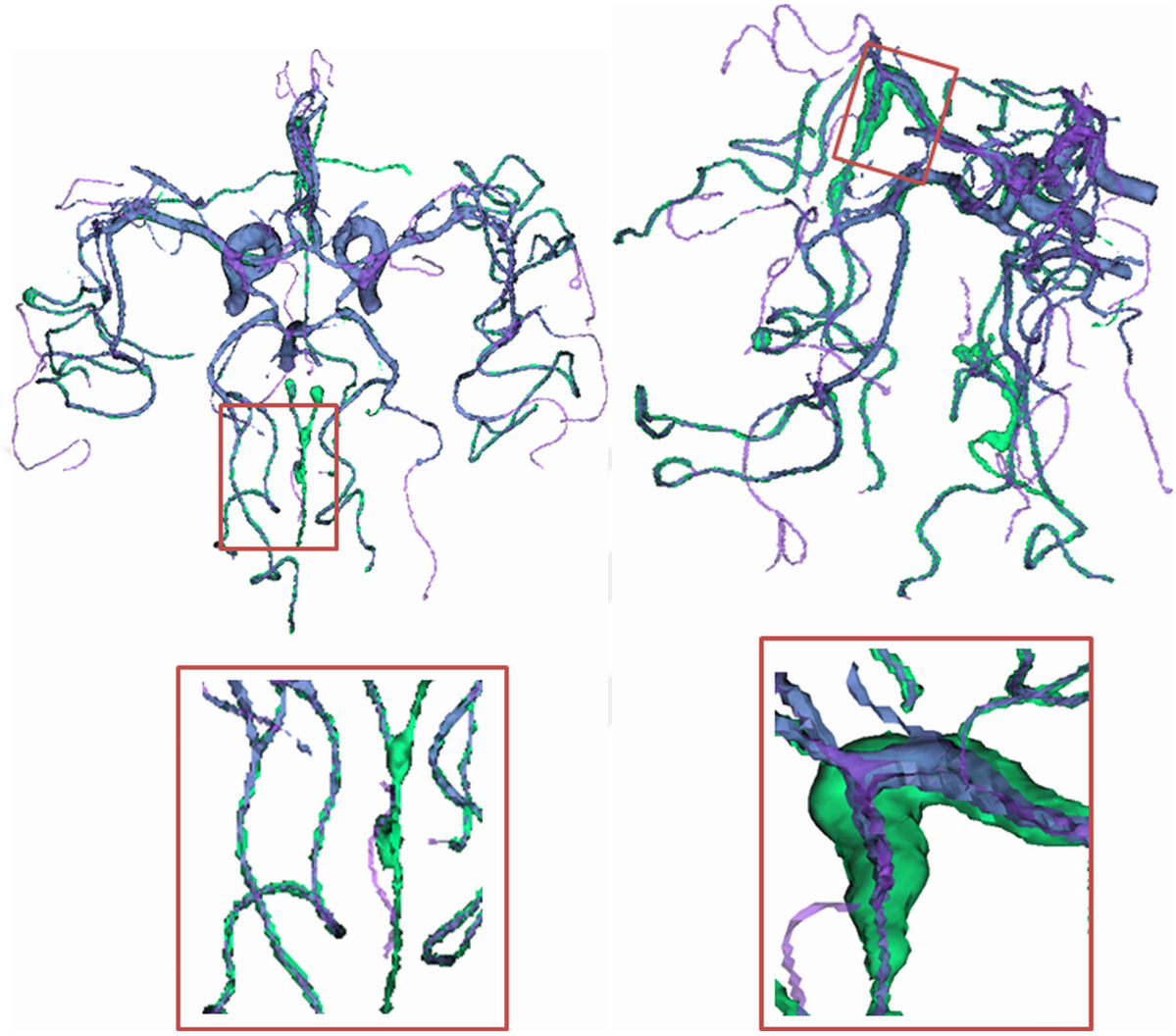


(a) (b) (c)

Figure 2.14: *(a) MIP view of a sample MRA data; (b) Output of the proposed algorithm (red); (c) Output of the algorithm displayed similarly to the manual segmentation (green).*

new (orange) method on three sample datasets from the testing database. The earlier method can be observed to be less smooth (Figure 2.11 (a,c): see the green sections of the branches), and it may also stop propagation earlier than the new method (Figure 2.11 (b): see the orange only sections of the branches where the green surface is missing).

From Table 2.1, it can be observed that the performance of our method is among the top in terms of the overlap measure (average ranking of 5.68), whereas it is not as high



(a) (b)

Figure 2.15: *Comparison of our new method (purple) and previous method (green) on a sample MRA dataset.*

in terms of the accuracy measure (average ranking of 14.40). The latter is a score that is computed based on the distances between the centerlines of the expert versus those of the algorithm. The two closest methods to ours in the Rotterdam Evaluation had very similar accuracy results in the (0.30, 0.34 mm) range, whereas the best and worst methods in terms of accuracy had 0.20 mm and 0.59 mm, respectively. With our average accuracy of 0.34 mm, which is less than a voxel distance away from the centerline, the algorithm

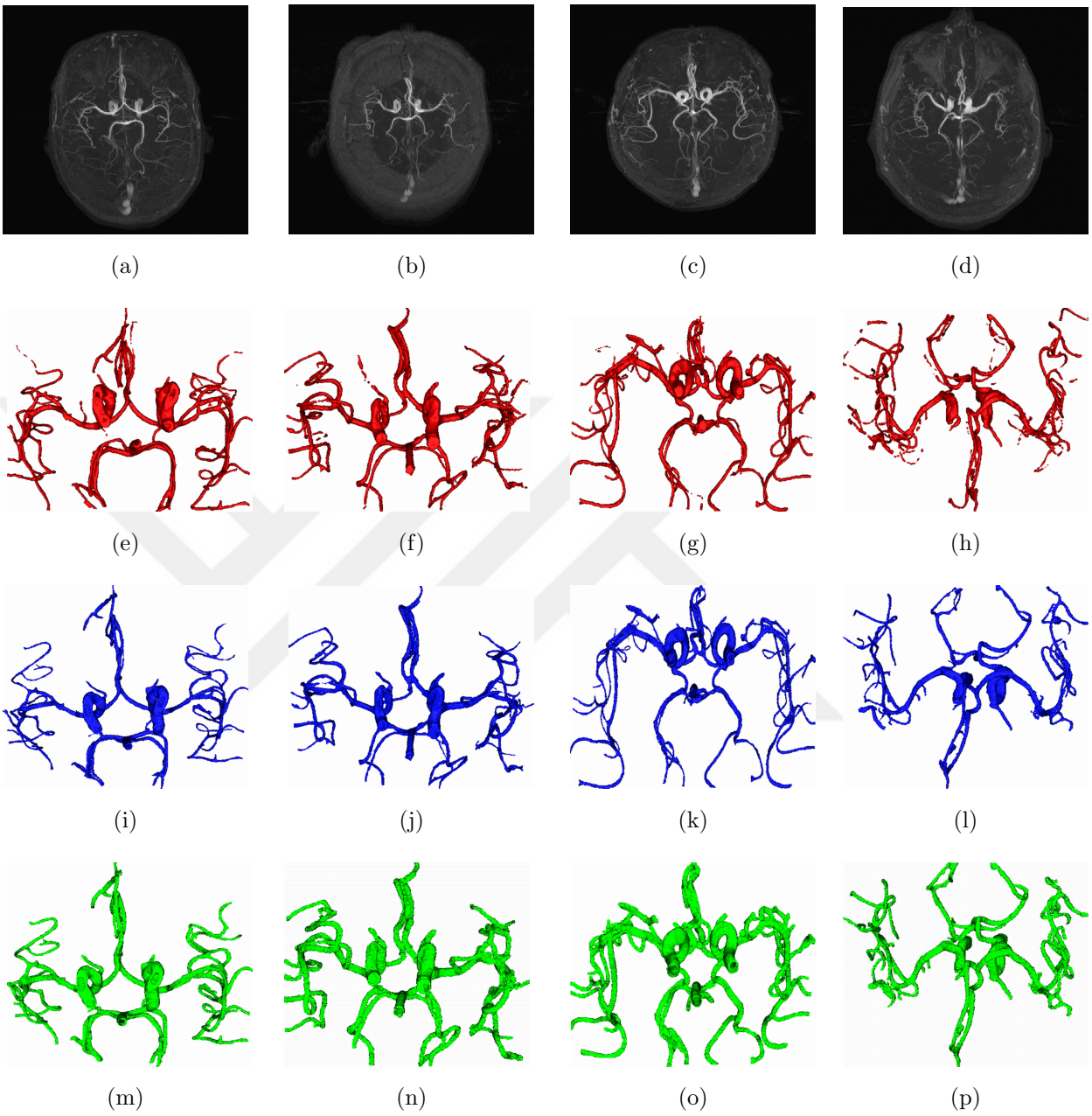


Figure 2.16: *Top row: (a, b, c, d) MIP views of MRA datasets 01, 32, 49, 58; Second row (e, f, g, h): Corresponding manual segmentation results [8]; Third row (i, j, k, l): Our results from the corresponding datasets; Bottom row (m, n, o, p): Results from the corresponding datasets using previous method [7].*

performs in the top half range among all the methods in terms of accuracy scores. On

the other hand, in the OV measure, with 97.3% overlap, we rank the first among semi-automatic (Category #2) and automatic algorithms (Category #1), and the third among all methods, as can be observed in the overall results. Moreover, our algorithm is the fastest among all 24 participating methods (See Footnote 3).

Since Rotterdam Coronary Artery Algorithm Evaluation Framework evaluates only four main vessel branches in each dataset (illustrated in Figure 2.10 and Figure 2.11), it underestimates the actual behavior of our method. In order to show the full performance, two datasets from Rotterdam testing database and corresponding vessel trees with all branches that have been extracted by our method are depicted in Figure 2.12. Volume renderings of aorta and vessels are given together in Figure 2.12 (a,d). Aorta and the whole heart region (delimited by the parietal pericardium) are extracted using the CTA cardiac segmentation software of Kirisli et al. [83]. A threshold is applied to parietal pericardium region to visualize vessels. To eliminate background, a high threshold is selected that have caused few low contrast vessels/branch segments to disappear. As is seen in Figure 2.12 (b,e), the proposed method is capable of segmenting more than four vessel branches in each dataset. Figure 2.12 (c,f) shows our extraction result together with aorta as a volume rendering.

To illustrate the typical behavior of our method in the presence of challenging sections such as with plaque, the estimated higher order tensors are shown for several sample coronary arterial branches over the CTA volumes (testing datasets 14, 17, 24, 29), which have low image quality and severe calcification scores (Figure 2.13). It can be observed that the HOT model works reasonably well over the challenging vessel regions, such as stenotic areas (a, b), low contrast and noisy intensity regions (c), and branchings (d).

2.4.1.3 MRA data

We evaluated the proposed methodology with two decomposition techniques described in section 2.3.3 on a set of 50 image volumes from subjects (25 male, 25 female, age range: 19-66, mean age: 39), which were acquired with time-of-flight (ToF)-MRA on a 3T unit under standardized protocols. Images were reconstructed with $448 \times 448 \times 128$ matrix,

Table 2.3: *Segmentation results of our method on MIDAS MRA volumes*

Avg.±std %	TP (%)	FN (%)	FP (%)	**OM** (%)
HOOI	$94.54 \pm 0.967\%$	$5.46 \pm 0.678\%$	$7.45 \pm 2.98\%$	$92.86 \pm 3.453\%$
RAnk-1 Approx	$95.43 \pm 0.893\%$	$4.57 \pm 0.612\%$	$6.57 \pm 1.93\%$	$94.78 \pm 2.891\%$
Previous Method [7]	$93.07 \pm 1.342\%$	$6.93 \pm 01.410\%$	$9.82 \pm 2.91\%$	$91.74 \pm 3.93\%$

having a voxel size of $0.5 \times 0.5 \times 0.8mm^3$. The images come from the dataset[4] that was used in [84].

In order to quantitatively evaluate the performance of our method, we compared our results with those of the almost-manual segmentation method described in [8] on the same database. Their algorithm flow works as follows: They first manually put seed points on the vessels inside a region of interest. The centerlines of the vessels are then extracted by initializing from the seed points using the method of available opensource TubeTK [61, 85] and VMTK [86] toolkits. Then, the results of centerlines are connected via a fast marching method using image intensity as a speed function which is run until another centerline object is reached. Then, they are backtracked by local gradient direction to obtain the minimal cost path that is used to connect the two centerlines [87]. Finally it is checked to see whether all the centerlines are correctly connected. Then, necessary manual corrections are performed. Later, to extract the vessel radii, they apply an automated lumen segmentation method which is based on geodesic active regions [88].

Table 2.3 tabulates average TP, FN, FP and OM rates with standard deviation on all MRA volumes, for each decomposition technique, as well as our previous method [7]. On average, OM ratios $92.86 \pm 3.453\%$, and $94.78 \pm 2.891\%$ were obtained, respectively for each decomposition method. The OM ratio, $91.74 \pm 3.93\%$, was lower for the earlier method. Furthermore, our previous method took four times longer than the new method with the rank-1 approximation decomposition on the brain vasculature data, and required

[4] `http://insight-journal.org/midas/community/view/21`

2-3 seed points per MRA volume, whereas the new method required only 1 seed point.

Manual segmentation results include only major vessels in the CoW region. For the validation studies, we show the vessels that have larger or equal radius to the provided manual segmentations (between $0.60mm$ and $5.00mm$) for a consistent quantitative and visual evaluation. Figure 2.14 (a) illustrates the MIP visualization of a sample MRA dataset and (b) visualizes the result of the proposed method (red). We display the vessels in green that are comparable to the manual segmentation results, which we use as a ground truth (Figure 2.14 (c)). In Figure 2.15, from different viewpoints, the proposed method output (purple) is visualized on top of the earlier method output (green) [7]. The newly proposed method is capable of finding more number of branches than the early method as can be observed in the purple only branches in the renderings. Furthermore, the previous method showed leakage problems in the depicted regions (see scaled up views in red boxes). Figure 2.16 depicts four sample results (subjects 01, 32, 49 and 58) from MIDAS MRA database. Top row represents MIP images for the sample volumes. Second row illustrates the results of the method in [8] with surface representation (red), third row depicts our results using rank-1 decomposition method (Section 2.3.3.2) (blue) and bottom row illustrates the results of our previous method [7] (green). The smoothness and continuity of the vessel surfaces obtained by the proposed method can be observed when compared to the provided manual segmentation maps and the earlier method.

2.4.2 Sensitivity to Initial Seed Position

In order to seek the sensitivity of our method to the user defined seed, we selected 10 seed points along high contrast regions from one of the MRA image volumes (data #58 of Section 2.4.1.3). Figure 2.17 depicts the 10 seeds used from various cerebral arterial branches. Running our algorithm individually using those 10 seed points, we evaluated the resulting segmentation performance with respect to the provided manual segmentation results. The OM ratios we obtained with both tensor decomposition techniques (Section 2.3.3.1, Section 2.3.3.2) are: $93.43 \pm 1.34\%$ and $95.02 \pm 0.89\%$, respectively. The standard deviations are low and the numbers are within the range of the OM measures calculated for the whole MRA dataset (Table 2.3). This is expected as the HOT trac-



Figure 2.17: *Seed selection from different branch points on the* 58^{th} *dataset of MIDAS MRA database, where seeds are shown by red spheres.*

tography is advanced naturally in both directions from a starting centerline point. The property of the insensitivity to the initialization provides an easier user interaction to our method. The user's only constraint in marking a seed point is to pick a relatively high contrast centerline point that is not on a branching region, which is observed over a slice of the given image volume.

2.4.3 Computational Aspects

We implemented the proposed algorithm in MATLAB (MathWorks Inc., Natick, MA, USA) and C (Mex), and ran the experiments on a computer with Intel Processor Xeon X560 @ 2.67 GHz CPU computer of 64 GB memory. Our algorithm takes less than 30

seconds to create the whole vessel tree in the CTA data experiments of the Rotterdam Evaluation Framework (Section 2.4.1.2). For each MRA experiment of cerebral vasculature extraction (Section 2.4.1.3), the whole tree is captured in ∼60 seconds using the HOOI decomposition method. Time is doubled with rank-1 approximation method. Additional speed up is possible with code optimization. The proposed approach has the potential to be used for future real-time clinical applications.

2.5 Discussions

Quantitative performance of our method was demonstrated on synthetic vasculature, coronary arteries of the Rotterdam Coronary Artery Evaluation Framework, and cerebral arteries of the MIDAS-MRA dataset. The improvement in the performance of the vessel tractography approach going from a second order tensor model in our previous method to the new HOT model embedded into 4D was observed in presented applications of the method, which were also indicated by the reported quantitative scores. Furthermore, the HOT vessel tractography is considerably faster than the earlier method ($\sim$ 10 times in the coronary artery dataset and $\sim$ 4 times in the cerebral artery dataset). Moreover, a less number of seed points is required for the new HOT method.

The pathological sections in vessels are one of the main challenges for vascular segmentation algorithms in addition to branchings. Our method performs reasonably well in stenotic regions of coronary arteries, as the main pathologies in the form of plaques with calcifications are included in the CTA volumes of the Rotterdam dataset, some samples of which were shown in Figure 2.13. However, in Rotterdam Coronary Artery Evaluation Framework, we observed that the performance falls at highly calcified sections. We see two factors that lead to this observation: (i) we apply a basic calcification filter as a preprocessing to remove those plaque areas, which are not delineated very precisely. Later our centerline passes through the remaining part of the lumen excluding those stenosis regions; (ii) the manual expert markings of the centerline in an area with plaque are likely to have more uncertainty when compared to healthier parts of the vessel. We also observed some performance fall in low quality images. However, the maximal rank for almost all methods

above ours was 23 (the number of participating teams) as well (only two had maximal rank of 22). This indicates that each method fell to last places for some challenging data samples with possibly high calcifications and image noise. Therefore, our observation of low performance in noisy image scenarios is valid for the participating algorithms. From Tables 2.1 and 2.2, the proposed method clearly has an improved overall ranking with respect to the earlier method. For a statistical comparison, we performed a paired t-test between the overall metric results of the new method and the earlier method. The differences in the results are statistically significant at a significance level of 0.05 (p-values of the measures are as follows: OV $1.5090e-04$, AI $4.1619e-05$, OT 0.0032, OF 0.0012).

For the cerebral vasculature, pathologies such as aneurysms present difficult scenarios in MRA (or other modality) volumes of unhealthy subjects. For the analysis of those volumes, a preprocessing stage is needed in order to detect the vessel segments that include protrusions or malformations. For instance, a blob filter as in [89, 90] could be used as preprocessing for the datasets with aneurysms. Once those blob-like regions are determined, the corresponding change in the tensor model can be detected, and the HOT tractography could be adjusted to handle those blob regions accordingly during tracking. In general, for vasculature segmentation from the data of the diseased populations, whether for coronary arteries or cerebral arteries or others, an initial pathology detection and labelling stage is required for a correct segmentation procedure. Our removal of the calcifications from the CTA coronary artery datasets is exactly for that purpose. This was discussed previously in the context of the accuracy performance of our technique. Certainly, more advanced calcification segmentation procedures can be employed for an improved performance. Similarly, pathology detection should be carried out for cerebral vasculature in the future for a potential application to the diseased brain image volumes.

The minimal radius of a vessel that can be detected by our algorithm is determined by the physical size of 1 voxel in the data matrix. For the MRA and the CTA dataset applications in this work, the minimum vessel radius size corresponds to 0.5mm on average, determined by the resolutions of the given data.

The proposed algorithm is fast and provides an easy user interaction with a single seed selection, which is not sensitive to the initialization. The method works very well on the

continuous vessels, however, it can stop at the locations where the vessel is interrupted. Hence, one limitation of our method is the requirement of a new seed point when there are disconnected branches, which is a disadvantage if a fully automatic method is required. This could be overcome by employing further structural segmentations; for instance, segmenting the heart and locating a seed in the ostium for the entry point of the coronary arteries. Similarly, brain atlases could be employed for finding automatic seeds in the brain for full automatic cerebral vessel segmentation.

2.6 Conclusion

We presented a new method for extracting a whole vessel tree using a HOT vessel tractography idea, which was inspired by HARDI techniques. The main advantage of the proposed method is the seamless modeling of the n-furcations jointly with tubular sections within the same mathematical model. We achieved this by embedding a general cartesian tensor into a 4D space so that the antipodal asymmetries in Y-junction-like situations could be modeled. Although in this study, we showed the results with a fourth order tensor, a third order tensor in 4D is equally able to model a vessel tree. We validated the HOT vessel tractography method on two different applications: segmentation of coronary arteries and cerebral arteries over real patient image datasets. Both quantitative and qualitative results showed that the proposed method performed well with high overlap ratios in the cerebral MRA application and the coronary CTA application. It ranked among top ten of the all participating methods and ranked the first among the semi-automatic algorithms of the Rotterdam CTA Challenge. These experiments demonstrated the favourable performance of the method on clinical datasets.

Besides, the proposed method shows fast execution time and simple user interaction, which indicate its potential for use in the clinical settings. The proposed HOT vessel tractography method can also be easily adapted to other modalities.

Chapter 3

Asymmetric orientation distribution functions (AODFs) revealing intravoxel geometry in diffusion MRI:[5]

We propose a method that relies on well-established symmetric ODF profiles where the reconstruction of the profiles is performed by following any of the classical HARDI techniques. Here, we utilized diffusion orientation transform (DOT) [12] and spherical deconvolution [91, 13] using HARDI tools [92]. After the estimation of a multi-directional representation of the local fiber orientations, we develop a method that exploits voxel-based ODFs in a conic spatial neighborhood to capture underlying asymmetry of the fiber populations in a voxel.

3.1 Literature Review

The diffusional attenuation of MR signal has been exploited to characterize tissue anisotropy through an indirect computation of the diffusion behavior of water molecules

[5]The preliminary work of this chapter is reported in: *Medical Image Computing and Computer-Assisted Intervention (MICCAI) 2015 Lecture Notes in Computer Science Volume 9349 pp 231-238.*

in human nervous system. In particular, taking several diffusion-weighted images in varying directions enables determination of the orientation of coherently organized nerve fiber tracts. Under the assumption of a single coherent tract per voxel, the diffusion tensor imaging (DTI) has been proven to infer the dominant fiber direction sufficiently [25]. Unfortunately, in cases of heterogeneous fiber structures such as crossing, kissing, fanning or bending fiber configurations, the unimodal orientation distribution function (ODF) assumed by DTI is no longer capable of resolving the orientation of distinct fiber populations within a voxel.

In order to resolve the orientation of distinct fiber tracts in such voxels, diffusion spectrum imaging (DSI) has been suggested [93]. DSI reconstructs the probability density function of particle diffusion displacements over a 3D volumetric grid. However, to date, long acquisition times have prevented clinical applications of this method. Alternatively, high angular resolution diffusion imaging (HARDI) acquisitions, which evenly sample a single or multiple spherical shells, have been proposed [26]. Several methods, using ODFs, which are more flexible representations to indicate multimodal fiber distributions, have managed to overcome DTI's limitations in HARDI data [9, 91, 94, 12]. Tuch et al. [9] suggested a model independent approach that simply forms a linear matrix formulation, known as the q-ball reconstruction based on a spherical radial basis function interpolation. Tournier et al. [91] presented a model-dependent approach that includes the number of distinct fiber orientations in the model. When it is allowed to tend to infinity, this naturally extends to the concept of spherical deconvolution. Ozarslan et al. [94, 11] introduced Cartesian higher order tensors (HOTs) for modeling the apparent diffusion propagator (ADC) and an analytical method for transforming the diffusivity (ADC) profile to probability profiles, also known as the Ensemble Average Propagator (EAP) in the respective time period.

The MR signal is predicted to be complex valued due to the Fourier transform relationship between the displacement distribution and the signal. Consequently, some techniques [95, 96, 97] have been formulated with the capability of handling complex-valued data to yield asymmetric profiles. However, obtaining accurate phase information in diffusion-weighted acquisitions is a formidable task particularly in *in vivo* acquisitions. Most im-

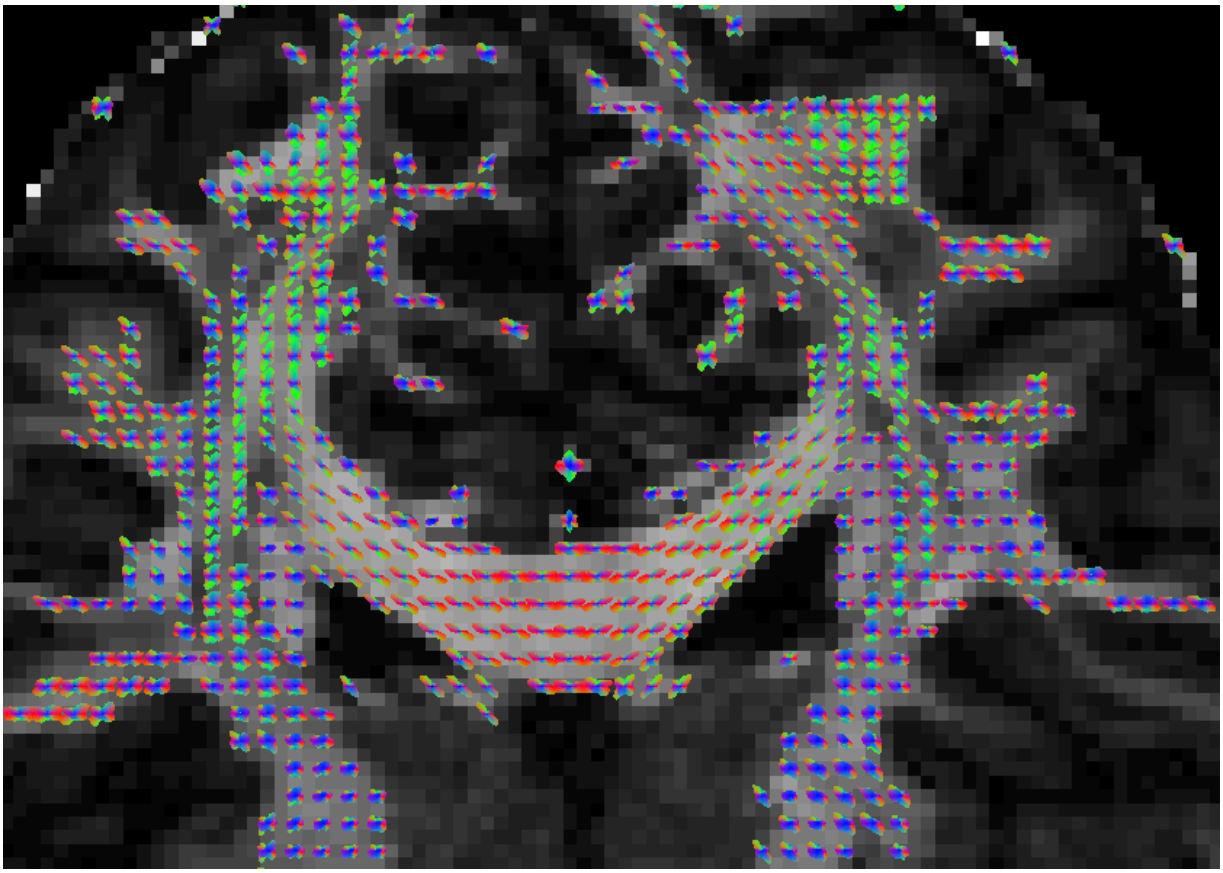


Figure 3.1: *ODF field that is reconstructed by QBall imaging [9] on a sample HARDI data.*

portant obstacle is the patient motion, which substantially distorts the phase of the signal [98]. Additionally, imperfections in the acquisition (e.g., imperfect B_0 shift compensation), flow, and susceptibility variations within the tissue could all influence the detected signal phase substantially. Thus, attributing the observed phase shifts to diffusion alone would be very problematic. Therefore, current diffusion MRI processing pipelines assume magnitude-valued data. When magnitude-valued data are used, the regions containing Y-shaped crossings or bending fibers might lead to unimodal or star-shaped ODF, even though the expected distribution of displacements for water molecules for Y-shaped crossings [95], or curving fibers [11] is asymmetric. Furthermore, the displacement probability profiles obtained from all the above HARDI techniques are always anti-podally symmetric. For instance, the ODF field that is visualized in Figure 3.1, consists of symmetric ODF components over a WM region, whose bending is grossly apparent, as well as regions with potentially asymmetric junctions. Indeed, a recent study [99] showed that the proportion

of WM voxels containing crossing fibers to be between 63% and 90% of the whole WM, whereas the ODFs can model either single fiber populations or only symmetrically crossing fibers.

Several works have been published with varying levels of relevance to our study. In order to model the sprouting or anti-symmetric crossing structures, Barmpoutis et al. [66] suggested an ODF field construction method by considering inter-voxel information, which creates a field of asymmetric spherical functions that differentiate between crossing and splaying fibers. Schultz [70] demonstrated that HOTs indicating likely fiber directions can be estimated from a small number of diffusion-weighted measurements by taking into account information from local neighborhoods. Suggesting an HOT voting method, they demonstrated that the resulting even-order tensor fields facilitate fiber reconstruction at crossings both in synthetic and in real DW-MRI data, and that the odd-order fields differentiate crossings from junctions. In Campbell et al [100], the challenge of partial volume averaging of fiber directions in diffusion MRI data due to multiple fiber orientations within a voxel is noted for tracts with high curvature, crossing, branching, bottlenecks and splaying or sprouting. To overcome the challenge, the data is regularized by considering all pairwise neighbouring voxel ODFs in a local neighbourhood weighted with an index of co-helicity. However, there is no mention of the asymmetrical configurations of fibers in this work.

Pizzolato et al. [101] propose to recover the EAP directly from the complex diffusion weighted signal in order to also describe eventual diffusional asymmetry, thus obtaining an asymmetric EAP. They validate these results in-silico through 3D Monte-Carlo simulations of WM tissue, however, they have not shown any results on real data.

In a recent work by Ehricke et al [102], a regularization on the ODF field is carried out using a cone model like we propose in this study. Although this work sounds similar to ours in that it is using a cone model to filter ODFs, their asymmetric ODF regularization is based on the asymmetric weights assigned to the utilized pair of antipodally-symmetric cones placed at a given voxel during filtering. Neither in the results nor in the discussions is an asymmetric ODF at a voxel level is constructed or depicted, and a voxel-level asymmetric ODF reconstruction was not foreseen, which is exactly the purpose of the method

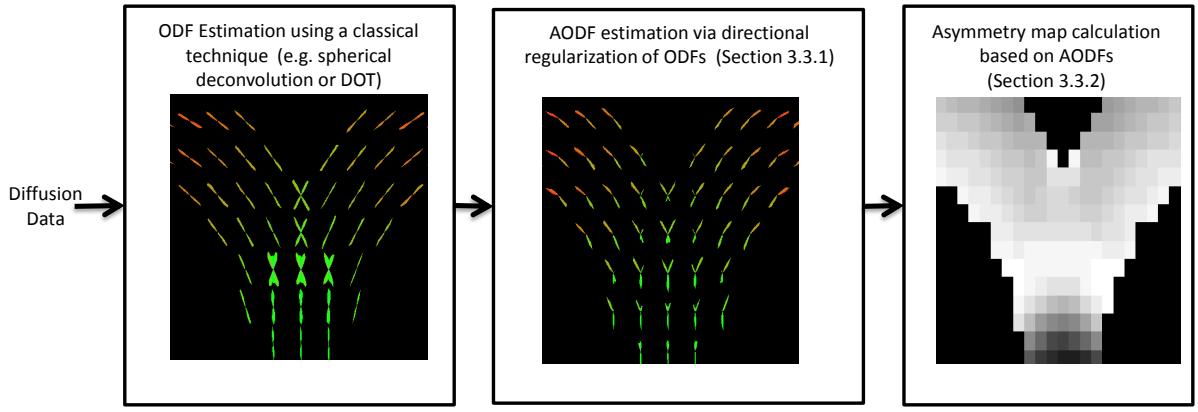


Figure 3.2: *Flowchart of the proposed AODF reconstruction method.*

presented in this work.

In this work, we present a technique for voxel-by-voxel reconstruction of AODFs, which is described in Section 3.3.1. The level of asymmetry is quantified via a new scalar measure, and it is presented in Section 3.3.2. Experimental results using both synthetic and real diffusion MRI data are presented to demonstrate the performance of the proposed algorithm in Section 3.4, followed by discussions in Section 3.5 respectively.

3.2 Mathematical Background

The spherical harmonics (SH) transform is a natural way to decompose signals that live on the sphere (also known as spherical functions). It is also the equivalent of the Fourier transform in the plane, and it is a powerful tool to represent spherical functions.

Due to the modeling of only the magnitude part of the diffusion MRI signal by DMRI pipelines, the signal S becomes real and symmetric. Hence, it is natural to define a real and symmetric orthonormal spherical harmonics basis with even orders [103]:

$$Y_l^m(\theta,\phi) = \sqrt{\frac{2l+1}{4\pi}\frac{(l-m)!}{(l+m)!}}P_l^m(cos\theta)e^{im\phi}, \tag{3.1}$$

where l denotes the order and m is the phase factor. (θ,ϕ) are $(\theta \in [0,\pi], \phi \in [0,2\pi])$ respectively. P_l^m is an associated Legendre polynomial. For $k = 0,2,4,\cdots$, and $m = -k,\cdots,0,\cdots,k$, the new index is defined as $j := j(k,m) = (k^2+k+2)/2+m$ and Y_j is

defined as following:

$$Y_j = \begin{cases} \sqrt{2} \cdot Re(Y_k^m) & if \ -k \leq m < 0 \\ Y_k^0 & if \ m = 0 \\ \sqrt{2} \cdot Img(Y_k^m) & if \ 0 < m \leq k \end{cases} \tag{3.2}$$

where $Re(Y_l^m)$ and $Img(Y_l^m)$ represent the real and imaginary parts of SH respectively.

The HARDI signal is then approximated by

$$S(\theta_i, \phi_i) = \sum_{j=1}^{R} c_j Y_j(\theta_i, \phi_i), \tag{3.3}$$

where $R = (l+1)(l+2)/2$ is the number of coefficients in the modified SH basis of order l. Figure 3.3 depicts the first 15 coefficients of the modified symmetric spherical harmonics basis, which are used to represent DMRI spherical functions on the sphere. Any spherical function can be decomposed as a sum of SH coefficients [10], an example of which can be seen in the bottom row of Figure 3.3.

3.3 Method

We propose a method that relies on well-established symmetric ODF profiles where the reconstruction of the profiles is performed by following any of the classical HARDI techniques. Here, we utilized diffusion orientation transform (DOT) [12] and spherical deconvolution [91, 13] using HARDI tools [92]. After the estimation of a multi-directional representation of the local fiber orientations (ODFs), we develop a method that exploits voxel-based ODFs in a conic spatial neighborhood to capture underlying asymmetry of the fiber populations in a voxel. The proposed method is depicted in a flowchart in Figure 3.2.

The ODF is defined at each voxel location $\boldsymbol{x} = (x, y, z) \in \mathbb{R}^3$ by $\phi(\boldsymbol{x}, \hat{\boldsymbol{u}})$ for the direction vector $\hat{\boldsymbol{u}} \in \mathbb{S}^2$. At the given voxel $\boldsymbol{x}$ and the given direction $\hat{\boldsymbol{u}}$, a cone $\mathbf{C}_{\boldsymbol{x},\hat{\boldsymbol{u}}}$ (Figure 3.4(a)) is constructed by a certain radius r and height h. Although the directional asymmetry of the fiber pathway cannot be deduced from the ODF of a single voxel, it becomes apparent by exploiting the neighborhood diffusion profiles holistically, and considering the ODFs at all voxels in the local volume delimited by the cone $\mathbf{C}_{\boldsymbol{x},\hat{\boldsymbol{u}}}$.

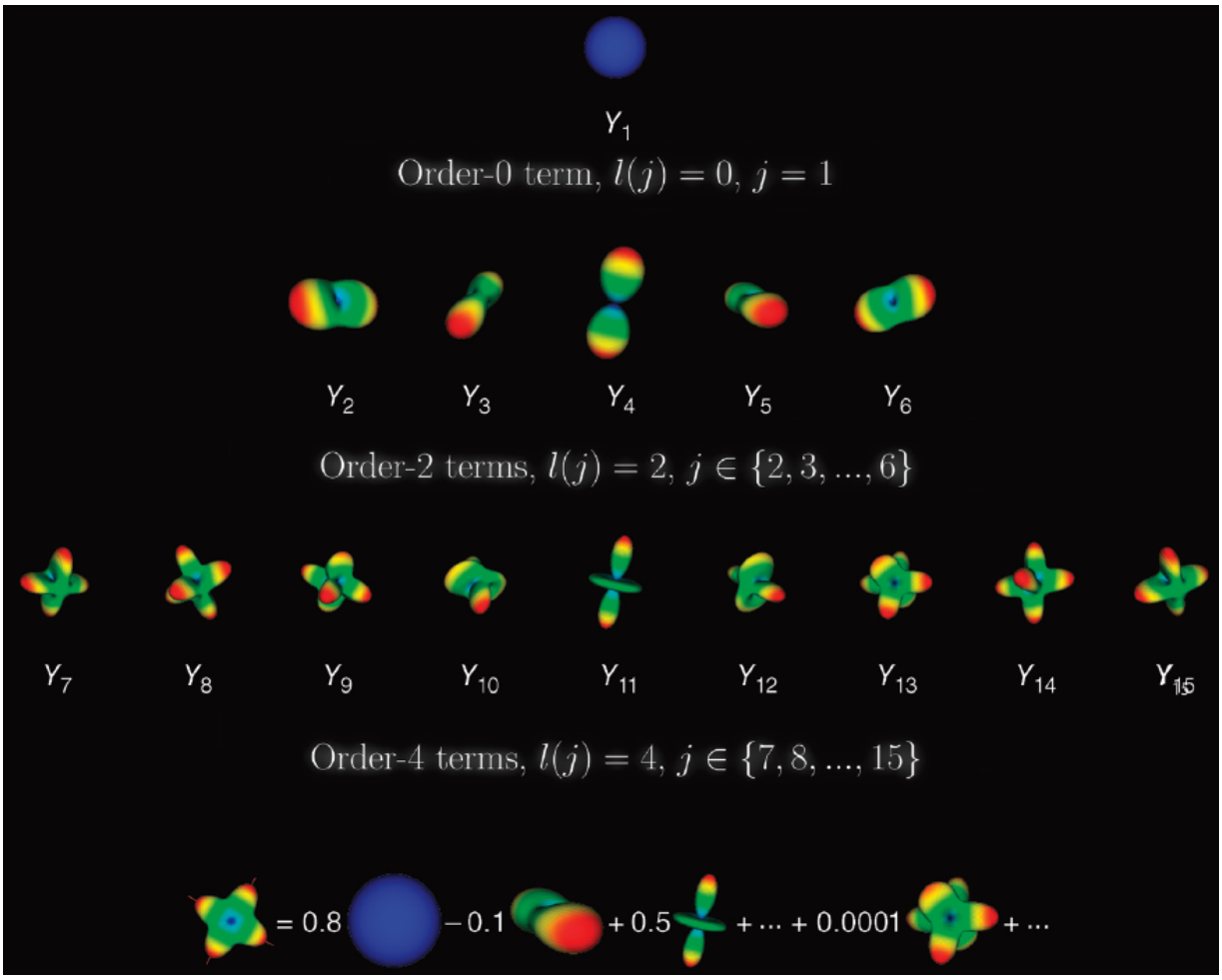
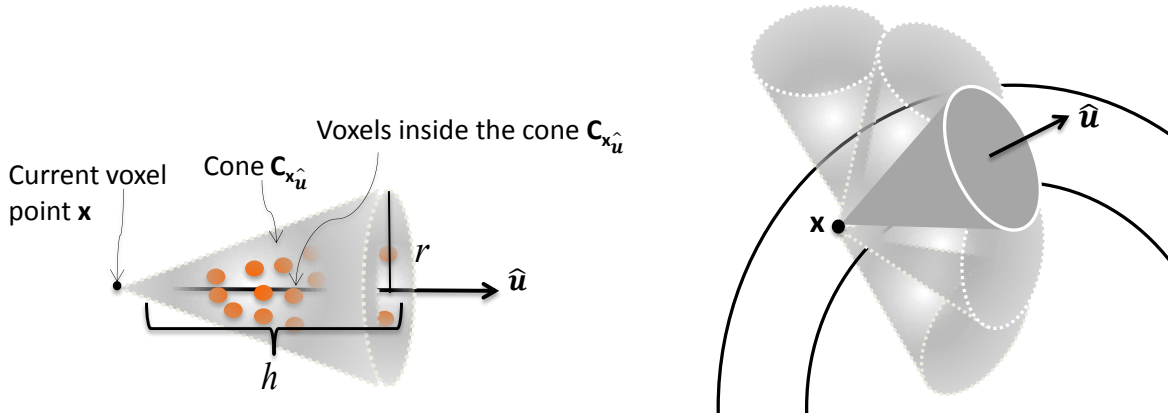


Figure 3.3: *Spherical harmonics basis. First 15 coefficients of the modified symmetric spherical harmonics bases are illustrated, which are used to represent DMRI spherical functions on the sphere. The bottom row shows that any spherical function can be represented as a sum of SH coefficients [10].*

3.3.1 Asymmetric ODFs revealed by a cone model

In this section, the directional regularization of ODF fields using the cone model described above, is presented through three different filtering approaches: (i) a Gaussian filter; (ii) a bilateral filter; (iii) a steerable filter.



(a) (b)

Figure 3.4: *(a) The cone* $\mathbf{C}_{\boldsymbol{x},\hat{\boldsymbol{u}}}$ *is constructed with a certain height and a radius; (b) An asymmetric ODF is reconstructed by rotating the cone model along all sampled directions on the unit sphere at each voxel point, and executing a directional regularization on the ODF field in* $\mathbf{C}_{\boldsymbol{x},\hat{\boldsymbol{u}}}$.

3.3.1.1 Gaussian filter

The idea of a cone-based directional ODF filtering is first realized by building a Gaussian function $G_\sigma(\boldsymbol{x}, \hat{\boldsymbol{u}})$ whose center lies on the axis of the cone $\mathbf{C}_{\boldsymbol{x},\hat{\boldsymbol{u}}}$ with a variance parameter σ. At the voxel $\boldsymbol{x}$, once the cones are constructed along each sampling direction $\hat{\boldsymbol{u}}$ as in Figure 3.4(b), the weighted smoothing of the ODF field is carried out. The weights of Gaussian functions go from highest on the central axis to lowest on the side surface of the cone. This filtering operation can be formulated by:

$$f(\boldsymbol{y}, \hat{\boldsymbol{u}}) = \left[\chi(\boldsymbol{y} \in \mathbf{C}_{\boldsymbol{x},\hat{\boldsymbol{u}}})\, \phi(\boldsymbol{y}, \hat{\boldsymbol{u}})\right] * G_\sigma(\boldsymbol{y}, \hat{\boldsymbol{u}}), \tag{3.4}$$

where convolution is performed by integrating over space, $f(\boldsymbol{y}, \hat{\boldsymbol{u}})$ is the regularized AODF field value at voxel $\boldsymbol{y}$ along $\hat{\boldsymbol{u}}$, and $\chi(\cdot)$ is the indicator function, which takes the value of 1 when the condition in its argument is satisfied, and vanishes otherwise. Note that filtering is performed only along the orientation of the cone $\hat{\boldsymbol{u}}$, i.e., the ODF values only in the direction corresponding to that of the cone are smoothed out over the voxels in the cone. This creates a directional regularization effect and constructs an enhanced field of

view that is capable of seeing further along a given direction in a larger neighborhood. Moreover, the integration over the corresponding ODF values leads to sharpening of the gross orientations while the non-essential (e.g., noise induced) or less dominant directions are suppressed. More importantly, this results in extraction of existing local asymmetries in a fiber distribution at the voxel level.

3.3.1.2 Bilateral filter based on a Gaussian distribution

Secondly, we exemplify the directional ODF regularization via a bilateral filter, which has been developed as a non-linear, edge-preserving low pass filter for images [104]. It involves an averaging of intensity values from nearby pixels to set the intensity value at each pixel in an image. We adapt the bilateral filtering to ODF fields as follows: for all voxels in a given cone, the ODF values at the orientation corresponding to the axial direction of the cone are used as the intensity values in an image. The weighted average of those ODF values along the corresponding direction are calculated by:

$$f^b(\boldsymbol{x}\,,\hat{\boldsymbol{u}}\,) = \frac{1}{W_{\boldsymbol{x}}} \sum_{\boldsymbol{y}_{\,i}\in\mathbf{C}_{\boldsymbol{x}\,,\hat{\boldsymbol{u}}}} \phi(\boldsymbol{y}_{\,i},\hat{\boldsymbol{u}}\,)G_{\sigma_s}(\|\boldsymbol{x}\,-\boldsymbol{y}_{\,i}\|)\,G_{\sigma_r}(\|\phi(\boldsymbol{x}\,,\hat{\boldsymbol{u}}\,)-\phi(\boldsymbol{y}_{\,i},\hat{\boldsymbol{u}}\,)\|)\;,$$

where G_{σ_r} is the Gaussian range kernel function for smoothing differences in the ODF values and G_{σ_s} is the Gaussian spatial kernel function for smoothing differences in coordinates. $W_{\boldsymbol{x}}$ is the normalization term:

$$W_{\boldsymbol{x}} = \sum_{\boldsymbol{y}_{\,i}\in\mathbf{C}_{\boldsymbol{x}\,,\hat{\boldsymbol{u}}}} G_{\sigma_s}(\|\boldsymbol{x}\,-\boldsymbol{y}_{\,i}\|)\,G_{\sigma_r}(\|\phi(\boldsymbol{x}\,,\hat{\boldsymbol{u}}\,)-\phi(\boldsymbol{y}_{\,i},\hat{\boldsymbol{u}}\,)\|)\;. \tag{3.5}$$

Thus, $f^b(\boldsymbol{x}\,,\hat{\boldsymbol{u}}\,)$ is the AODF obtained via the directional bilateral filter of ODFs in the neighborhood of $\boldsymbol{x}\,$.

3.3.1.3 Steerable Gaussian filter

The orientation selective excitations in the human visual cortex have been exploited by early image processing techniques such as [105], which presented filters with isotropic and anisotropic components for restoration of noisy images. Anisotropic part of the filters involved a set of detectors at different orientations. Such early works constituted the origins

of the idea of steerable filters in [106], which include an orientation-selective convolution kernel that can be expressed via a linear combination of a small set of rotated versions of itself. Steerable filters are popularly used for image enhancement and feature extraction [107, 108, 109]. We adapt the steerable filtering to ODF regularization by taking the ODF values of the voxels in the given cone as follows:

$$f^s(\boldsymbol{y}\,,\hat{\boldsymbol{u}}\,) = \chi(\boldsymbol{y}\,\in \mathbf{C}_{\boldsymbol{x}\,,\hat{\boldsymbol{u}}}\,)\;\phi(\boldsymbol{y}\,,\hat{\boldsymbol{u}}\,) * h(\boldsymbol{y}\,,\hat{\boldsymbol{u}}\,)\;. \tag{3.6}$$

Here, the convolution of the ODF with the steerable filter $h(\cdot)$ is given by

$$\phi(\boldsymbol{y}\,,\hat{\boldsymbol{u}}\,) * h(\boldsymbol{y}\,,\hat{\boldsymbol{u}}\,) = \sum_{k=1}^{N}\sum_{l=0}^{k}\sum_{m=0}^{k-l} b_{klm}(\hat{\boldsymbol{u}}\,)\;\phi(\boldsymbol{y}\,,\hat{\boldsymbol{u}}\,) * h_{klm}(\boldsymbol{y}\,)\;, \tag{3.7}$$

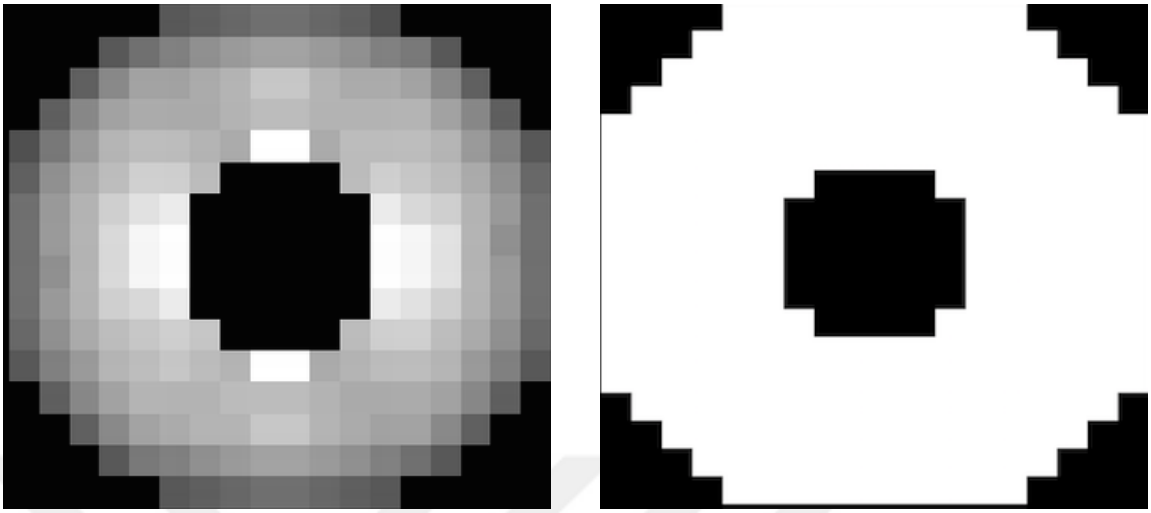
where N is the order of the filter. The functions $b_{klm}(\hat{\boldsymbol{u}}\,)$ are trigonometric functions that interpolate the rotation of the filters $h(\boldsymbol{y}\,,\hat{\boldsymbol{u}}\,)$. This decomposition decouples the rotation of the filters from the convolution in Eq. 3.6, which makes the estimation computationally efficient. The most widely used and well known family of steerable filters are Gaussian derivatives $g(x, y, z)$ and their linear combinations [106, 110] which we also utilized:

$$h_{klm}(x, y, z) = \frac{\partial^l}{\partial x^l}\frac{\partial^m}{\partial y^m}\frac{\partial^{k-l-m}}{\partial z^{k-l-m}} g(x, y, z)\;. \tag{3.8}$$

3.3.2 Measuring Asymmetry

After we construct an AODF field using one of the methods in Section 3.3.1, an asymmetry measure can be computed at each voxel in order to create a scalar map that quantifies asymmetry over WM regions. For this purpose, we propose a measure based on the angular similarity (covariance) metric in [96]. Envisioning functions to be vectors on an ∞-dimensional Hilbert space, the cosine of the angle between the two functions is a measure of their similarity. When symmetry is concerned, the functions can be taken to be the AODF denoted by $f(\hat{\boldsymbol{u}}\,)$, and its reflection about the origin, $f(-\hat{\boldsymbol{u}}\,)$. To this end, it is natural to consider the inner product to define a symmetry-seeking measure as in the following:

$$\cos\gamma = \frac{\int_S f(\hat{\boldsymbol{u}}\,)f(-\hat{\boldsymbol{u}}\,)\mathrm{d}\hat{\boldsymbol{u}}}{\int_S f(\hat{\boldsymbol{u}}\,)^2\mathrm{d}\hat{\boldsymbol{u}}} = \frac{\sum_{l=0}^{l_{\max}}\sum_{m=-l}^{l}(-1)^l\,|a_{lm}|^2}{\sum_{l=0}^{l_{\max}}\sum_{m=-l}^{l}|a_{lm}|^2}\;. \tag{3.9}$$



(a) (b)

Figure 3.5: *(a) Asymmetry index map; (b) FA map calculated for circularly bending fibers:(bright-to-dark:high-to-low values).*

Here, the last expression provides the measure in terms of a_{lm}, which are the coefficients obtained when $f(\hat{\boldsymbol{u}})$ is represented in a series of spherical harmonics. Then an asymmetry measure α can be defined at each voxel:

$$\alpha = \sin\gamma = \sqrt{1 - \cos^2\gamma}. \tag{3.10}$$

This scalar measure can be computed on a voxel-by-voxel basis to create a gray-scale map, which provides contrast dependent on the inherent intra-voxel asymmetry of fiber populations. A sample asymmetry map calculated for a circularly bending fiber configuration (Section 3.4.1.1) is shown in Figure 3.5. In contrast to the most widely used scalar measure for WM fibers, the fractional anisotropy (FA), which is not very informative here other than showing a high level of constant anisotropy, the asymmetry map signifies the changing level of asymmetry at different radii in concentric circular fibers.

3.4 Experiments and Results

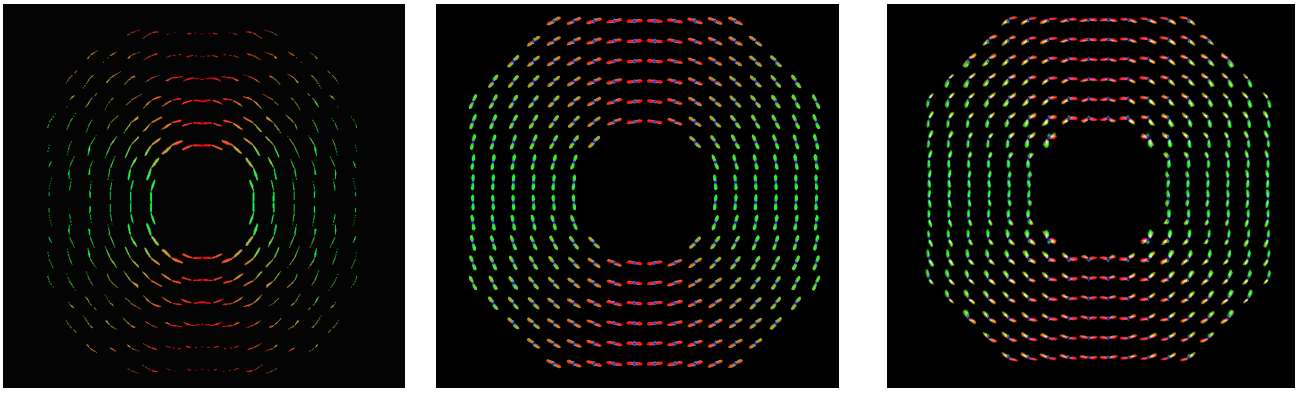
In this section, we will show the results of the cone-based directional ODF regularization and maps of the asymmetry measure on both synthetic and real data. Diffusion MRI

data: Synthetic diffusion MRI data are obtained from INRIA [75, 74]. The volumes are typically of size $30 \times 30 \times 18$ with 81 gradient directions and they are representative of various fiber crossing scenarios including asymmetric junctions (Section 3.4.1.2). A second synthetic data is simulated for a full circular fiber geometry (Section 3.4.1.1). The real diffusion MRI data with both high and low number of gradient directions are obtained from two online databases (Section 3.4.2). The parameters cone height h and radius r (defined in Section 3.3.1) are selected as 2 mm and 5 mm for synthetic and real experiments, respectively. The filter order in steerable filters $N = 5$, and $\sigma = 0.5$ for all experiments, these parameters were selected empirically.

3.4.1 Synthetic Fibers

3.4.1.1 Synthetic Bending Fibers

Diffusion taking place in a curving fiber within a full circle geometry was considered in [11], wherein the physical signal attenuation for each portion of the curving circular fiber is derived. Using this result, we simulate the q-space complex signal for a set of concentric circularly bending fibers, which are reconstructed over a three-dimensional (3D) volumetric grid. A Fourier transform is taken to produce the true EAP. Then, we use the DSI approach [93], where the EAP is integrated radially along given gradient directions to obtain the "true" ODFs, which display the inherent asymmetry in the fiber. One such sample simulated experiment is shown in Figure 3.6. In (a), the reconstructed ODFs for a set of circularly bending fibers using the just described DSI method is shown. In (b) the symmetric ODFs using one of the classical methods, more specifically, the DOT approach [12], are depicted. In (c) the AODFs at each voxel constructed by our method in Section 3.3.1.3 are shown. Clearly, the proposed spatial directional regularisation of the symmetric ODFs resulted in an asymmetric ODF field, which is naturally in line with the underlying curving geometry, as also verified by the"true" ODF field obtained from the DSI method. The bending structures are now visible at the voxel level. The asymmetry is visibly decreasing for larger circles as expected.

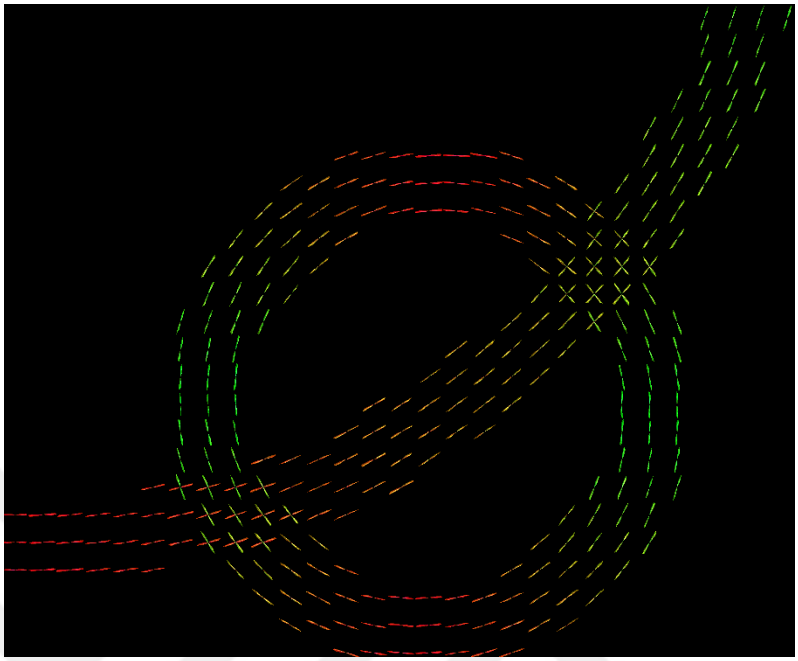


(a) (b) (c)

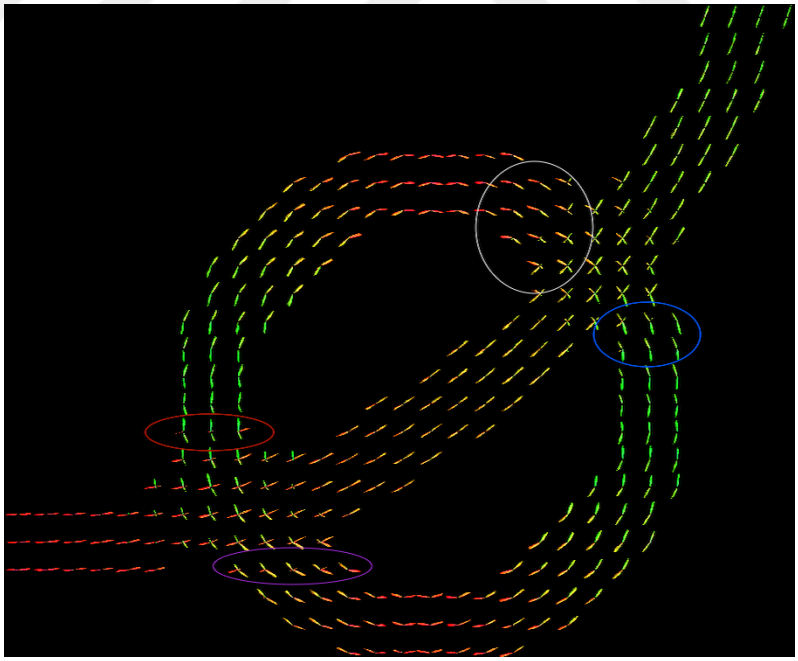
Figure 3.6: *Circularly bending fibers: (a) AODF field created by the analytical results in [11]; (b) ODF field created by the DOT method [12]; (c) AODF field created by the proposed technique.*

3.4.1.2 Synthetic Crossing Fibers

Three more synthetic examples (data taken from the simulations in [111]) demonstrate the capabilities of the proposed technique. In Figure 3.7, a circular pattern of fibers meet a bending line of fibers in non-symmetric junctions. The ODF field shown in Figure 3.7(a) clearly displays the symmetry assumption imposed in conventional HARDI processing as seen from the visualised symmetric ODFs. The AODF field results are visualized for each technique: Gaussian (Figure 3.7(b)), bilateral (Figure 3.7(c)), and steerable (Figure 3.7(d)) filtering. Ellipses with matching colors show the comparison among each technique on the same fiber region of interest.

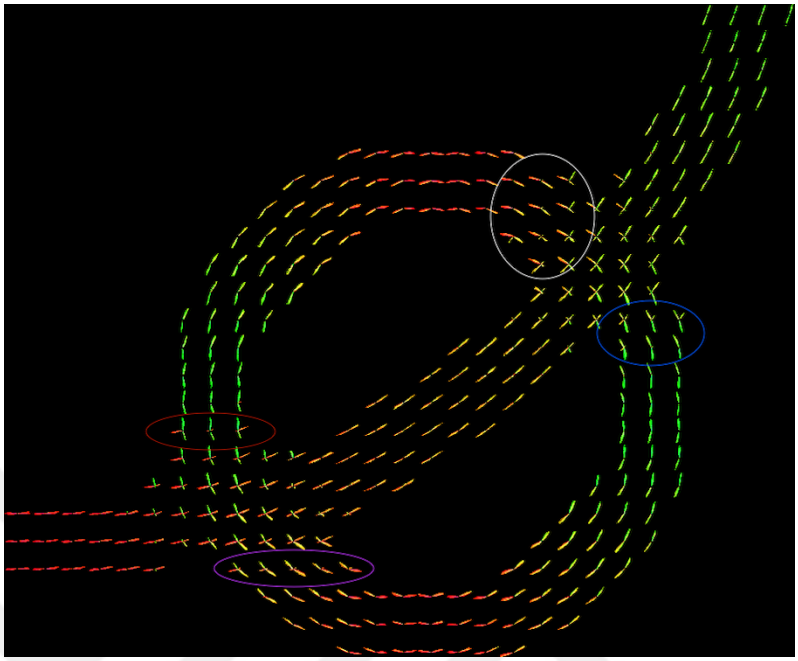


(a)

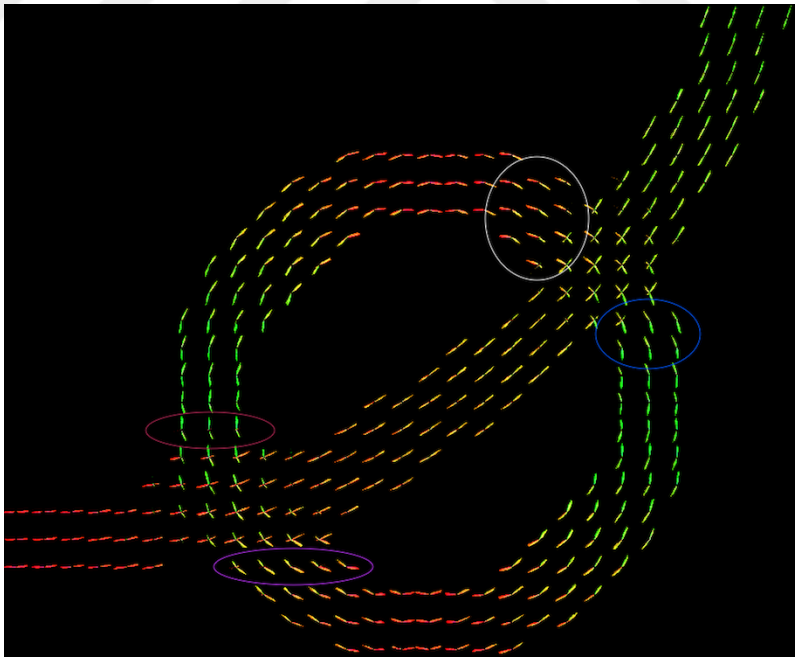


(b)

Figure 3.7: *Simulations for strong curvature fibers. (a): ODFs obtained via the method in Ref. [13]; (b) AODF maps obtained by Gaussian filtering (Figure c and d are in the following page).*

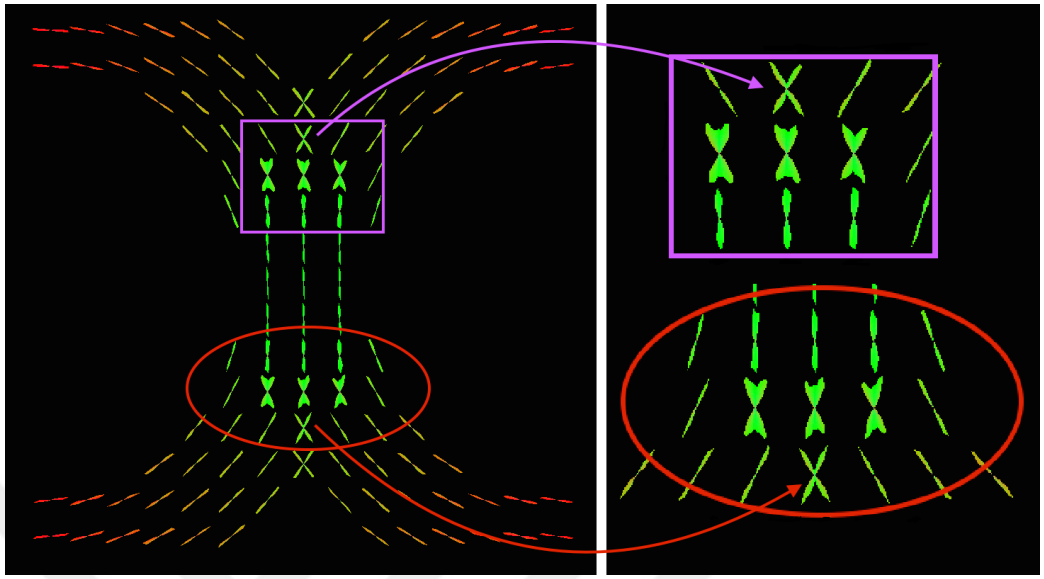


(c)

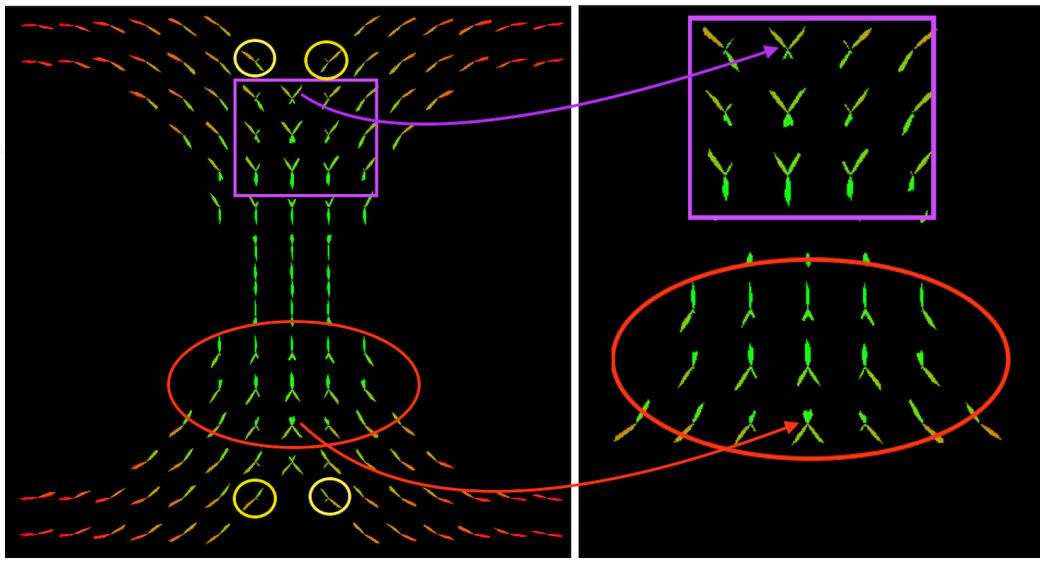


(d)

Figure 3.7: *Simulations for strong curvature fibers. (c) AODF maps obtained by bilateral filtering; (d) AODF maps obtained by steerable filtering.*



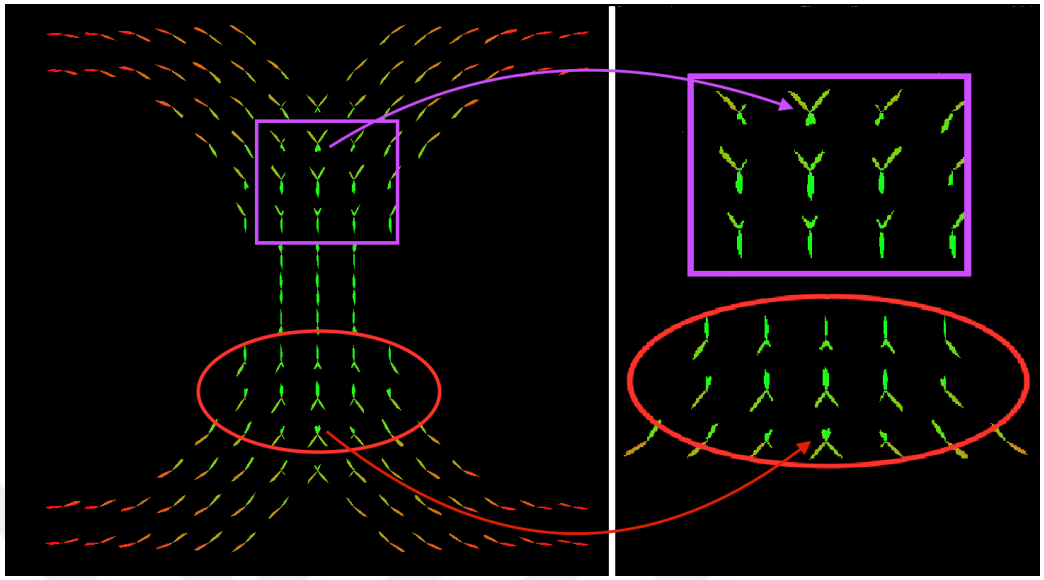
(a)



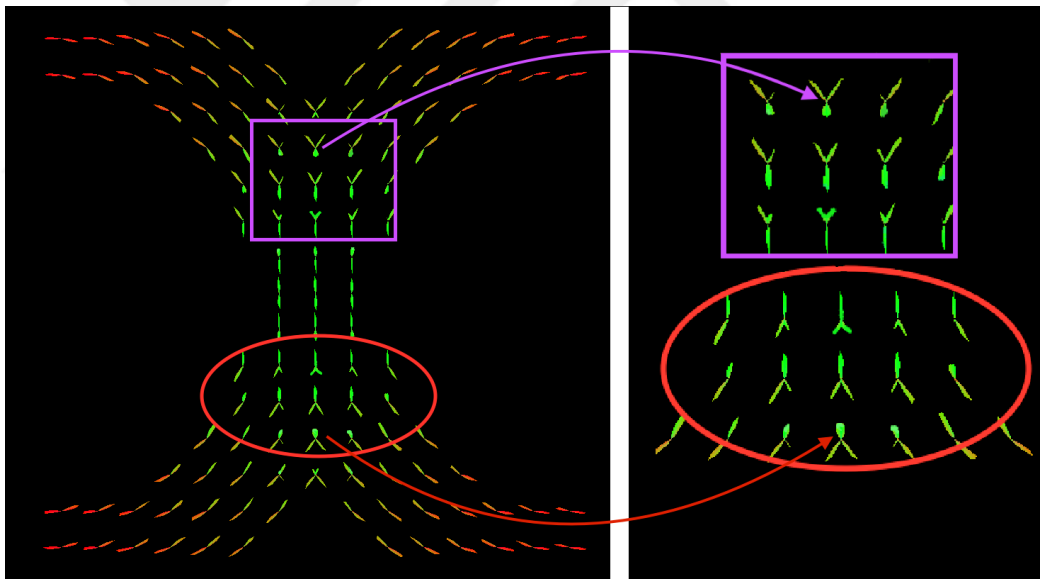
(b)

Figure 3.8: *Simulations for kissing fibers. (a): ODFs obtained via the method in Ref. [13]; (b) AODF maps obtained by Gaussian filtering (Figure c and d are in the following page).*

In Figure 3.8, a bottleneck or a kissing fiber geometry is depicted. Figure 3.8(a) shows the ODF representation of the kissing fibers, whereas Figure 3.8(b) depicts the corresponding reconstructed asymmetric ODFs by Gaussian filtering. Figure 3.8(c, d) shows the reconstructed asymmetric ODFs by bilateral and steerable filtering, respectively.



(c)



(d)

Figure 3.8: *Simulations for kissing fibers. (c) AODF maps obtained by bilateral filtering; (d) AODF maps obtained by steerable filtering.*

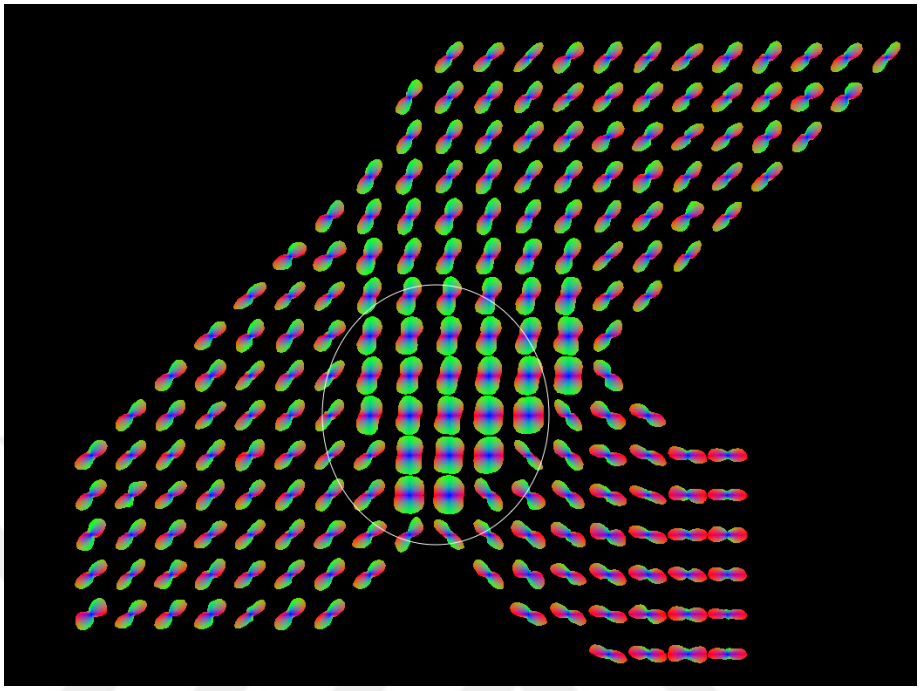
Noisy AODFs are depicted by yellow ellipses. On the right side of the figures, zoomed views of the regions are depicted.

The last synthetic example that represents the branching fibers is shown in Figure 3.9. Figure 3.9(a) depicts the ODF representation of the branching fibers while the corre-

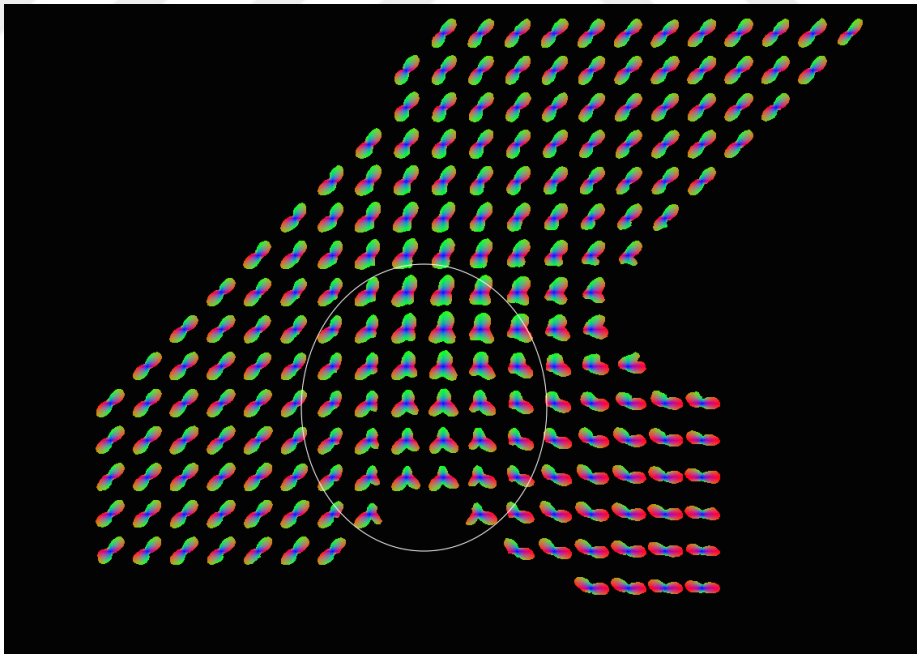
sponding reconstructed asymmetric ODFs by Gaussian filtering is shown in Figure 3.9(b). Figure 3.9(c, d) demonstrates the results of the reconstructed asymmetric ODFs by bilateral and steerable filtering, respectively.

3.4.2 Real MRI Data Fibers

HARDI data are obtained from two datasets: MGH-USC Human Connectome Project (HCP) (https://ida.loni.usc.edu/login.jsp) and Parkinson's Progression Markers Initiative (PPMI) Project database(http://www.ppmi-info.org). HCP data are acquired from 288 gradient directions with $1.25 \times 1.25 \times 1.25$ mm^3 voxel size whereas PPMI data are acquired from 64 gradient directions with $1.98 \times 1.98 \times 2$ mm^3 voxel size. The ODF field for both data are created by the DOT method [12]. As a preprocessing operation, we inserted a sigmoid function on the ODF field to enhance very high components and suppress very low components, which are likely to be due to noise. To focus on fiber pathways that exhibit high curvature, we selected the corpus callosum (CC) and Meyer's Loop (ML) as shown in Figure 2.1. It is well known that non-invasive extraction of the visual pathways including CC and ML through Diffusion MRI is challenging due to the strong bending, crossing and kissing geometric patterns in the relevant anatomy. For the MRI data experiments, AODFs reconstructed by the steerable filter-based ODF regularization are utilized. Figure 2.1 shows the reconstructed AODFs for PPMI HARDI data.

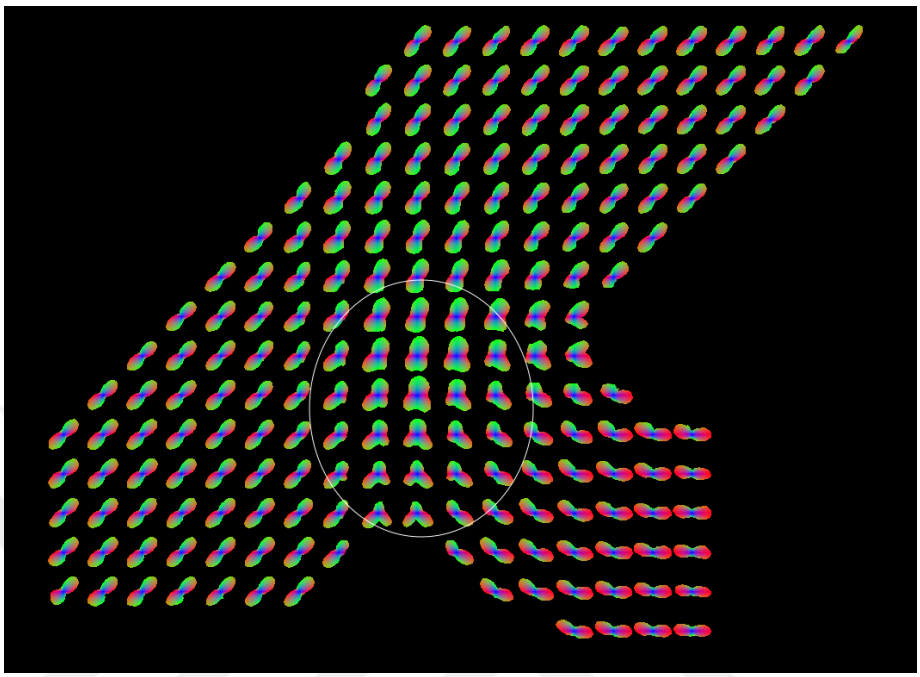


(a)

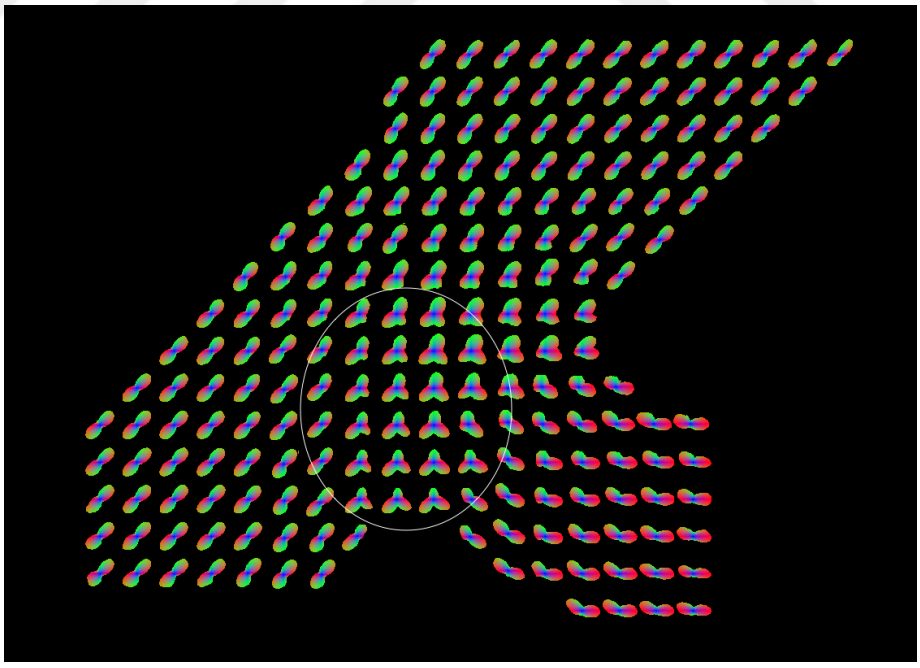


(b)

Figure 3.9: *Simulations for branching fibers. (a): ODFs obtained via the method in Ref. [13]; (b) AODF maps obtained by Gaussian filtering (Figure c and d are in the following page).*



(c)



(d)

Figure 3.9: *Simulations for branching fibers. (c) AODF maps obtained by bilateral filtering; (d) AODF maps obtained by steerable filtering.*

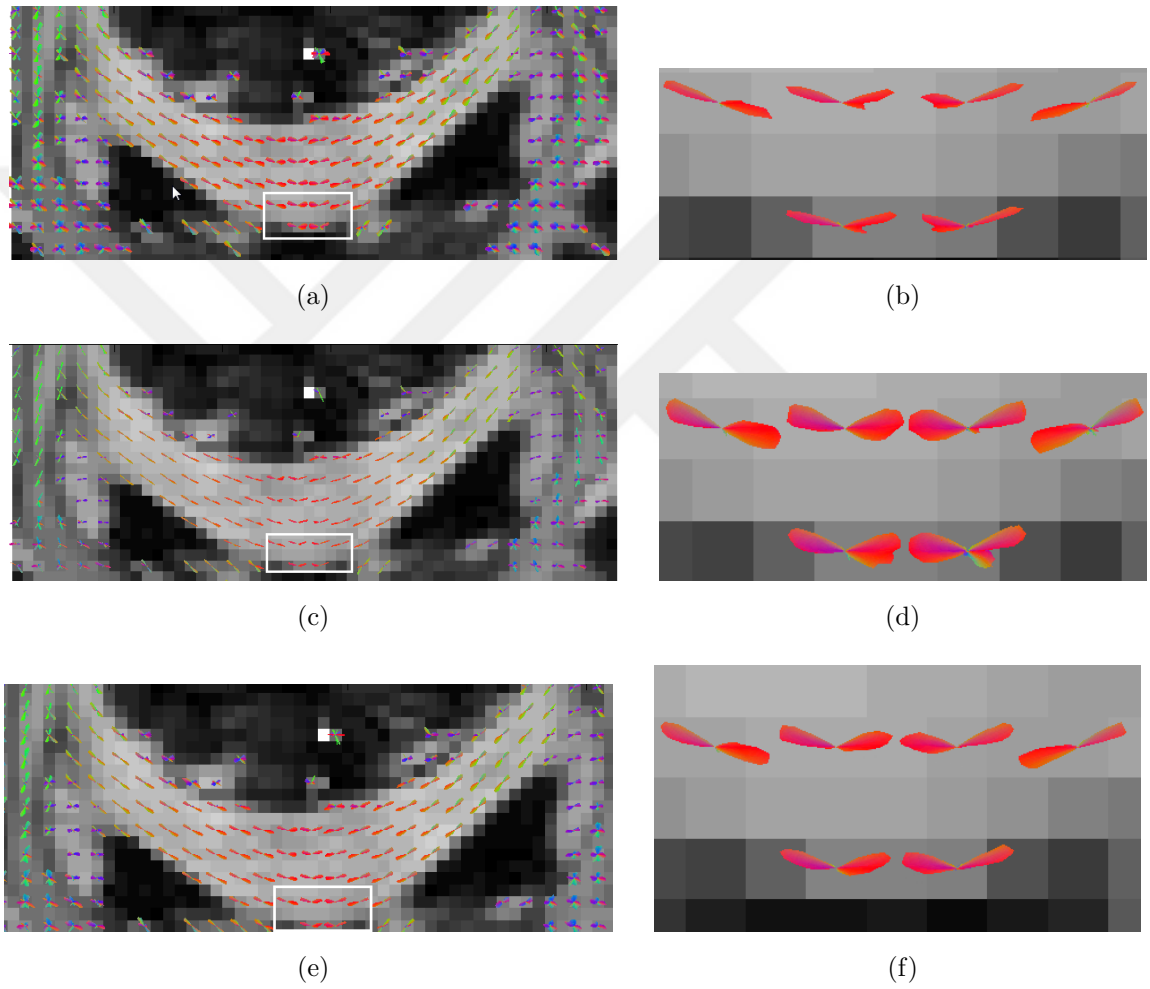


Figure 3.10: *The results of (a) Gaussian filtering; (c) bilateral filtering; (e) steerable filtering on HCP HARDI data; (b, d, f) zoomed views of each filtering techniques.*

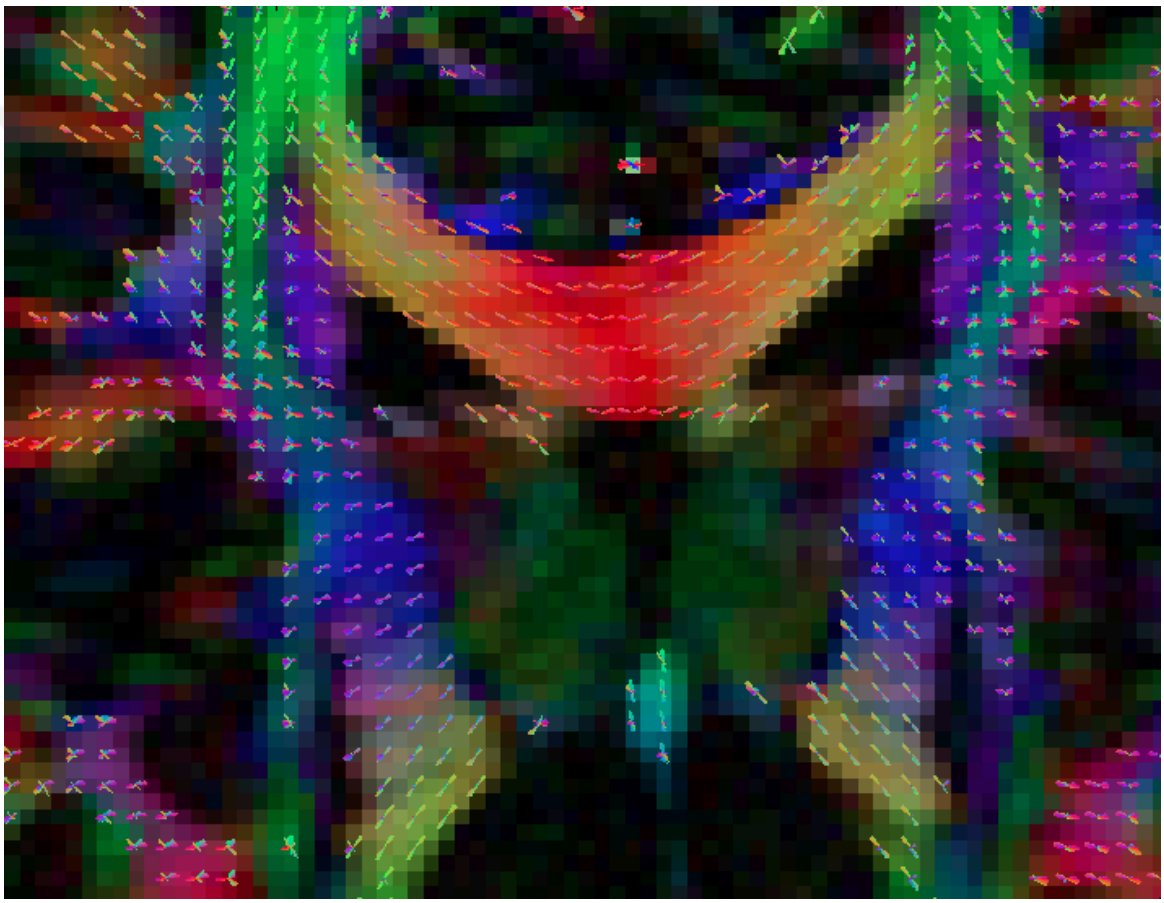


Figure 3.11: *The result of steerable filtering on PPMI HARDI data.*

3.4.3 Asymmetry Index Map Results

Figures 3.12, 3.13, and 3.14 demonstrate the comparison of FA and asymmetry maps that are calculated for each filtering technique over a slice of the following: a circle crossing bending lines of fibers, kissing fibers, branching fibers and real WM fibers.

In Figures 3.15 and 3.16, the asymmetry maps for real data (PPMI and HCP data) over an axial slice are shown.

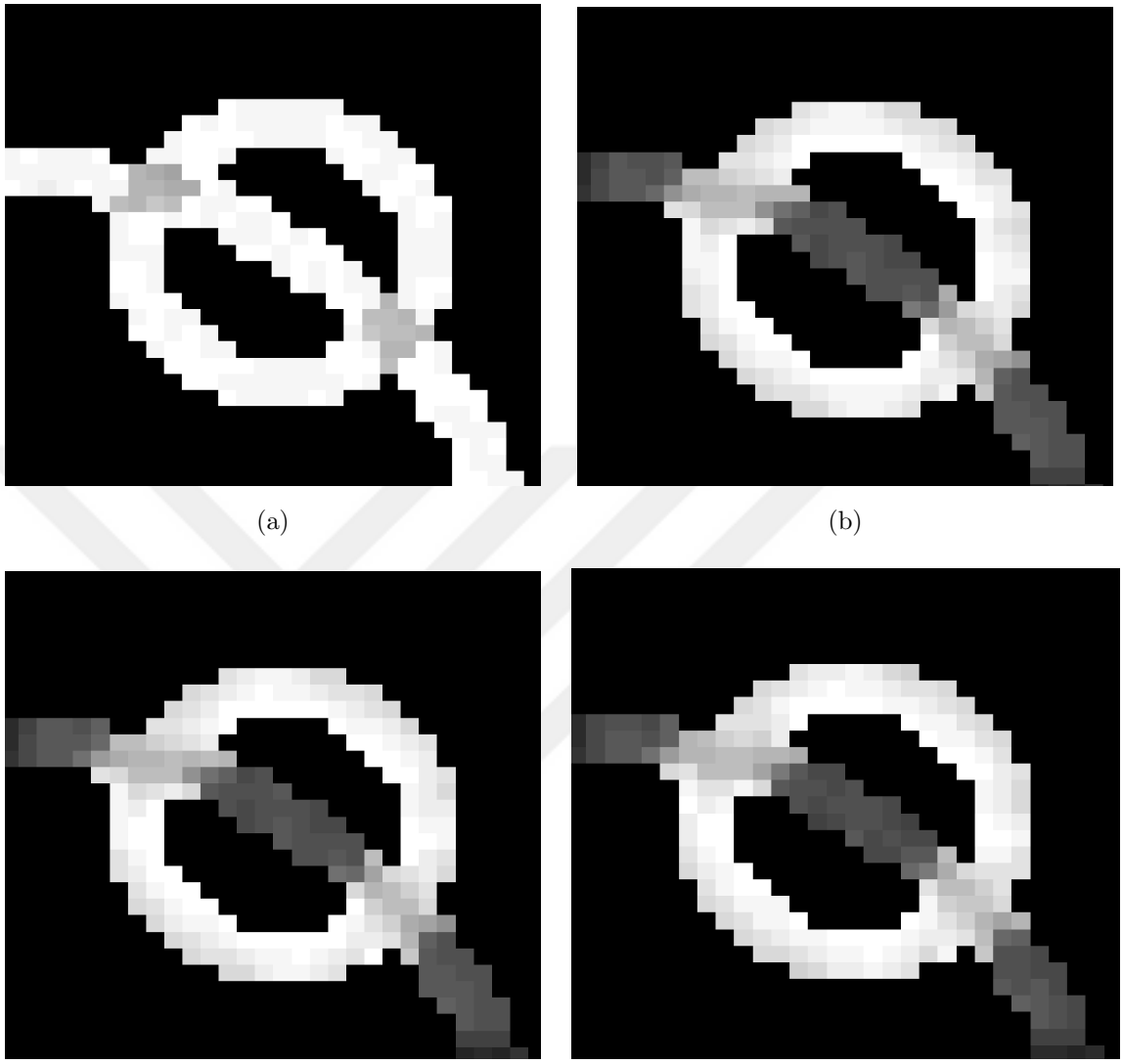


Figure 3.12: *FA (a) and asymmetry (b, c, d) maps (bright-to-dark:high-to-low values) calculated for strong curvature fibers; (b): Filtering with a Gaussian function; (c): Bilateral filter based on a Gaussian distribution; (d): Steerable Gaussian filter.*

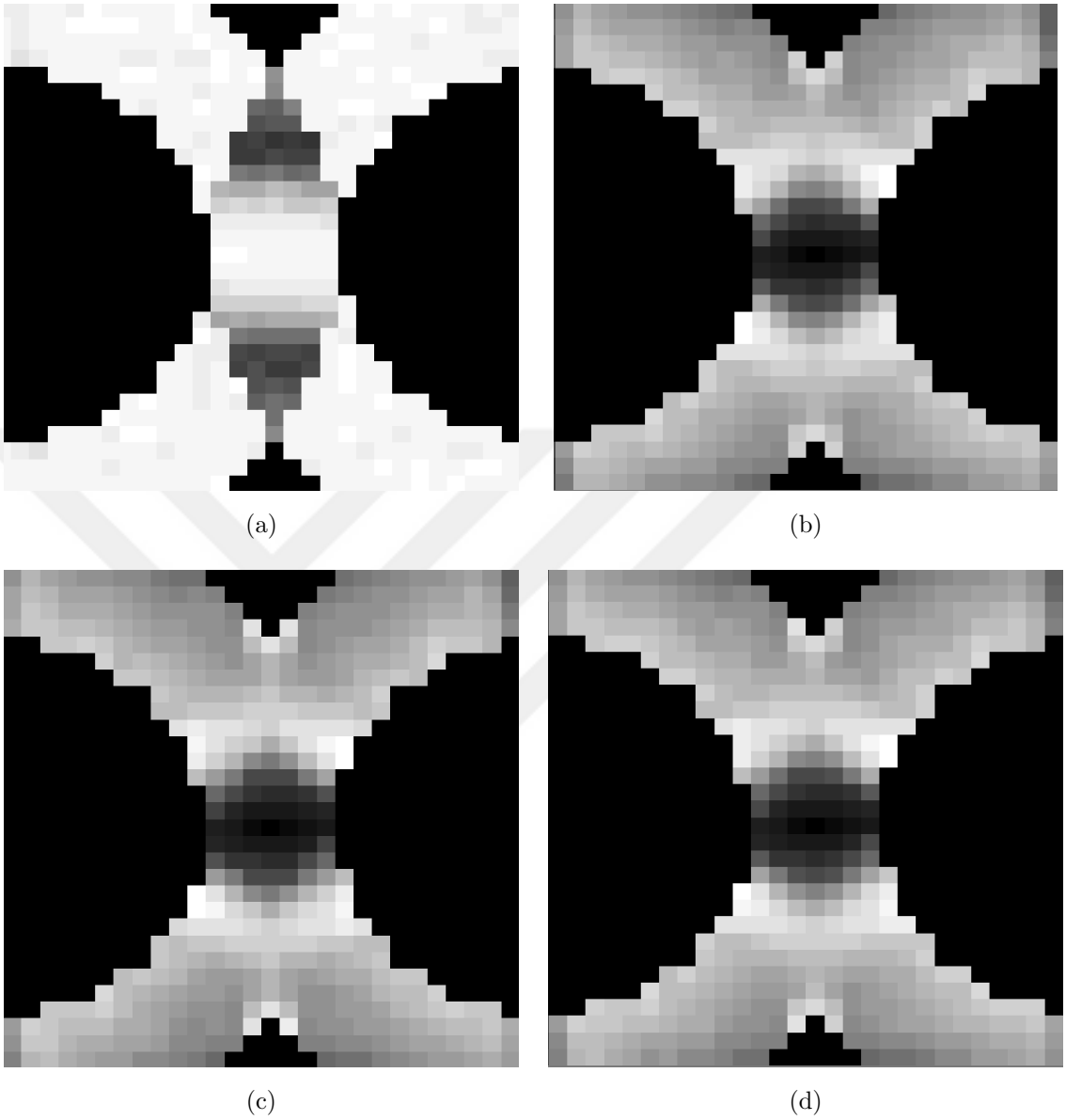
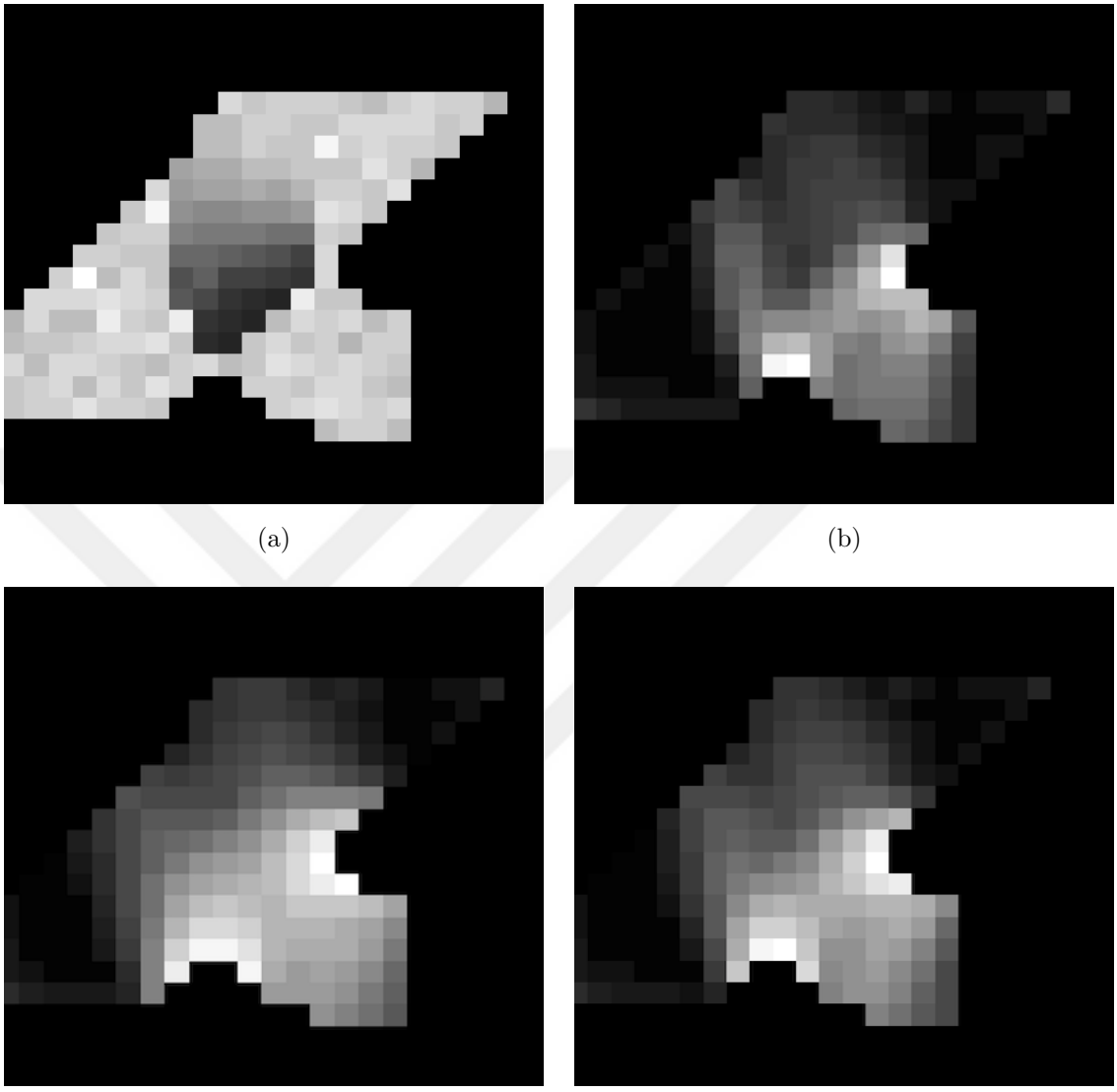


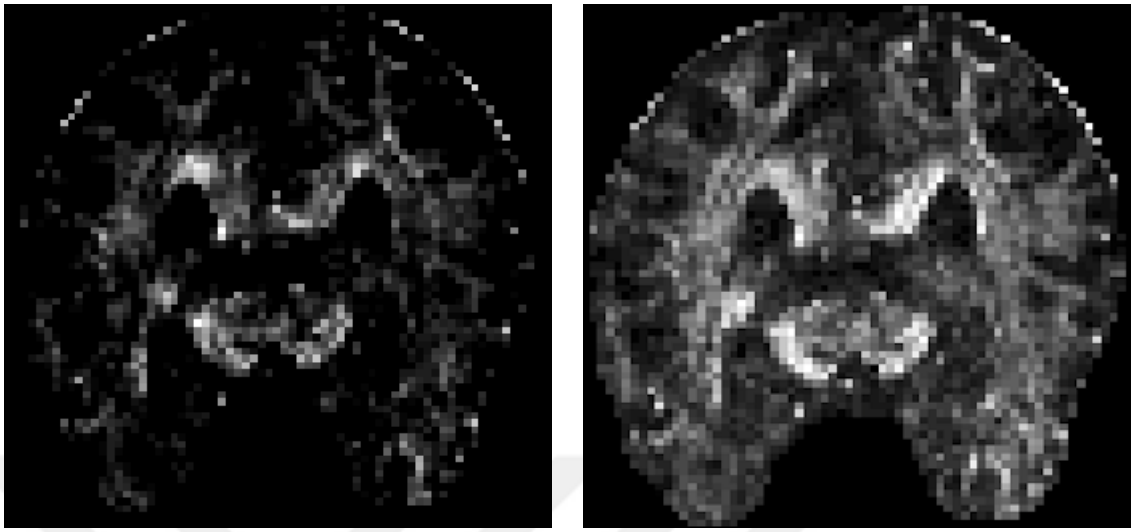
Figure 3.13: *FA (a) and asymmetry (b, c, d) maps (bright-to-dark:high-to-low values) calculated for kissing fibers; (b): Filtering with a Gaussian function; (c): Bilateral filter based on a Gaussian distribution; (d): Steerable Gaussian filter.*



(a) (b)

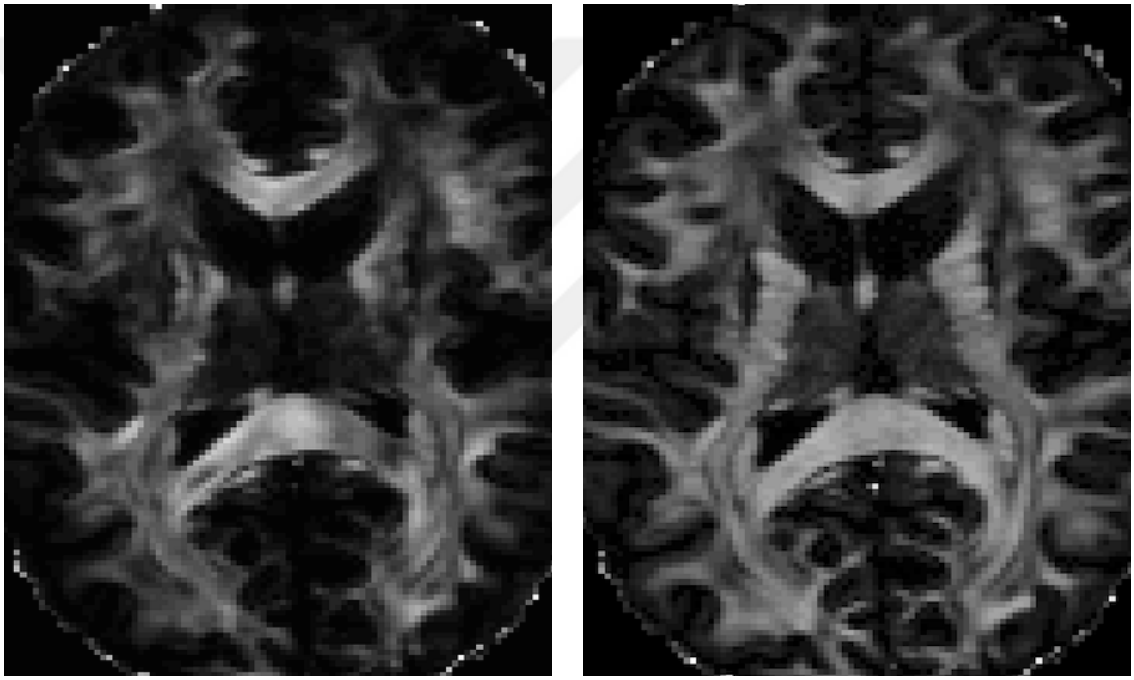
(c) (d)

Figure 3.14: *FA (a) and asymmetry (b, c, d) maps (bright-to-dark:high-to-low values) calculated for branching fibers; (b): Filtering with a Gaussian function; (c): Bilateral filter based on a Gaussian distribution; (d): Steerable Gaussian filter.*



(a) (b)

Figure 3.15: *An axial slice depicting the asymmetry and FA maps on a sample PPMI data in (a) and (b), respectively.*



(a) (b)

Figure 3.16: *An axial slice depicting the computed asymmetry and FA maps on a HCP data sample in (a) and (b), respectively.*

3.5 Discussions and Conclusion

Proposed algorithm is implemented in Matlab and C (Mex), and the experiments are run on a computer with Intel Processor Xeon X560 @ 2.67 GHz CPU computer of 64 GB memory. Our algorithm takes less than 12 mins to create the AODF field based on Gaussian filtering for the whole brain HCP diffusion data with 288 gradient directions and takes less than 5 mins for PPMI data with 64 gradient directions. Time doubles for bilateral filtering and it takes 2,5 times more for steerable filtering. As these filters are suitable for parallel implementations, the AODF directional regularization method can be potentially sped up for practical clinical use.

In all experiments above, clearly the bending in the crossing was captured at the voxel-level representations of the junction regions after the directional regularisation of the ODFs. We provided a validation using the circular bending fibers, whose complex q-space signal is available in analytical form. This facilitated an inverse Fourier transform to obtain the EAPs, and then the reconstruction of the "true" ODF fields based on the DSI method. However, as well-known, this approach based on the the complex q-space signal could only be utilized in this special case, in contrast to real scenarios where the complex signal is not available. The bending intravoxel fiber geometry, which cannot be captured by the symmetric ODFs, is visualized for the true ODF as well as the AODF field obtained from the regularization. Moreover, as expected, the asymmetry is observed to visibly decrease from smaller to larger circles for both the true ODFs and the AODFs.

In the other synthetic experiments, the resulting representation of the local fiber orientations, particularly in splaying sections of the kissing fibers are clearly observed to exhibit the Y-pattern as desired. Steerable filtering can be observed to work the best among the techniques due to its consideration of spatial derivatives of the Gaussian filter which yields the most smoothly reconstructed AODF field.

For the real data experiments, similarly, the reconstructed AODFs clearly display the inherent bending and asymmetry at the voxel level for the corresponding white matter tracts. Comparing this result with that of Figure 3.1, the unique representation capability of the AODF field compared to the ODFs for capturing an improved underlying intravoxel

geometry of fibers is apparent.

For the circularly bending fibers, the asymmetry measure is as expected rotationally invariant and increase from high to low radii (Figure 3.12). This feature is very clearly observed in Figure 3.5, too. Similarly, the proposed measure becomes larger in the asymmetric regions of interest: the circle itself as well as the crossing regions (Figure 3.12), and in the splaying parts of the kissing fibers Figure 3.13, respectively. For the fibers bending slightly, the asymmetry map values decrease as desired in all techniques (Figure 3.12). In Figure 3.13, the asymmetry map values approach zero for the parts of the straight line of fibers that are away from the junction, as desired. The asymmetry values increase over the splaying fibers and the junctions. For the junction region, observe the expected fall in FA measure. In the remaining regions, the FA varies more homogeneously and less informatively in contrast to the asymmetry values. The results show that the steerable filter performs better on all cases as it yields smoother results than the other approaches.

For real data volumes, the asymmetry measure values are substantial for regions with fibers featuring relatively high curvature. The effects of different number of gradient directions as well as different spatial resolutions between the HCP and PPMI data are visible on the computed asymmetry maps. The PPMI asymmetry map is coarse and blocky, while HCP map is smooth, as can be expected. Compared to the FA map, note the asymmetry map is insensitive to bendings on the fiber bundles.

Chapter 4

Vessel Orientation Constrained Quantitative Susceptibility Mapping (QSM) Reconstruction:[6]

QSM is used to estimate the underlying tissue magnetic susceptibility and oxygen saturation in veins. This chapter presents vessel orientation as a new regularization term to improve the accuracy of l_1 or l_2 regularized QSM reconstruction in cerebral veins. For that purpose, the vessel tree is first extracted from an initial QSM reconstruction. In a second step, the vascular geometric prior is incorporated through an orthogonality constraint into the QSM reconstruction. Using a multi-orientation QSM acquisition as gold standard, we show that the QSM reconstruction obtained with the vessel anatomy prior provides up to 40% RMSE reduction relative to the baseline l_1 or l_2 regularizer approaches. We also demonstrate *in vivo* OEF maps along venous veins based on segmentations from QSM. The utility of the proposed method is further supported by inclusion of a separate MRI venography scan to introduce more detailed vessel orientation information into the reconstruction, which provides significant improvement in vessel conspicuity.

[6]The parts of this work will also be reported in: *Medical Image Computing and Computer-Assisted Intervention (MICCAI) 2016-Lecture Notes in Computer Science.*

4.1 Literature Review

QSM is a recently developed venous imaging technique, which gives rise to subtle changes in magnetic tissue susceptibility. Magnetic tissue susceptibility is linearly proportional to the voxel intensity in the QSM data [29, 112, 113]. Since dipolar field patterns have been deconvolved during QSM reconstruction, segmentation of vasculature on QSM images is expected to outperform magnitude- or phase-based approaches. Automated vessel detection may also provide anatomical priors to improve quantification of brain physiology from QSM, including oxygen extraction fraction in cerebral veins. Baseline OEF is an important physiological parameter for tissue health in normal brain function and many cerebrovascular diseases [114]. Reliable estimation of OEF depends on robust and accurate QSM reconstruction within venous structures.

In this study, we present a new regularization constraint to the existing l_1- or l_2-norm regularized QSM reconstruction [28, 115]. The new regularization constraint incorporates prior information about the vessel anatomy and the orientation. The vessel orientation prior is estimated by extracting the vessel tree from QSM data using high order tensor vessel tractography (Chapter 2, [29]). The algorithm flowchart can be summarized in Figure 4.1. As an initialization, an original QSM data is acquired with one of the traditional QSM reconstruction techniques. Then, the vessel tree (vessel surface+centerline+vessel orientation information) is extracted from the original QSM volume. Using the vessel orientation as a prior to l_1- or l_2-norm regularized reconstruction techniques, we reconstruct new QSM images where the vessel branches are enhanced.

4.2 Mathematical Background

4.2.1 l_1- or l_2- regularized QSM reconstruction

To quantify oxygenation along brain vessels requires recovery of the underlying tissue susceptibility distribution from MRI observations of magnetic field perturbations. Tissue susceptibility χ is related to the measured field map ϕ via the formulation $\mathbf{DF}\chi = \mathbf{F}\phi$, where $\mathbf{F}$ is the Fourier transform operator and $\mathbf{D} = 1/3 - k_z^2/k^2$ is the susceptibility kernel

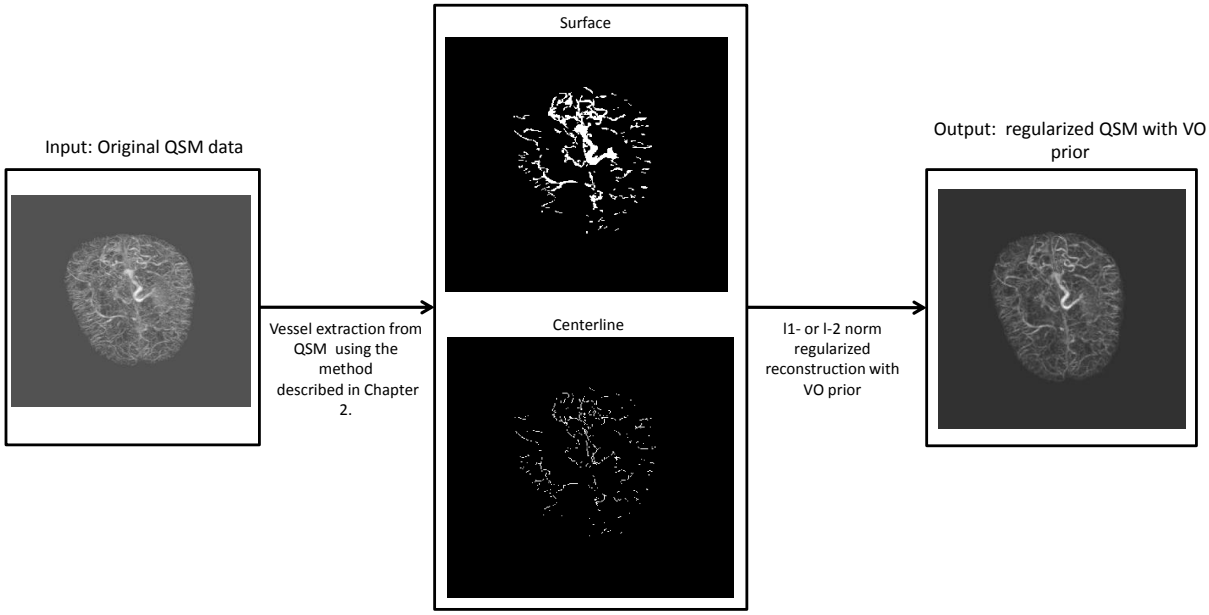


Figure 4.1: *Flowchart of the proposed QSM reconstruction method.*

in k-space. Due to the presence of zeros on the conical surface along the magic angle in this kernel, the solution of this system necessitates additional regularization.

Most popular types of existing QSM reconstruction techniques can be formulated by penalizing l_1- or l_2-norm of gradients in three dimensions [115], and can be expressed as an unconstrained convex optimization problem, minimizing

$$l_1\text{-regularized: } \underset{\chi}{argmin}\ \frac{1}{2}\left\|\mathbf{F^{-1}DF}\chi - \phi\right\|_2^2 + \alpha \cdot \|\mathbf{G}\chi\|_1 \tag{4.1}$$

or

$$l_2\text{-regularized: } \underset{\chi}{argmin}\ \left\|\mathbf{F^{-1}DF}\chi - \phi\right\|_2^2 + \beta \cdot \|\mathbf{G}\chi\|_2^2 \tag{4.2}$$

where α and β are the regularization parameters and $\mathbf{G} = [\mathbf{G_x}; \mathbf{G_y}; \mathbf{G_z}]$ is the gradient operator in three spatial directions.

4.2.2 Oxygen Extraction Fraction (OEF)

Venous oxygen saturation, SvO_2, is a percentage and has value between 0 and 1 (most commonly between 0.5 - 0.8) [116]. It indicates the percentage of hemoglobin molecules that remain oxygenated in blood, after the local brain tissue has consumed the oxygen it needs from the circulation. OEF is the difference between the oxygen content of arterial and venous blood: $OEF = 1 - SvO_2$. The relationship between susceptibility (from the QSM maps) and oxygenation level in the vessel can be formulated as following:

$$\Delta\chi_{vein-water} = (1 - SvO_2) \cdot \Delta\chi_{do} \cdot H_{ct} + \Delta\chi_{oxy-water} \cdot H_{ct} \tag{4.3}$$

where hematocrit (H_{ct}) is the percentage of blood that consists of red blood cells, which is measured for each subject. $\Delta\chi_{do}$ is the susceptibility shift per unit H_{ct} between fully oxygenated and fully deoxygenated red blood cells that is typically assumed $0.27ppm$. $\Delta\chi_{oxy-water}$ is the susceptibility shift between oxygenated blood cells and water, which is assumed as $-0.03ppm$ for all experiments as in [117]. χ_{water} can be estimated from cerebrospinal fluid region (e.g. the anterior part of the brain ventricles). χ_{vein} is calculated at each point in the centerline of the vessel, and χ_{water} should be subtracted from those values to obtain $\Delta\chi_{vein-water}$ along the vessel.

4.3 Method

4.3.1 Segmentation

To extract a brain vessel tree from a given QSM image volume, we utilized our recent framework based on the higher order tensor vessel tractography by [7, 29] (Chapter 2). Starting from a few seed points (e.g. 5-6), an entire cerebral vein tree is captured from the QSM by this technique, which provides the vessel orientation, its centerline (central lumen line), its thickness (vessel lumen diameter), locations of branching points, and lengths of branches. The only interaction to the method is providing seed points which lend themselves to a simple practical vessel extraction process. The computation time for segmentation of the whole vessel tree is on the order of minutes (< 10 min). The extracted

knowledge of centerlines permits OEF computation [116] along the vasculature.

4.3.2 l_1- or l_2- regularized QSM reconstruction with vessel orientation (VO) constraint

We propose a new regularization term to be added to Eq. 4.1 and Eq. 4.2. As a regularizer, we use the dot product between the $\mathbf{G}\chi$ and the orientation vector $\mathbf{V} = [\mathbf{V_x}; \mathbf{V_y}; \mathbf{V_z}] \in \mathbb{R}^{\mathbf{3}}$. The new regularization term incorporates prior information about the vessel anatomy and the orientation. We expect OEF (and thus susceptibility) along the vessel direction to be relatively smooth. Thus, the $\mathbf{G}\chi$ inside a vessel should be orthogonal to the $\mathbf{V}$, and the dot product between $\mathbf{G}\chi$ and $\mathbf{V}$ should be small. The final constraint is weighted by a dilated vessel mask $\mathbf{M}$:

$$\|\boldsymbol{M}\,(\mathbf{G}\cdot\mathbf{V})\chi\|_p^p \tag{4.4}$$

where p is set to 1 for l_1, set to 2 for l_2 regularization. The structuring element in the dilation is a cylinder and the size of its radius is half of the vessel radius. Over each cross section of the vessel along the centerline, $\mathbf{V}$ is defined at each voxel as the difference between two consecutive centerline points. Then, $\mathbf{V}$ is weighted by a smooth surface, which enhances it along the edges and suppresses along the centerline of the vessel and outside of $\mathbf{M}$ (Figure 4.2).

Hence, the l_1-regularized and vessel orientation constrained reconstruction problem reads as:

$$\underset{\chi}{\operatorname{argmin}}\ \frac{1}{2}\left\|\mathbf{F^{-1}DF}\chi-\phi\right\|^2+\alpha\cdot\|\mathbf{G}\chi\|_1+\lambda\,\|\mathbf{M}(\mathbf{G}\cdot\mathbf{V})\chi\|_1 \tag{4.5}$$

where α and λ are the regularization parameters.

We perform the optimization by non-linear conjugate gradient with backtracking line-search using 200 iterations (See Algorithm 1) [118][7].

The l_2-regularized and vessel orientation constrained reconstruction problem can be formulated as following:

$$\underset{\chi}{\operatorname{argmin}}\ \left\|\mathbf{F^{-1}DF}\chi-\phi\right\|^2+\beta\cdot\|\mathbf{G}\chi\|_2^2+\gamma\,\|\mathbf{M}(\mathbf{G}\cdot\mathbf{V})\chi\|_2^2\,, \tag{4.6}$$

[7]The "Sparse MRI" algorithm is available online: http://people.eecs.berkeley.edu/ mlustig/Software.html

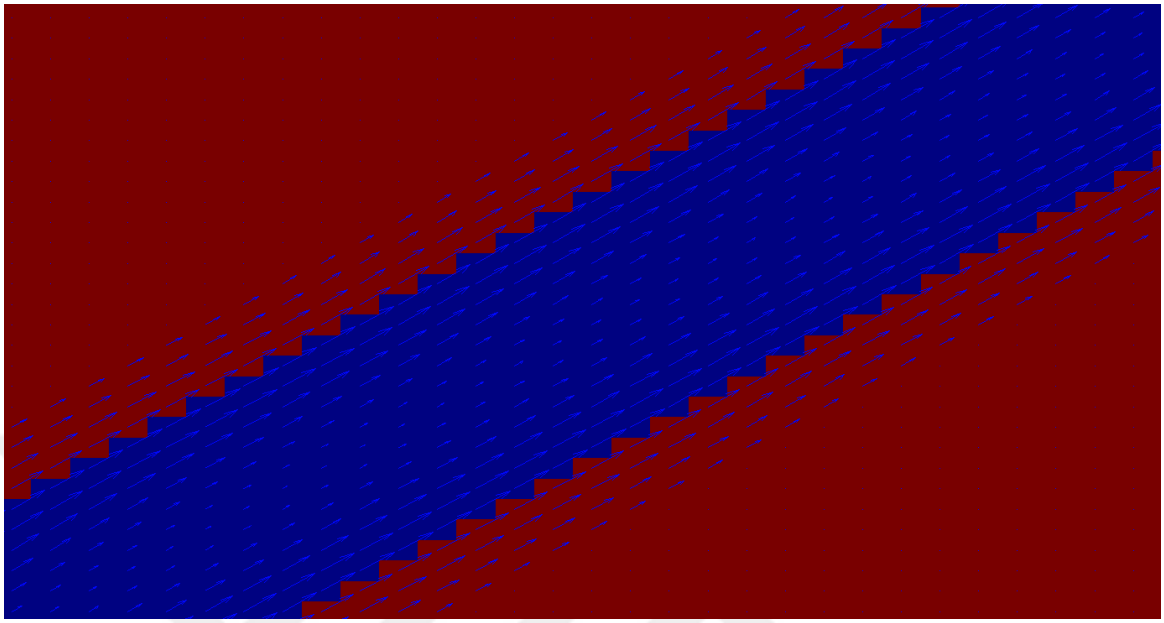


Figure 4.2: *Illustration of vessel prior on a region of a vessel branch.*

Algorithm 1 *l1-norm regularized non-linear conjugate gradient with backtracking line-search*

procedure L1VQSM($\mathbf{D}$, $\mathbf{F}$, ϕ, $\mathbf{G}$, α, λ, $\mathbf{V}$, $\mathbf{M}$)

Precomputation: $\mathbf{DF}\chi$, $\mathbf{DF}\boldsymbol{\Delta}\chi$, $\mathbf{G}\chi$, $\mathbf{G}\boldsymbol{\Delta}\chi$, $\mathbf{M}(\mathbf{G}\cdot\mathbf{V})\chi$, $\mathbf{M}(\mathbf{G}\cdot\mathbf{V})\boldsymbol{\Delta}\chi$

Line Search:

$\underset{\tau}{argmin}\ \ \frac{1}{2}\left\|\mathbf{DF}(\chi+\tau\Delta\chi)-\mathbf{F}\phi\right\|_2^2+\alpha\left\|\mathbf{G}(\chi+\tau\Delta\chi)\right\|_1+\gamma\left\|\mathbf{M}(\mathbf{G}\cdot\mathbf{V})(\chi+\tau\Delta\chi)\right\|_1$

for step size τ **do**

χ update: $\chi=\chi+\tau\Delta\chi$

gradient update:

$g_{new}=\mathbf{F}^{-1}\mathbf{D}(\mathbf{DF}\chi-\mathbf{F}\phi)+\alpha\mathbf{G}^T\text{sign}(\mathbf{G}\chi)+\lambda(\mathbf{V}\cdot\mathbf{G})\mathbf{M}^T sign(\mathbf{M}(\mathbf{G}\cdot\mathbf{V})\chi)$

parameter update: $b=\left\|g_{new}\right\|_2/\left\|g_{prev}\right\|_2$, $g_{prev}=g_{new}$

$\Delta\chi$ update: $\Delta\chi=b\cdot\Delta\chi-g_{new}$

end for

end procedure

where β and γ are the regularization parameters. The algorithm can be summarized as in Algorithm 2.

Algorithm 2 *l2-norm regularized non-linear conjugate gradient with backtracking line-search*

procedure L2VQSM($\mathbf{D}$, $\mathbf{F}$, ϕ, $\mathbf{G}$, α, λ, $\mathbf{V}$, $\mathbf{M}$)

Precomputation: $\mathbf{DF}\chi$, $\mathbf{DF}\boldsymbol{\Delta}\chi$, $\mathbf{G}\chi$, $\mathbf{G}\boldsymbol{\Delta}\chi$, $\mathbf{M}(\mathbf{G}\cdot\mathbf{V})\chi$, $\mathbf{M}(\mathbf{G}\cdot\mathbf{V})\boldsymbol{\Delta}\chi$

Line Search:

$\underset{\tau}{argmin} \quad \|\mathbf{DF}(\chi+\tau\Delta\chi)-\mathbf{F}\phi\|_2^2+\beta\|\mathbf{G}(\chi+\tau\Delta\chi)\|_2^2+\gamma\|\mathbf{M}(\mathbf{G}\cdot\mathbf{V})(\chi+\tau\Delta\chi)\|_2^2$

for step size τ **do**

χ update: $\chi=\chi+\tau\Delta\chi$

gradient update:

$g_{new}=(\mathbf{F}^{-1}\mathbf{D}^2\mathbf{F}+\beta\mathbf{G}^T\mathbf{G}+\gamma\mathbf{V}^T\mathbf{G}\mathbf{M}^2\mathbf{G}^T\mathbf{V})\chi-\mathbf{F}^{-1}\mathbf{DF}\phi$

parameter update: $b=\|g_{new}\|_2\,/\,\|g_{prev}\|_2$, $g_{prev}=g_{new}$

$\Delta\chi$ update: $\Delta\chi=b\cdot\Delta\chi-g_{new}$

end for

end procedure

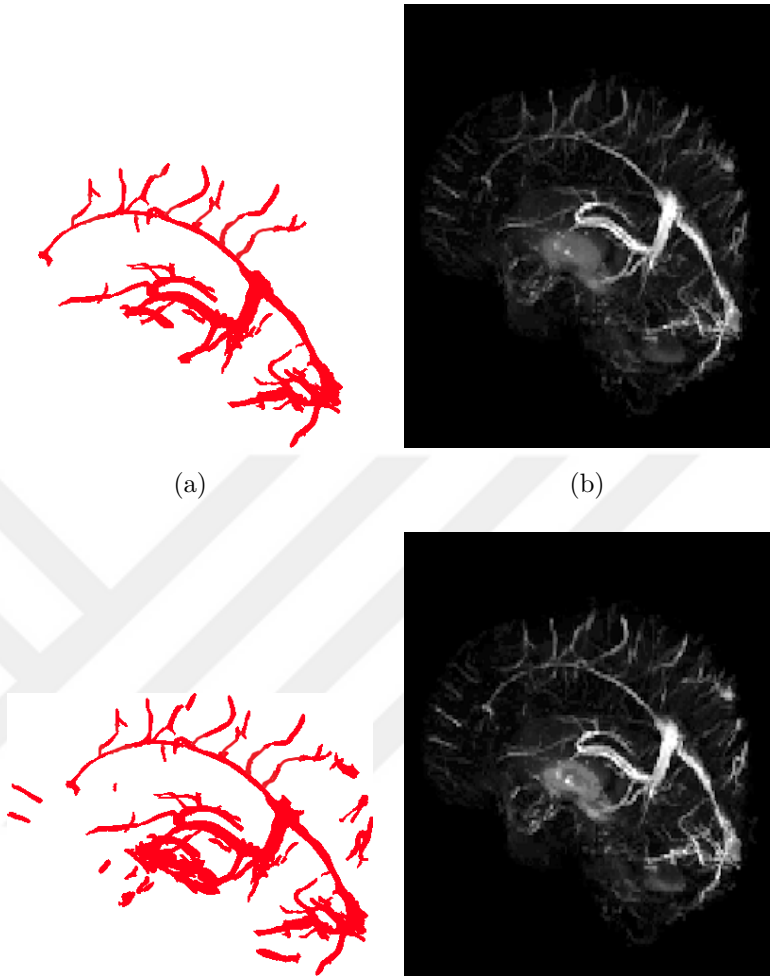
4.4 Experimental Results

In this section, we will show the results of the l_1- or l_2-regularized QSM reconstruction with VO constraint on: (Section 4.4.1) a ground truth *in vivo* validation data; (Section 4.4.2) *in vivo* QSM volumes acquired on ten healthy volunteers; (Section 4.4.3) a single *in vivo* QSM volume registered with a contrast-enhanced Fast Spin Echo MRI (MFAST) data. The regularization parameters (α, λ, β, γ) were determined by parameter sweeping based on the validation data. The values ($\alpha=8.3\cdot10^{-4}$, $\lambda=3.5\cdot10^{-2}$, $\beta=3.4\cdot10^{-2}$, $\gamma=6.310^{-3}$) that minimized the normalized root mean square error (RMSE) relative to the true χ were selected to be the optimal setting, and applied in all experiments.

4.4.1 Validation data

A ground truth *in vivo* QSM dataset is obtained using 3D-Gradient Echo (GRE) acquisition at 12 different head orientations relative to the main magnetic field. Since the dipole kernel $\mathbf{D}$ varies as a function of the angle between the subject's head and the main field, an overdetermined system can be formed using data from multiple orientations to mitigate the ill-conditioning of dipole inversion. This technique is termed Calculation Of Susceptibility through Multiple Orientation Sampling (COSMOS) and obviates the need for additional regularization [119] to provide ground-truth quality susceptibility maps. For this acquisition, a healthy volunteer (female, age 30) was scanned with a 32-channel head coil on a Siemens 3T Trio system using TR/TE = 35/25 ms at 1 mm isotropic resolution with BW = 100 Hz/pixel upon 15-fold acceleration with the Wave-CAIPI sequence [120]. Raw phase images were processed using Laplacian unwrapping [121] and SHARP background removal [122] to yield tissue phase images from each orientation, which were jointly inverted to provide the COSMOS χ solution. Using the COSMOS reconstruction as the ground truth χ map, the field map ϕ was simulated using the forward dipole model $\phi = \mathbf{F^{-1}DF}$, and Gaussian noise ($\sigma = 0.01$) was added.

Starting from the noisy field map, l_1-reconstruction results in 8.37% and l_2-reconstruction yields 17.37% RMSE, which are calculated in the whole volume. We segmented the vessel tree from the χ map using the higher order tensor based vessel extraction method described in Section 4.3.1. Figure 4.3(a,c) depicts the extracted vessel tree with two levels of detail in segmentation. The results of less detailed (4 seed points are used) and high detailed segmentation (7 seed points are used) are depicted in Figure 4.3(a) and Figure 4.3(c), respectively. l_1 regularized reconstruction with VO constraint has RMSE error of 6.27% with less detailed segmentation and 5.13% with more detailed segmentation (Figure 4.3 (b) and Figure 4.3 (d)). l_2 regularized reconstruction with VO constraint has RMSE error of 13.38% with less detailed segmentation and 11.23% with more detailed segmentation (Figure 4.4). We observe that when the segmentation becomes more detailed, VO constraint is more effective in the reconstruction, thus RMSE decreases along the vessels. The results show that the improvement in the accuracy of the reconstruction with our vessel orientation constraint over the existing l_1 reconstruction is 40%. Qualitatively, it can be

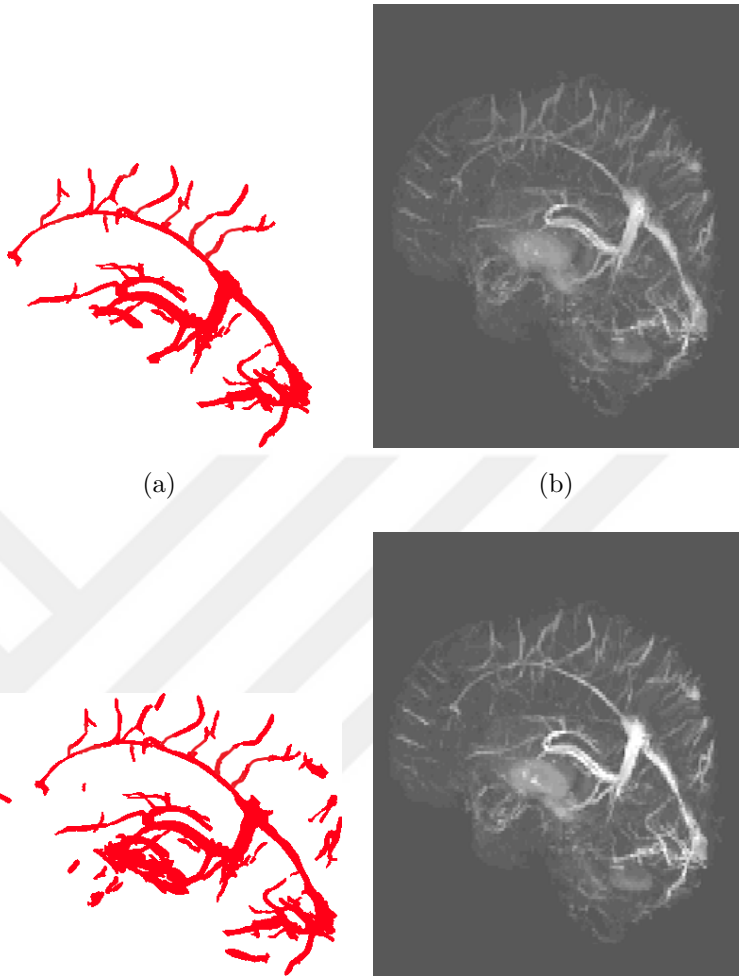


(a) (b)

(c) (d)

Figure 4.3: *A ground truth* in vivo *phantom data from QSM image with 12-orientations; (a) the less detailed vessel tree from the phantom data; (b) the result of* l_2 *regularized reconstruction with VO constraint for the less detailed vessel tree segmentation (4 seed points are used for vessel segmentation, and the reconstruction has* 13.38% *RMSE); (c) the more detailed vessel tree from the phantom data; (d) the result of* l_1 *regularized reconstruction with VO constraint for the more detailed vessel tree segmentation (7 seed points are used for vessel segmentation, and the reconstruction has* 5.13% *RMSE).*

observed that smaller vessels are more visible in the reconstructions regularized with the additional VO constraint (Figure 4.5).



(a) (b)

(c) (d)

Figure 4.4: *A ground truth* in vivo *phantom data from QSM image with 12-orientations; (a) the less detailed vessel tree from the phantom data; (b) the result of* l_2 *regularized reconstruction with VO constraint for the less detailed vessel tree segmentation (4 seed points are used for vessel segmentation, and the reconstruction has* 6.27% *RMSE); (c) the more detailed vessel tree from the phantom data; (d) the result of* l_1 *regularized reconstruction with VO constraint for the more detailed vessel tree segmentation (7 seed points are used for vessel segmentation, and the reconstruction has* 11.23% *RMSE).*

4.4.2 *in vivo MRI data*

Ten young, healthy volunteers were scanned with a 32-channel coil on a Siemens 3T Trio system. 3D-GRE images for susceptibility mapping were acquired with full flow-

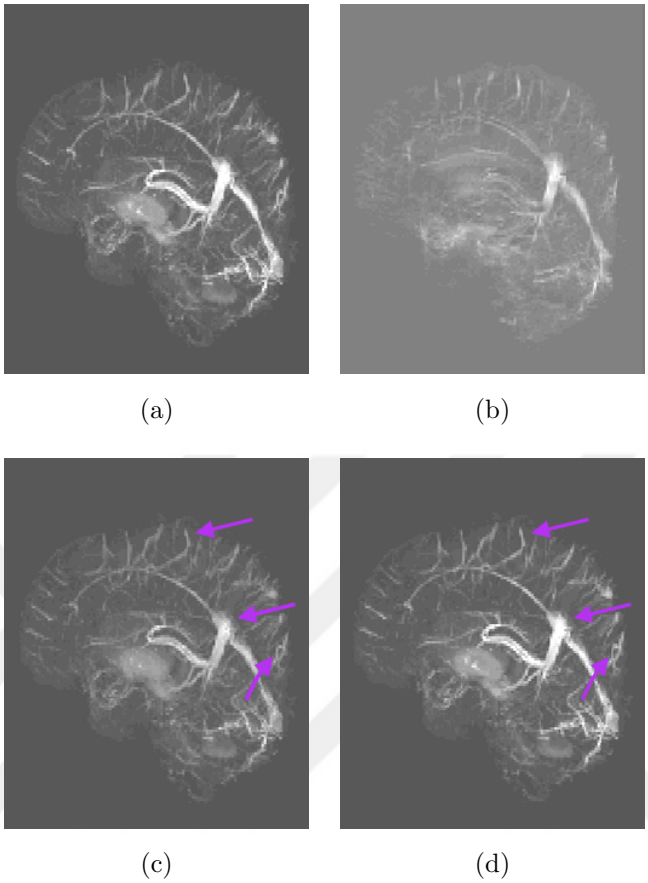


Figure 4.5: *Simulations result from ground truth susceptibility phantom. RMSE values were computed using a known ground truth susceptibility map. (a) Original χ field; (b) noisy normalized field map (input to QSM reconstruction); (c) l_1 regularized reconstructed χ field (*8.37% *RMSE); (d) l_1 regularized reconstructed with VO constraint χ field (*5.13% *RMSE). Arrows point out the reconstruction comparisons on the sample veins.*

compensation along each axis at all echoes. Axial magnitude and phase images were collected with TR = $23ms$; TE = $7.2/17.7ms$; resolution = $0.875 \times 0.875 \times 1mm^3$, matrix = $226 \times 256 \times 144$; and BW = 260Hz/pixel. Phase images were combined offline and processed with Laplacian unwrapping [121]. Background field was removed with SHARP filtering [122] and QSM reconstruction was performed with a l_1 regularized reconstruction technique [28].

Figure 4.6 depicts the QSM map, centerlines and surfaces of the vessel trees on two healthy volumes. We compute the OEF values after the l_1 regularized reconstruction with

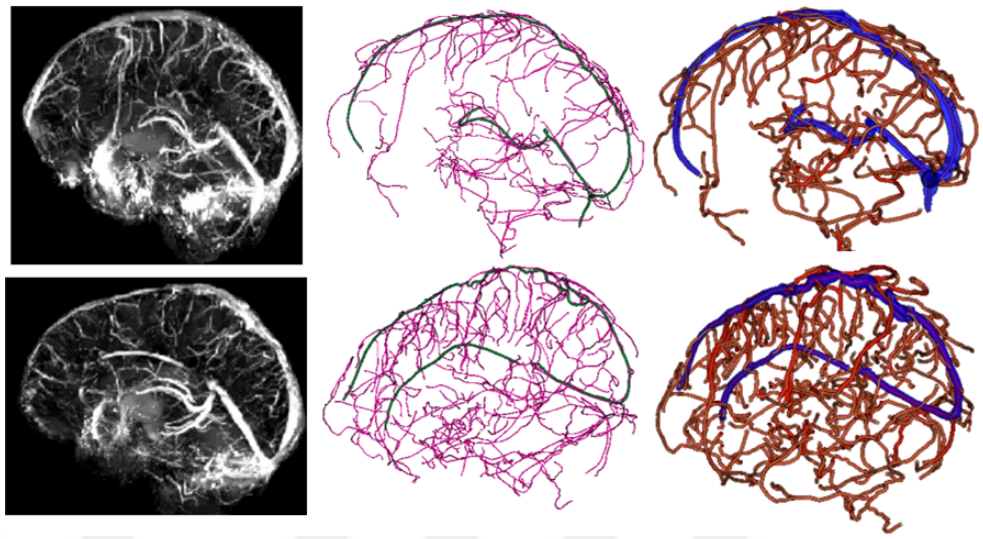


Figure 4.6: *(Left Column) Original QSM map; (Middle Column) extracted centerlines of the vessels; (Right Column) surface renderings for the vessels are shown for two healthy subjects.*

VO constraint on the same subjects. Mean OEF of l_1 regularized reconstruction with VO constraint results across all veins are $33.3 \pm 4\%$, $35.7 \pm 7\%$, $31.7 \pm 3\%$, $38.6 \pm 5\%$, $37.4 \pm 6\%$, $33.8 \pm 3\%$, $33.7 \pm 2\%$, $35.7 \pm 5\%$, $31.9 \pm 4\%$, and $34.3 \pm 9\%$ respectively, for each of ten subjects. Estimated OEF for straight sinus, sagittal sinus, pial vessels are $46.3 \pm 6\%$, $36.4 \pm 4\%$, $31.8 \pm 3\%$, respectively, in average of ten subjects. Furthermore, we display the OEF values on the vessel surfaces of the sample two subjects, where the VO constraint is shown to improve conspicuity of smaller vessels (Figure 4.7)).

4.4.3 QSM + MFAST data

The experiment in Section 4.4.2 first uses standard QSM reconstruction (generic prior) and segments the vessels from this initial estimate of susceptibility. Here we test the hypothesis that vessel tree extraction from a separate angiographic volume offers improved vascular priors for OEF quantification from QSM maps.

With IRB approval, patients were scanned on a 3T GE scanner (MR750, GE Healthcare Systems, Waukesha, WI) with an 8-channel head-coil. A flow-compensated 3D parallel-imaging-accelerated multi-echo (ME)-GRE sequence was used with the following param-

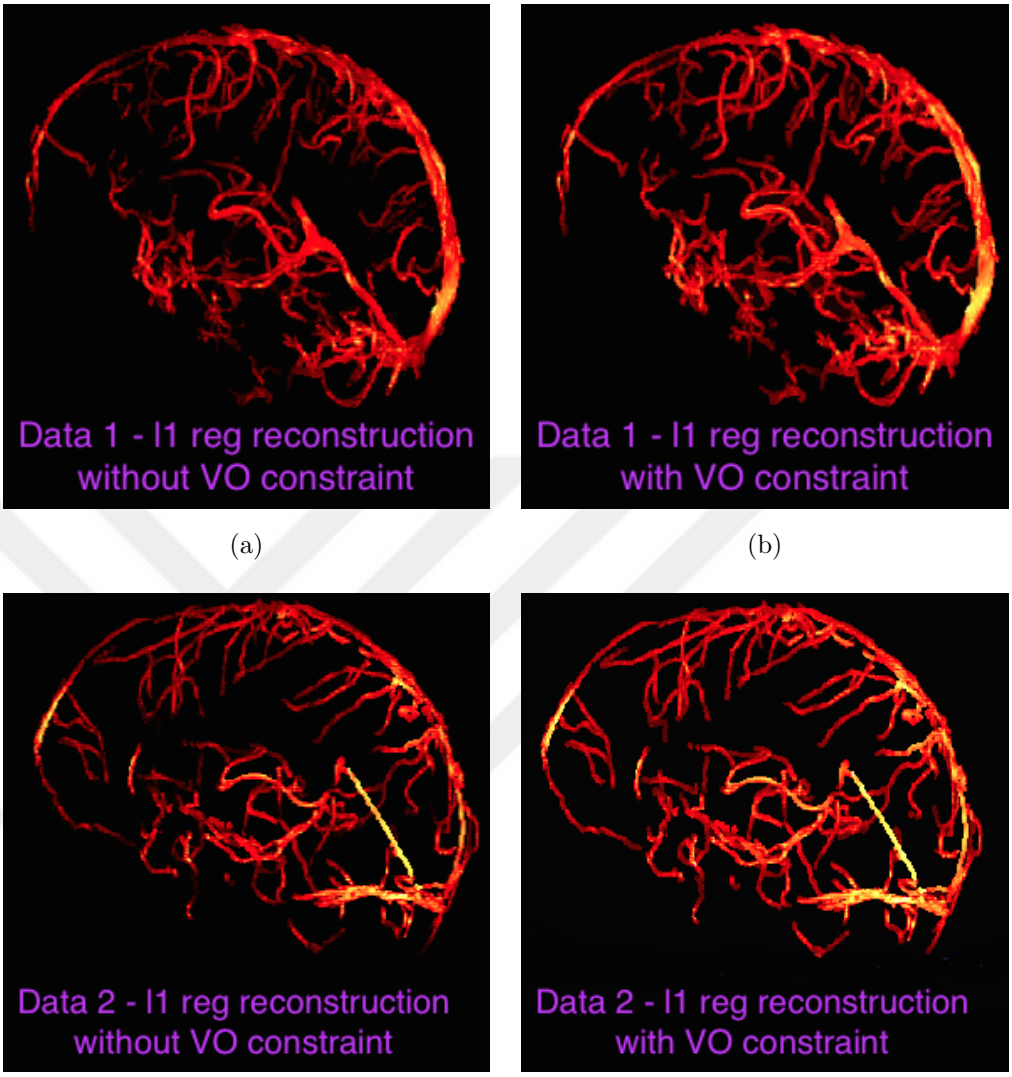


Figure 4.7: *OEF visualization on two sample subjects from ten data volume (shown in hot colors); (a) QSM reconstruction without vessel orientation is shown on the first subject; (b) the result of l_1 regularized reconstruction with VO constraint is shown on the first subject; (c) QSM reconstruction without vessel orientation is shown on the second subject; (d) the result of l_1 regularized reconstruction with VO constraint is shown on the second subject.*

eters: Axial plane, FOV = $22cm$, matrix size = 384×256, number of partitions = 66, resolution = $0.6 \times 0.9 \times 2mm^3$, acceleration factor = 2, flip angle = $15°$, TR = $36ms$, seven echoes ranging from TE = $4 - 33ms$ ($4.8ms$ increments), scan time = $5.44min$. On completion of the scan, the raw data from the scanner were automatically reconstructed

using compiled threaded MATLAB code.

A ferumoxytol-enhanced MRA using 3D SPGR was designed with short repetition time (TR) = 4ms and echo time (TE) = 1ms. The sequence was fat suppressed with FOV = $26cm$, matrix size = 416×416, resolution = $0.625 \times 0.625mm^2$ and 180 slices with 1mm thickness. The excitation was done with a flip angle of 15 degrees and receiver bandwidth of $62.5kHz$. The scan time was reduced by not acquiring the corners of ky-kz space, producing an acquisition time of $5.46min$.

We first extracted the brain using FSL [123] from MFAST data, then registered MFAST and QSM data with a rigid registration using the MedInria software [124]. Using the QSM reconstruction as the reference χ map, the field map ϕ was simulated using the forward dipole model, and Gaussian noise was added ($\sigma = 0.02$). Then, we segmented the vessel tree from QSM data and MFAST data separately. Figure 4.8 (Top row) shows the vessel tree segmentation from QSM and MFAST data, respectively. We use morphological operators to separate veins from arteries for the MFAST data. Figure 4.8 (Bottom row) visualizes the results of: (First column) QSM reconstruction without the vessel orientation prior; (Second column) QSM reconstruction with the vessel orientation prior, where the vessel tree is segmented from the QSM data; (Third column) QSM reconstruction with the vessel orientation prior where the vessel tree is segmented from the MFAST data. The results show the enhancements along the veins using our VO prior in the reconstructions. The amount of detail captured in the vessel tree extracted from the MFAST data volume, which is then incorporated into the QSM reconstruction through the VO regularizer clearly reveals the benefits of the new regularizer term.

4.5 Discussions and Conclusion

We developed a method that improves the accuracy of l_1 regularized QSM reconstruction [28, 115] with a new regularization constraint, vessel orientation. Quantitative performance of our method was demonstrated on a ground truth phantom data. Furthermore, we performed the experiments on ten QSM images reconstructed from MRI phase and presented the mean OEF results for all veins in each volume and major vessel segments.

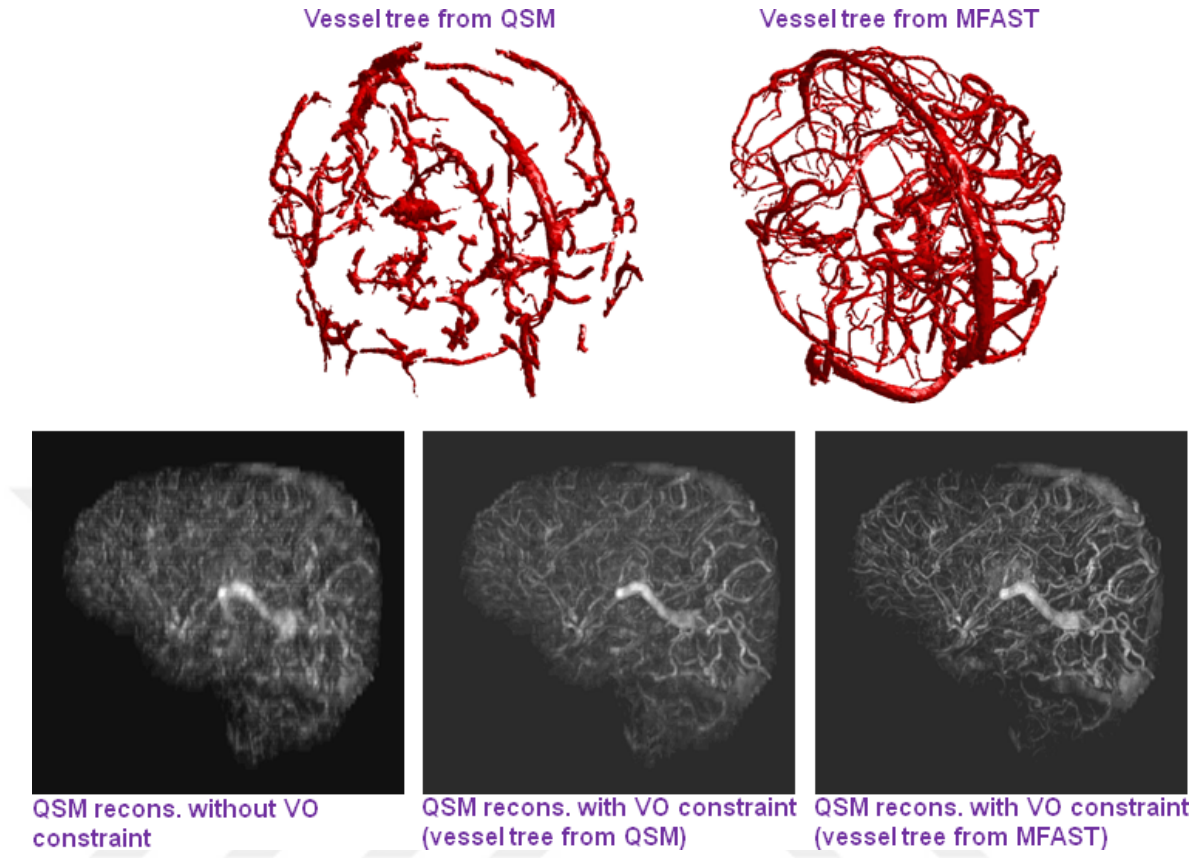


Figure 4.8: *Top row: Left Column-vessel tree extraction from QSM data, Right Column-vessel tree extraction from MFAST data ; Bottom row: (First column) QSM reconstruction without vessel orientation, (Second column) l_1-reg QSM data reconstructed with vessel orientation constraint (Vessel tree is extracted from the QSM data), (Third column) l_1-reg QSM data reconstructed with vessel orientation constraint (vessel tree is extracted from the MFAST data).*

On two sample subjects, we showed that the OEF maps along the vessel direction are relatively smooth. Finally, we compared the QSM reconstructions on a QSM volume acquired with an additional contrast, the MFAST. We showed the results for QSM reconstructions with and without vessel orientations, where the vessel trees were segmented from QSM and MFAST data, respectively. This experiment implied that when the segmentation becomes more detailed and accurate, the quality of the reconstruction increases. Use of the vessel orientation constraint increased OEF values (Figure 4.7), such that our results are more in line with physiological OEF values reported by O-15 PET imaging [125]. This

observation suggests that the use of anatomical prior helps mitigate partial volume effects and over-smoothing associated with traditional regularized QSM reconstruction. The new OEF values may also reflect less underestimation due to vessel orientation because of the vascular prior.

Chapter 5

Summary of Contributions and Conclusion

Segmentation of human vasculatures is a fundamental step for accurate visualization of vessels and assessment of cardio- and cerebro-vascular diseases, e.g atherosclerosis and stroke. Computationally created 3D models of vessels are used as a virtual medical navigation tool and in investigation of possible anomalies in arteries and veins. In the first part of this thesis, a new vascular structure segmentation method, which is based on a cylindrical flux-based HOT was developed. The HOT naturally models branching geometry of vessels including n-furcations, which is challenging for the vessel segmentation methods. In a general linear HOT model embedded in 3D, one has to work with an even order tensor due to an enforced antipodal-symmetry on the unit sphere. However, in scenarios such as in a bifurcation, the antipodally-symmetric tensor embedded in 3D will not be useful. In order to overcome that limitation, we embed the tensor in 4D and obtain a structure that can model asymmetric junction scenarios. During the construction of a higher order tensor (e.g. third or fourth order) in 4D, the orientation vectors lie on the unit 3-sphere, in contrast to the unit 2-sphere in 3D tensor modeling. This 4D tensor is exploited in a seed-based vessel segmentation algorithm, where the principal directions of the 4D HOT is obtained by decomposition, and used in a HOT tractography approach. We demonstrated quantitative validation of the proposed algorithm on varying vasculatures and modalities: synthetic complex tubular structures, cerebral arteries

of MRA images from the MIDAS-MRA dataset [84] and coronary arteries of CTA images from Rotterdam Coronary Artery Evaluation Framework [82]. In MIDAS-MRA dataset, we compared our results with almost manual segmentation results described in [8], and obtained $95.02 \pm 0.89\%$ accuracy in overall. Besides, the algorithm only requires single seed point for the extraction of whole vessel tree, and the whole process takes less than 30 seconds. Rotterdam Coronary Artery Evaluation Framework facilitates standardized evaluations of the centerline extraction methods over common datasets with ground truth and with standard performance measure. There are 24 methods evaluated so far in three categories: automatic, semi-automatic, interactive. We ranked the 1^{st} among semi-automatic algorithms category.

In the second part of this thesis, a DMRI processing method was presented for representing the inherent asymmetry of the underlying intravoxel geometry, which emerges in regions with bending, crossing, or sprouting fibers. The ODFs obtained through conventional approaches such as q-ball imaging [65] and spherical deconvolution [91] result in symmetric ODF profiles at each voxel even when the underlying geometry is asymmetric. To extract such inherent asymmetry, we employed inter-voxel filtering approaches (Gaussian, bilateral and steerable) through a cone model, which facilitate a sharpening of the ODFs in some directions while suppressing peaks in other directions, thus yielding an AODF field. AODFs reveal more information regarding the cytoarchitectural organization within the voxel compared to symmetric ODFs. The level of asymmetry is quantified via a new scalar index that could complement standard measures of diffusion anisotropy. Experiments on synthetic geometries of circular, crossing, and kissing fibers show that the estimated AODFs successfully recover the asymmetry of the underlying geometry. The feasibility of the techniques were demonstrated and compared on a complex synthetic bending fiber simulation, INRIA synthetic crossing fibers examples and *in vivo* data obtained from the HCP and PPMI Project database.

In the last part of this thesis, an l_1- and l_2-norm regularized QSM reconstruction with a new prior in cerebral veins were proposed. First, the vessel tree was extracted from an initial QSM reconstruction. In a second step, the vascular geometric prior was incorporated through an orthogonality constraint into the QSM reconstruction. Using a

multi-orientation QSM acquisition as gold standard, we showed that the QSM reconstruction obtained with the vessel anatomy prior provides up to 40% RMSE reduction relative to the baseline l_1 regularizer approach. We also demonstrated *in vivo* OEF maps along venous veins based on segmentations from QSM. The utility of the proposed method is further supported by inclusion of a separate MRI venography (MFAST) scan to introduce more detailed vessel orientation information into the reconstruction, which provides significant improvement in vessel conspicuity.

One potential future application of HOT vessel tractography method can be the detection and modeling of the pathologies such as aneurysms using HOTs. Generic tractography algorithms may not accurately find the WM fiber tracts for AODFs, since their model is mostly based on even order SH. AODF tractography algorithm can be developed as another future application. As an extension of our QSM reconstruction work, an idea to pursue is extracting the vessel prior from the enhanced QSM image and iterating the whole procedure a few times until there is no change in the reconstructed QSM. Both the number of vessel branches and OEF values over the iteration number can be monitored to unveil vein structure and physiology in health and diseases in population studies.

Bibliography

[1] Medchrome, "Coronary circulation." [Online]. Available: http://tube.medchrome.com/2011/04/coronary-circulation-anatomy.html

[2] B. staff., "Blausen gallery 2014," *Wikiversity Journal of Medicine*.

[3] N. EMS, "Blood flow through the brain." [Online]. Available: http://www.neuroems.com/2014/04/18/blood-flow-through-the-brain-pt-3-circle-of-willis/

[4] H. Gray, *Anatomy of the Human Body*. Lea & Febiger, 1918.

[5] C. Westbrook, *MRI at a glance*, 2nd ed. Wiley-Blackwell, 2010.

[6] T. Schultz and H.-P. Seidel, "Estimating crossing fibers: A tensor decomposition approach." *IEEE Trans. Vis. Comput. Graph.*, vol. 14, no. 6, pp. 1635–1642, 2008.

[7] S. Cetin, A. Demir, A. J. Yezzi, M. Degertekin, and G. Unal, "Vessel tractography using an intensity based tensor model with branch detection." *IEEE Trans. Med. Imaging*, vol. 32, no. 2, pp. 348–363, 2013.

[8] H. Bogunovic, J. Pozo, R. Cardenes, L. San Roman, and A. Frangi, "Anatomical labeling of the circle of willis using maximum a posteriori probability estimation," *Medical Imaging, IEEE Transactions on*, vol. 32, no. 9, pp. 1587–1599, 2013.

[9] D. S. Tuch, "Q-ball imaging," *Magn Reson Med*, vol. 52, pp. 1358–1372, 2004.

[10] M. Descoteaux, *High Angular Resolution Diffusion Imaging (HARDI)*. John Wiley and Sons, Inc., 1999.

[11] E. Özarslan, C. G. Koay, and P. J. Basser, "Remarks on q-space MR propagator in partially restricted, axially-symmetric, and isotropic environments," *Magn Reson Imaging*, vol. 27, no. 6, pp. 834–844, 2009.

[12] E. Özarslan, T. M. Shepherd, B. C. Vemuri, S. J. Blackband, and T. H. Mareci, "Resolution of complex tissue microarchitecture using the diffusion orientation transform (DOT)," *NeuroImage*, vol. 31, no. 3, pp. 1086–1103, 2006.

[13] F. Dell'Acqua, P. Scifo, G. Rizzo, M. Catani, A. Simmons, G. Scotti, and F. Fazio, "A modified damped Richardson-Lucy algorithm to reduce isotropic background effects in spherical deconvolution," *NeuroImage*, vol. 49, no. 2, pp. 1446 – 1458, 2010.

[14] P. Libby, "Inflammation in atherosclerosis," *Nature*, vol. 420, pp. 868–874, 2002.

[15] Z. A. Fayad, V. Fuster, K. Nikolaou, and C. Becker, "Concepts coronary angiography and plaque imaging: Current and potential future computed tomography and magnetic resonance imaging for noninvasive," 2010.

[16] E. R. Melhem, S. Mori, G. Mukundan, M. A. Kraut, M. G. Pomper, and P. C. van Zijl, "Diffusion Tensor MR Imaging of the Brain and White Matter Tractography," *Am. J. Roentgenol.*, vol. 178, no. 1, pp. 3–16, Jan. 2002.

[17] B. J. Jellison, A. S. Field, J. Medow, M. Lazar, M. S. Salamat, and A. L. Alexander, "Diffusion tensor imaging of cerebral white matter: A pictorial review of physics, fiber tract anatomy, and tumor imaging patterns," *AJNR*, vol. 25, no. 3, pp. 356–369, 2004.

[18] Y. Wang and T. Liu, "Quantitative susceptibility mapping (qsm): Decoding mri data for a tissue magnetic biomarker," *Magnetic Resonance in Medicine*, vol. 73, no. 1, pp. 82–101, 2015.

[19] C. Langkammer, F. Schweser, N. Krebs, A. Deistung, W. Goessler, E. Scheurer, K. Sommer, G. Reishofer, K. Yen, F. Fazekas, S. Ropele, and J. R. Reichenbach,

"Quantitative susceptibility mapping (qsm) as a means to measure brain iron? a post mortem validation study," *NeuroImage*, vol. 62, no. 3, pp. 1593 – 1599, 2012.

[20] W. Zheng, H. Nichol, S. Liu, Y.-C. N. Cheng, and E. M. Haacke, "Measuring iron in the brain using quantitative susceptibility mapping and x-ray fluorescence imaging," *NeuroImage*, vol. 78, pp. 68 – 74, 2013.

[21] A. P. Fan, T. Benner, D. S. Bolar, B. R. Rosen, and E. Adalsteinsson, "Phase-based regional oxygen metabolism (prom) using mri," *Magnetic Resonance in Medicine*, vol. 67, no. 3, pp. 669–678, 2012.

[22] E. Haacke, J. Tang, J. Neelavalli, and Y. Cheng, "Susceptibility mapping as a means to visualize veins and quantify oxygen saturation," *Journal of Magnetic Resonance Imaging*, vol. 33, no. 6, pp. 1527–1529, 6 2011.

[23] C. Langkammer, T. Liu, M. Khalil, C. Enzinger, M. Jehna, S. Fuchs, F. Fazekas, Y. Wang, and S. Ropele, "Quantitative susceptibility mapping in multiple sclerosis," *Radiology*, vol. 267, no. 2, pp. 551–559, 2013.

[24] F. Schweser, A. Deistung, B. W. Lehr, and J. R. Reichenbach, "Differentiation between diamagnetic and paramagnetic cerebral lesions based on magnetic susceptibility mapping," *Medical Physics*, vol. 37, no. 10, pp. 5165–5178, 2010.

[25] P. J. Basser, S. Pajevic, C. Pierpaoli, J. Duda, and A. Aldroubi, "In vivo fiber tractography using DT-MRI data," *Magn Reson Med*, vol. 44, no. 4, pp. 625–632, 2000.

[26] D. S. Tuch, R. M. Weisskoff, J. W. Belliveau, and V. J. Wedeen, "High angular resolution diffusion imaging of the human brain," *Mag Reson Med*, vol. 7, p. 321, 1999.

[27] K. E. Hammond, J. M. Lupo, D. Xu, S. Veeraraghavan, H. Lee, A. Kincaid, D. B. Vigneron, G. T. Manley, S. J. Nelson, and P. Mukherjee, "Microbleed detection in traumatic brain injury at 3t and 7t: Comparing 2d and 3d gradient-recalled echo (gre) imaging with susceptibility-weighted imaging (swi)," *ISMRM*, vol. 248, 2009.

[28] B. Bilgic, A. P. Fan, J. R. Polimeni, S. F. Cauley, M. Bianciardi, E. Adalsteinsson, L. L. Wald, and K. Setsompop, "Fast quantitative susceptibility mapping with l1-regularization and automatic parameter selection," *Magnetic Resonance in Medicine*, vol. 72, no. 5, pp. 1444–1459, 2014. [Online]. Available: http://dx.doi.org/10.1002/mrm.25029

[29] S. Cetin and G. Unal, "A higher-order tensor vessel tractography for segmentation of vascular structures," *Medical Imaging, IEEE Transactions on*, vol. 34, no. 10, pp. 2172–2185, Oct 2015.

[30] T. Koller, G. Gerig, G. Szekely, and D. Dettwiler, "Multiscale detection of curvilinear structures in 2-d and 3-d image data," in *Computer Vision. Proceedings., Fifth International Conference on*, 1995, pp. 864 –869.

[31] C. Lorenz, I.-C. Carlsen, T. M. Buzug, C. Fassnacht, and J. Weese, "Multi-scale line segmentation with automatic estimation of width, contrast and tangential direction in 2d and 3d medical images," in *Proceedings of the First Joint Conference on Computer Vision, Virtual Reality and Robotics in Medicine and Medial Robotics and Computer-Assisted Surgery*. London, UK, UK: Springer-Verlag, 1997, pp. 233–242.

[32] Y. Sato, S. Nakajima, H. Atsumi, T. Koller, G. Gerig, S. Yoshida, and R. Kikinis, "3D Multi-scale line filter for segmentation and visualization of curvilinear structures in medical images," in *CVRMed-MRCAS '97: Proceedings of the First Joint Conference on Computer Vision, Virtual Reality and Robotics in Medicine and Medial Robotics and Computer-Assisted Surgery*. London, UK: Springer-Verlag, 1997, pp. 213–222.

[33] A. F. Frangi, W. J. Niessen, K. L. Vincken, and M. A. Viergever, "Multiscale Vessel Enhancement Filtering," *Medical Image Computing and Computer-Assisted Interventation MICCAI'98*, pp. 130–137, 1998.

[34] P. Orłowski and M. Orkisz, "Efficient computation of Hessian-based enhancement filters for tubular structures in 3D images," *IRBM*, vol. 30, no. 3, pp. 128–132, 2009.

[35] K. Krissian, "Flux-based anisotropic diffusion applied to enhancement of 3-d angiogram," *IEEE TMI*, vol. 21, no. 11, pp. 1440–1442, 2002.

[36] R. Manniesing, M. Viergever, and W. Niessen, "Vessel enhancing diffusionA scale space representation of vessel structures," *Medical Image Analysis*, vol. 10, no. 6, pp. 815–825, 2006.

[37] L. Risser, F. Plouraboue, and X. Descombes, "Gap Filling of 3-D Microvascular Networks by Tensor Voting," *Medical Imaging, IEEE Transactions on*, vol. 27, no. 5, pp. 674–687, 2008.

[38] M. W. Law and A. C. Chung, "Three dimensional curvilinear structure detection using optimally oriented flux," in *Proceedings of the 10th European Conference on Computer Vision: Part IV*. Berlin, Heidelberg: Springer-Verlag, 2008, pp. 368–382.

[39] D. Lesage, E. D. Angelini, I. Bloch, and G. Funka-Lea, "Bayesian maximal paths for coronary artery segmentation from 3d ct angiograms," in *Proceedings of the 12th International Conference on Medical Image Computing and Computer-Assisted Intervention: Part I*, ser. MICCAI '09, 2009, pp. 222–229.

[40] C. Kirbas and F. Quek, "A review of vessel extraction techniques and algorithms," *ACM Comput. Surv.*, vol. 36, pp. 81–121, 2004.

[41] P. Felkel, R. Wegenkittl, and A. Kanitsar, "Vessel Tracking in Peripheral CTA Datasets - An Overview," in *IEEE Spring Conference on Computer Graphics (SCCG)*, 2001, pp. 232–239.

[42] J. S. Suri, K. C. Liu, L. Reden, and S. Laxminarayan, "A review on MR vascular image processing algorithms: Acquisition and prefiltering: part I," *IEEE T. Inf. Technol. Biomed.*, vol. 6, no. 4, pp. 324–337, 2002.

[43] J. S. Suri, K. Liu, L. Reden, and S. Laxminarayan, "A review on mr vascular image processing: skeleton versus nonskeleton approaches: part ii," *IEEE Transactions on Information Technology in Biomedicine*, vol. 6, no. 4, pp. 338–350, 2002.

[44] K. Bühler, P. Felkel, and A. L. Cruz, "Geometric methods for vessel visualization and quantification – a survey," in *In Geometric Modelling For Scientific Visualization*, 2002, pp. 399–420.

[45] D. Lesage, E. D. Angelini, I. Bloch, and G. Funka-Lea, "A review of 3D vessel lumen segmentation techniques," *Med. Imag. Anal.*, vol. 13, no. 6, pp. 819–845, 2009.

[46] L. M. Lorigo, O. D. Faugeras, W. E. Grimson, R. Keriven, R. Kikinis, A. Nabavi, and C. F. Westin, "CURVES: curve evolution for vessel segmentation." *Med Image Anal*, vol. 5, no. 3, pp. 195–206, 2001.

[47] R. Manniesing, M. Viergever, and W. Niessen, "Vessel axis tracking using topology constrained surface evolution," *Medical Imaging, IEEE Transactions on*, vol. 26, no. 3, pp. 309 –316, march 2007.

[48] X. Zhu, Z. Xue, X. Gao, Y. Zhu, and S. Wong, "Voles: Vascularity-oriented level set algorithm for pulmonary vessel segmentation in image guided intervention therapy," in *Biomedical Imaging: From Nano to Macro, 2009. ISBI '09. IEEE International Symposium on*, 28 2009-july 1 2009, pp. 1247 –1250.

[49] S. Worz and K. Rohr, "Segmentation and quantification of human vessels using a 3-d cylindrical intensity model," *Image Processing, IEEE Transactions on*, vol. 16, no. 8, pp. 1994 –2004, aug. 2007.

[50] O. Friman, M. Hindennach, C. Kühnel, and H.-O. Peitgen, "Multiple hypothesis template tracking of small 3D vessel structures," *Med. Imag. Anal.*, vol. 14, no. 2, pp. 160–171, 2010.

[51] Y. Zheng, H. Tek, and G. Funka-Lea, "Robust and accurate coronary artery centerline extraction in cta by combining model-driven and data-driven approaches," in *MICCAI*, 2013, pp. 74–81.

[52] T. Deschamps and L. D. Cohen, "Fast extraction of minimal paths in 3d images and applications to virtual endoscopy," *Med. Imag. Anal.*, vol. 5, no. 4, pp. 281 – 299, 2001.

[53] L. Cohen and R. Kimmel, "Global minimum for active contour models: A minimal path approach," *International Journal of Computer Vision*, vol. 24, pp. 57–78, 1997.

[54] H. Li and A. J. Yezzi, "Vessels as 4-d curves: Global minimal 4-d paths to extract 3-d tubular surfaces and centerlines," *IEEE Trans. Med. Imaging*, vol. 26, no. 9, pp. 1213–1223, 2007.

[55] F. Benmansour, L. D. Cohen, M. W. K. Law, and A. Chung, "Tubular anisotropy for 2d vessel segmentation." in *CVPR*. IEEE, 2009, pp. 2286–2293.

[56] D. Baboiu and G. Hamarneh, "Vascular bifurcation detection in scale-space," in *IEEE workshop on Mathematical Methods for Biomedical Image Analysis (IEEE MMBIA)*, 2012, pp. 41–46.

[57] L. Antiga and D. Steinman, "Robust and objective decomposition and mapping of bifurcating vessels," *Medical Imaging, IEEE Transactions on*, vol. 23, no. 6, pp. 704 –713, june 2004.

[58] M. Piccinelli, A. Veneziani, D. A. Steinman, A. Remuzzi, and L. Antiga, "A framework for geometric analysis of vascular structures: Application to cerebral aneurysms." *IEEE Trans. Med. Imaging*, vol. 28, no. 8, pp. 1141–1155, 2009.

[59] F. Yuan, Y. Chi, S. Huang, and J. Liu, "Modeling n-furcated liver vessels from a 3-d segmented volume using hole-making and subdivision methods." *IEEE Trans. Biomed. Engineering*, vol. 59, no. 2, pp. 552–561, 2012.

[60] G. Xiong, S. Musuvathy, and T. Fang, "Automated structured all-quadrilateral and hexahedral meshing of tubular surfaces," in *IMR*, 2012, pp. 103–120.

[61] D. Pace, A. Enquobahrie, P. Reynolds, J. Jomier, E. Bullitt, and S. Aylward, "Tubetk: An open-source toolkit of algorithms operating on images of tubes," *International Congress and Exhibition on CARS.*, vol. 7, no. S1, pp. S79–S80, 2012.

[62] D. S. Tuch, R. Weisskoff, J. Belliveau, and V. Wedeen, "High angular resolution diffusion imaging of the human brain," in *Proceedings of the 7th Annual Meeting of ISMRM, Philadelphia*, vol. 321, 1999.

[63] E. Ozarslan and T. H. Mareci, "Generalized diffusion tensor imaging and analytical relationships between diffusion tensor imaging and high angular resolution diffusion imaging," *Magn. Reson. Med*, vol. 50, pp. 955–965, 2003.

[64] B. C. V. A. Barmpoutis, B. Jian and T. M. Shepherd, "Symmetric positive 4th order tensors and their estimation from diffusion weighted mri," *IPMI*, pp. 308–319, 2007.

[65] D. S. Tuch, "Q-ball imaging," *Magnetic Resonance in Medicine*, vol. 52, no. 6, pp. 1358–1372, Dec. 2004.

[66] D. H. A. Barmpoutis, B. C. Vemuri and J. R. Forder, "Extracting tractosemas from a displacement probability field for tractography in dw-mri," *In LNCS 5241, (Springer) Proceedings of MICCAI08: Int. Conf. on Medical Image Computing and Computer Assisted Intervention*, pp. 9–16, 6-10 September 2008.

[67] A. Tristan-Vega, C.-F. Westin, and S. Aja-Fernandez, "Estimation of fiber orientation probability density functions in high angular resolution diffusion imaging." *NeuroImage*, vol. 47, no. 2, pp. 638–650, 2009.

[68] C. P. Hess, P. Mukherjee, E. T. Han, D. Xu, and D. B. Vigneron, "Q-ball reconstruction of multimodal fiber orientations using the spherical harmonic basis," *Magnetic Resonance in Medicine*, vol. 56, no. 1, pp. 104–117, 2006.

[69] P. J. Basser, S. Pajevic, C. Pierpaoli, J. Duda, and A. Aldroubi, "In vivo fiber tractography using DT-MRI data," *Magnetic resonance in medicine*, vol. 44, no. 4, pp. 625–632, 2000.

[70] T. Schultz, "Towards resolving fiber crossings with higher order tensor inpainting," in *New Developments in the Visualization and Processing of Tensor Fields*, D. H. Laidlaw and A. Vilanova, Eds., 2012, pp. 253–265.

[71] T. Schultz, J. Weickert, and H.-P. Seidel, "A higher-order structure tensor," in *Visualization and Processing of Tensor Fields – Advances and Perspectives*, D. H. Laidlaw and J. Weickert, Eds., 2009, pp. 263–280.

[72] K. Krissian, G. Malandain, N. Ayache, R. Vaillant, and Y. Trousset, "Model-based detection of tubular structures in 3d images," *Computer Vision and Image Understanding*, vol. 80, no. 2, pp. 130 – 171, 2000.

[73] J. H. A. Barmpoutis and B. C. Vemuri, "Approximating symmetric positive semidefinite tensors of even order," *SIAM Journal on Imaging Sciences*, vol. 5, no. 1, pp. 434–464, 2012.

[74] A. Ghosh, M. Descoteaux, and R. Deriche, "Riemannian Framework for estimating Symmetric Positive Definite 4th Order Diffusion Tensors," in *MICCAI*, vol. 5241, 2008, pp. 858–865.

[75] M. Descoteaux, E. Angelino, S. Fitzgibbons, and R. Deriche, "Apparent Diffusion Coefficients from High Angular Resolution Diffusion Images: Estimation and Applications," *Magnetic Resonance in Medicine*, vol. 56, pp. 395–410, 2006.

[76] L. Qi, "Eigenvalues of a real supersymmetric tensor." *J. Symb. Comput.*, vol. 40, no. 6, pp. 1302–1324, 2005.

[77] T. G. Kolda and B. W. Bader, "Tensor decompositions and applications," *SIAM REVIEW*, vol. 51, no. 3, pp. 455–500, 2009.

[78] G. Bergqvist and E. G. Larsson, "The higher-order singular value decomposition theory and an application," *IEEE signal processing magazine (Print)*, vol. 27, no. 3, pp. 151–154, 2010.

[79] L. D. Lathauwer, B. D. Moor, and J. Vandewalle, "On the best rank-1 and rank-(r1,r2,. . .,rn) approximation of higher-order tensors," *SIAM J. Matrix Anal. Appl.*, vol. 21, no. 4, pp. 1324–1342, Mar. 2000.

[80] M. Descoteaux, R. Deriche, T. R. Knosche, and A. Anwander, "Deterministic and probabilistic tractography based on complex fibre orientation distributions." *Medical Imaging, IEEE Transactions on*, vol. 28, no. 2, pp. 269–286, 2009.

[81] G. Hamarneh and P. Jassi, "Vascusynth: Simulating vascular trees for generating volumetric image data with ground-truth segmentation and tree analysis," *Computerized Medical Imaging and Graphics*, vol. 34, no. 8, pp. 605 – 616, 2010.

[82] M. Schaap, C. T. Metz, T. van Walsum, A. G. van der Giessen, A. C. Weustink, N. R. Mollet, C. Bauer, H. Bogunovic, C. Castro, X. Deng, E. Dikici, T. O'Donnell, M. Frenay, O. Friman, M. H. Hoyos, P. H. Kitslaar, K. Krissian, C. Kuhnel, M. A. Luengo-Oroz, and M. Orkisz, "Standardized evaluation methodology and reference database for evaluating coronary artery centerline extraction algorithms," *Medical Image Analysis*, vol. 13, pp. 701–714, 2009.

[83] H. Kirisli, M. Schaap, S. Klein, S. Papadopoulou, M. Bonardi, C. Chen, A. Weustink, N. Mollet, E. P. A. Vonken, R. van der Geest, T. v. Walsum, and W. Niessen, "Evaluation of a multi-atlas based method for segmentation of cardiac cta data: a large-scale, multi-center and multi-vendor study," *Medical Physics*, vol. 37, no. 12, pp. 6279–6291, 2010.

[84] E. Bullitt, D. Zeng, G. Gerig, S. Aylward, S. Joshi, J. Smith, W. Lin, and M. Ewend, "Vessel tortuosity and brain tumor malignancy: A blinded study," *Acad Radiol*, vol. 12, no. 10, pp. 1232–1240, 2005.

[85] S. Aylward and E. Bullitt, "Initialization, noise, singularities, and scale in height ridge traversal for tubular object centerline extraction," *Medical Imaging, IEEE Transactions on*, vol. 21, no. 2, pp. 61 –75, feb. 2002.

[86] D. Steinman and L. A Antiga, "Vmtk: the vascular modeling toolkit," Available at http://www.vmtk.org.

[87] R. Cárdenes, J. L. Díez, I. Larrabide, H. Bogunovic, and A. F. Frangi, "3d modeling of coronary artery bifurcations from cta and conventional coronary angiography," in *MICCAI*, 2011, pp. 395–402.

[88] H. Bogunović, J. M. Pozo, M. C. Villa-Uriol, C. B. L. M. Majoie, R. van den Berg, H. A. F. Gratama van Andel, J. M. Macho, J. Blasco, L. San Román, and A. F.

Frangi, "Automated segmentation of cerebral vasculature with aneurysms in 3dra and tof-mra using geodesic active regions: An evaluation study," *Medical Physics*, vol. 38, no. 1, pp. 210–222, 2011.

[89] C. M. Hentschke, O. Beuing, R. Nickl, and K. D. T önnies, "Automatic cerebral aneurysm detection in multimodal angiographic images," in *Nuclear Science Symposium and Medical Imaging Conference (NSS/MIC)*, 2011, pp. 3116 – 3120.

[90] T. Jerman, Z. Spiclin, B. Likar, and F. Pernus, "Blob enhancement filter for computer aided diagnosis of cerebral aneurysms," in *Miccai Workshops of Computing and Visualization for Intravascular Imaging and Computer Assisted Stenting*, Boston, 2014.

[91] J. D. Tournier, F. Calamante, D. G. Gadian, and A. Connelly, "Direct estimation of the fiber orientation density function from diffusion-weighted MRI data using spherical deconvolution," *NeuroImage*, vol. 23, pp. 1176–1185, 2004.

[92] E. J. Canales-Rodriguez, L. Melie-Garcia, Y. Iturria-Medina, and Y. Aleman-Gomez, "High angular resolution diffusion imaging (HARDI) tools," Available at http://neuroimagen.es/webs/hardi_tools/.

[93] V. J. Wedeen, P. Hagmann, W.-Y. I. Tseng, T. G. Reese, and R. M. Weisskoff, "Mapping complex tissue architecture with diffusion spectrum magnetic resonance imaging," *Magnetic Resonance in Medicine*, vol. 54, no. 6, pp. 1377–1386, 2005. [Online]. Available: http://dx.doi.org/10.1002/mrm.20642

[94] E. Özarslan and T. H. Mareci, "Generalized diffusion tensor imaging and analytical relationships between diffusion tensor imaging and high angular resolution diffusion imaging," *Magn Reson Med*, vol. 50, no. 5, pp. 955–965, 2003.

[95] C. Liu, R. Bammer, B. Acar, and M. E. Moseley, "Characterizing non-Gaussian diffusion by using generalized diffusion tensors," *Magn Reson Med*, vol. 51, no. 5, pp. 924–37, 2004.

[96] E. Özarslan, C. G. Koay, T. M. Shepherd, M. E. Komlosh, M. O. İrfanoğlu, C. Pierpaoli, and P. J. Basser, "Mean apparent propagator (MAP) MRI: a novel diffusion imaging method for mapping tissue microstructure," *NeuroImage*, vol. 78, pp. 16–32, 2013.

[97] A. Ozcan, "Complete Fourier direct magnetic resonance imaging (CFD-MRI) for diffusion MRI," *Front Integr Neurosci*, vol. 7, p. 18, 2013.

[98] A. W. Anderson and J. C. Gore, "Analysis and correction of motion artifacts in diffusion weighted imaging," *Magnetic Resonance in Medicine*, vol. 32, no. 3, pp. 379–387, 1994.

[99] B. Jeurissen, A. Leemans, J.-D. Tournier, D. K. Jones, and J. Sijbers, "Investigating the prevalence of complex fiber configurations in white matter tissue with diffusion magnetic resonance imaging," *Human Brain Mapping*, vol. 34, no. 11, pp. 2747–2766, 2013.

[100] J.S.W.Campbell, P. Savadjiev, K. Siddiqi, and G. Pike, "Validation and Regularization in Diffusion MRI Tractography," in *ISBI*, 2006, pp. 351–354.

[101] M. Pizzolato, D. Wassermann, T. Boutelier, and R. Deriche, "Exploiting the Phase in Diffusion MRI for Microstructure Recovery: Towards Axonal Tortuosity via Asymmetric Diffusion Processes," in *Medical Image Computing and Computer Assisted Intervention*, Munich, Germany, 2015. [Online]. Available: https://hal.inria.fr/hal-01152672

[102] H.-H. Ehricke, K.-M. Otto, and U. Klose, "Regularization of bending and crossing white matter fibers in MRI q-ball fields," *Magn Reson Imaging*, vol. 29, pp. 916–926, 2011.

[103] M. Descoteaux, E. Angelino, S. Fitzgibbons, and R. Deriche, "Regularized, fast, and robust analytical q-ball imaging," *Magnetic Resonance in Medicine*, vol. 58, no. 3, pp. 497–510, 2007.

[104] C. Tomasi, "Bilateral filtering for gray and color images," 1998, pp. 839–846.

[105] H. Knutsson, R. Wilson, and G. Granlund, "Anisotropic nonstationary image estimation and its applications: Part i–restoration of noisy images," *IEEE Transactions on Communications*, vol. 31, no. 3, pp. 388–397, Mar 1983.

[106] W. T. Freeman and E. H. Adelson, "The design and use of steerable filters," *IEEE Transactions on Pattern Analysis and Machine Intelligence*, vol. 13, pp. 891–906, 1991.

[107] P. Perona, *Computer Vision — ECCV'92: Second European Conference on Computer Vision Santa Margherita Ligure, Italy, May 19–22, 1992 Proceedings*. Berlin, Heidelberg: Springer Berlin Heidelberg, 1992, ch. Steerable-scalable kernels for edge detection and junction analysis, pp. 3–18. [Online]. Available: http://dx.doi.org/10.1007/3-540-55426-2_1

[108] E. P. Simoncelli and H. Farid, "Steerable wedge filters for local orientation analysis," *IEEE Transactions on Image Processing*, vol. 5, no. 9, pp. 1377–1382, Sep 1996.

[109] E. P. Simoncelli, "The steerable pyramid." [Online]. Available: http://www.cns.nyu.edu/~eero/steerpyr/

[110] F. Aguet, M. Jacob, and M. Unser, "Three-dimensional feature detection using optimal steerable filters," in *IEEE International Conference on Image Processing 2005*, vol. 2, Sept 2005, pp. II–1158–61.

[111] M. Descoteaux, R. Deriche, T. R. Knösche, and A. Anwander, "Deterministic and probabilistic tractography based on complex fibre orientation distributions." *IEEE Trans. Med. Imaging*, vol. 28, no. 2, pp. 269–286, 2009.

[112] S. Cetin, B. B. Bilgic, A. Fan, K. Setsompop, and G. Unal, "Semi-automated visualization and segmentation of cerebral veins from qsm," *ISMRM*, vol. 2193, 2015.

[113] B. Serres, A. Deistung, A. Schäfer, M. Kocinski, A. Materka, and J. Reichenbach, "Automatic segmentation of the venous vessel network based on quantitative susceptibility maps and its application to investigate blood oxygenation," *ISMRM*, vol. 169, 2015.

[114] T. Christen, D. S. Bolar, and G. Zaharchuk, "Imaging Brain Oxygenation with MRI Using Blood Oxygenation Approaches: Methods, Validation, and Clinical Applications," *American Journal of Neuroradiology*, Aug. 2012.

[115] L. de Rochefort, T. Liu, B. Kressler, J. Liu, P. Spincemaille, V. Lebon, J. Wu, and Y. Wang, "Quantitative susceptibility map reconstruction from mr phase data using bayesian regularization: Validation and application to brain imaging," *Magnetic Resonance in Medicine*, vol. 63, no. 1, pp. 194–206, 2010.

[116] A. P. Fan, B. Bilgic, L. Gagnon, T. Witzel, H. Bhat, B. R. Rosen, and E. Adalsteinsson, "Quantitative oxygenation venography from mri phase," *Magnetic Resonance in Medicine*, vol. 72, no. 1, pp. 149–159, 2014. [Online]. Available: http://dx.doi.org/10.1002/mrm.24918

[117] R. M. Weisskoff and S. Kiihne, "Mri susceptometry: Image-based measurement of absolute susceptibility of mr contrast agents and human blood," *Magnetic Resonance in Medicine*, vol. 24, no. 2, pp. 375–383, 1992. [Online]. Available: http://dx.doi.org/10.1002/mrm.1910240219

[118] M. Lustig, D. Donoho, and J. M. Pauly, "Sparse MRI: The application of compressed sensing for rapid MR imaging," *MRM*, vol. 58, no. 6, pp. 1182–1195, 2007.

[119] T. Liu, P. Spincemaille, L. de Rochefort, B. Kressler, and Y. Wang, "Calculation of susceptibility through multiple orientation sampling (cosmos): A method for conditioning the inverse problem from measured magnetic field map to susceptibility source image in mri," *Magnetic Resonance in Medicine*, vol. 61, no. 1, pp. 196–204, 2009.

[120] B. Bilgic, L. Xie, R. Dibb, C. Langkammer, A. Mutluay, H. Ye, J. R. Polimeni, J. Augustinack, C. Liu, L. L. Wald, and K. Setsompop, "Rapid multi-orientation quantitative susceptibility mapping," *NeuroImage*, vol. 125, pp. 1131 – 1141, 2016.

[121] W. Li, B. Wu, and C. Liu, "Quantitative susceptibility mapping of human brain reflects spatial variation in tissue composition," *NeuroImage*, vol. 55, no. 4, pp.

1645 – 1656, 2011. [Online]. Available: http://www.sciencedirect.com/science/article/pii/S1053811911000164

[122] F. Schweser, A. Deistung, B. W. Lehr, and J. R. Reichenbach, "Quantitative imaging of intrinsic magnetic tissue properties using {MRI} signal phase: An approach to in vivo brain iron metabolism?" *NeuroImage*, vol. 54, no. 4, pp. 2789 – 2807, 2011.

[123] S. M. Smith, "Fast robust automated brain extraction," *Human Brain Mapping*, vol. 17, no. 3, pp. 143–155, 2002. [Online]. Available: http://dx.doi.org/10.1002/hbm.10062

[124] N. Toussaint, J. christophe Souplet, and P. Fillard, "Medinria: medical image navigation and research tool by inria," in *In: Proceedings of MICCAI Workshop on Interaction in Medical Image Analysis and Visualization*, 2007.

[125] J. P. Bremmer, B. N. M. Berckel, S. Persoon, L. J. Kappelle, A. A. Lammertsma, R. Kloet, G. Luurtsema, A. Rijbroek, C. J. M. Klijn, and R. Boellaard, "Day-to-day test–retest variability of cbf, cmro2, and oef measurements using dynamic 15o pet studies," *Molecular Imaging and Biology*, vol. 13, no. 4, pp. 759–768, 2010. [Online]. Available: http://dx.doi.org/10.1007/s11307-010-0382-1